

Unified Control for the Permanent Magnet Generator and Rectifier System

Zhuxian Xu

Thesis submitted to the faculty of the Virginia Polytechnic Institute and
State University in partial fulfillment of the requirements for the degree
of

Master of Science
In
Electrical Engineering

Committee:
Fred Wang (Co-Chair)
Jaime de la Ree (Co-Chair)
Dushan Boroyevich

May 3, 2010
Blacksburg, Virginia

Keywords: PMG and rectifier system, Unified control, System efficiency
optimization, Sensorless vector control

Unified Control for the Permanent Magnet Generator and Rectifier System

Zhuxian Xu

Abstract

The structure of a permanent magnet generator (PMG) connected with an active front-end rectifier is very popular in the AC-DC architecture. Especially for certain applications like aircraft and vehicles, power density and efficiency is critical. Since the generator and the rectifier can be controlled simultaneously, it would be very desirable to develop a unified control. With this unified control, the boost inductors between the PMG and rectifier is eliminated, which significantly reduce the volume and the weight of the whole system and improve the system power density. Also the system efficiency can be improved with appropriate control strategy.

In this thesis, a unified control for the permanent magnet generator and rectifier system is presented. Firstly, the unified model of the PMG and rectifier system is given as the basis to design the control system. Secondly, a unified control method for PMG and rectifier system is introduced. The design procedure for each control loops are presented in detail, including current control loop, voltage control loop, reactive control loop and speed and rotor position estimator loop. Thirdly, the hardware is developed and the experiment is conducted to verify the control strategy. Fourthly, a method to optimize the overall system efficiency by appropriate reactive power distribution is proposed. The two cases when the DC link voltage is flexible and the DC link voltage is fixed are considered.

Acknowledgements

I would like to express my sincere gratitude to my advisor, Dr. Fred Wang, for his support, guidance and encouragement during my study as well as my daily life. He led me to the area of power electronics with his incisive view and profound knowledge, encouraged me to dig into the area and helped me kindly when I met problems. His gentle personality and rigorous attitude toward research will benefit my career as well as my whole personal life.

I am also deeply grateful to my committee member, Dr. Dushan Boroyevich, for his numerous smart ideas and valuable instructions. He is always generous to give me suggestions, encouragement and ideas to help me in the research project. I would also like to thank my co-advisor Dr. Jaime de la Ree for helping me a lot along the graduate student period.

I am very grateful to all my colleagues in CPES for their help, mentorship, and friendship. I may not be able to list all the names but here are some I have to mention: Dr. Ming Xu, Dr. Shuo Wang, Dr. Yue Chang, Dr. Yuling Li, Dr. Jerry Francis, Dr. Rixin Lai, Dr. Dianbo Fu, Dr. Jing Xu, Dr. Pengju Kong, Igor Cvetkovic, Qiang Li, Puqi Ning, Ruxi Wang, Zhiyu Shen, Dong Dong, Zheng Chen, Qian Li, Xiao Cao, Tong Liu, Daocheng Huang, Ying Lu, Zheng Zhao, Jing Xue, Feng Yu, Haoran Wu, Bo Wen, Mingkai Mu, Zheyuan Tan, Wei Zhang, Shuilin Tian, Xuning Zhang and so many others. In particular, I would like to thank Dr. Di Zhang, Dong Jiang, Sara Ahmed and Yingyi Yan for their help and time on my research.

Thank you all the CPES staff, Marianne Hawthorne, Teresa Shaw, Trish Rose, Linda Gallagher, and Robert Martin, Dan Huff, Elizabeth Tranter, for making this lab a wonderful place for research.

At last but also the most important, I will thank my dear parents for their love, support and confidence in me.

Table of Contents

Chapter 1	Introduction.....	1
1.1	Background and Motivation.....	1
1.2	Literature Survey and Research Challenges.....	3
1.3	Thesis Organization.....	5
Chapter 2	Model of Permanent Magnet Generator and Rectifier System.....	7
2.1	Topology and Parameters.....	7
2.1.1	Permanent Magnet Generator	8
2.1.2	Passive Components Selection of the Boost Rectifier.....	9
2.2	Permanent Magnet Generator Model	11
2.3	Two-level Active Rectifier Model	13
2.4	PMG and Rectifier System Model	15
Chapter 3	Control Design for PMG and Rectifier System.....	18
3.1	Structure of Proposed Unified Control System.....	18
3.2	Inner Current Loop Design	19
3.2.1	D-Q Decoupling.....	19
3.2.2	Compensator Design.....	21
3.2.3	Small-signal Analysis in Saber	23
3.3	Outer Voltage Loop Design	26
3.3.1	Compensator Design.....	26

3.3.2	Small Signal Analysis in Saber.....	27
3.4	Instantaneous Reactive Power Loop Control.....	29
3.5	Sensorless Vector Control.....	29
3.5.1	Speed Estimation Strategy	31
3.5.2	Back EMF Observer Design	32
3.5.3	Tracking Controller Design	37
3.5.4	Simulation Verification.....	40
3.6	Control System Specifications	41
3.7	Simulation Verification in Saber for PMG and Rectifier System.....	42
Chapter 4	Hardware Development and Experiments	47
4.1	System Configuration.....	47
4.2	Hardware Design.....	50
4.2.1	Signal Conditioning Board	50
4.2.2	IPM and the Driver Board.....	53
4.2.3	PMG Parameters Measurement	58
4.3	Experimental Verification.....	60
4.3.1	PMG and diode rectifier system experiment	60
4.3.2	PMG and active front-end rectifier system experiment.....	61
Chapter 5	System Efficiency Optimization.....	69
5.1	Reactive Power Distribution	69

5.2	Loss Calculation	71
5.3	System efficiency optimization with flexible DC link voltage	73
5.4	System efficiency optimization with fixed DC link voltage	77
Chapter 6	Conclusions and Future Work	82
6.1	Conclusions	82
6.2	Future Work	83
Reference	84

Table of Figures

Figure 1-1 PM machines have no rotor copper loss [7].....	2
Figure 1-2 Advantage of PM motors vs. induction motors [7].....	2
Figure 1-3 PMG with a diode rectifier [2].....	3
Figure 1-4 PMG with a diode rectifier followed by a dc chopper	3
Figure 2-1 Power stage configuration of the PMG and rectifier system	7
Figure 2-2 Magnetic saliency of IPM machine [7].....	8
Figure 2-3 Minimum inductance L_{\min} required at different switching frequency for three different THD specifications [26].....	10
Figure 2-4 Equivalent circuits of the permanent magnet synchronous generator in d-q axes	12
Figure 2-5 Switching model of the boost rectifier	13
Figure 2-6 Equivalent circuit of VSR average model in a-b-c coordinates.....	14
Figure 2-7 Equivalent circuit of VSR average model in d-q coordinates.....	15
Figure 2-8 Model of PMG and rectifier system.....	16
Figure 3-1 Control Schematic of PMG and rectifier system	19
Figure 3-2 Multi-Input-Multi-Output vs. Single-Input-Single-Output structures	20
Figure 3-3 Decoupled D and Q channels.....	21
Figure 3-4 Control schematic with D-Q decoupling.....	21
Figure 3-5 Circuit for measuring D channel current loop gain.....	24
Figure 3-6 Bode magnitude and phase diagrams of D channel current loop gain	24
Figure 3-7 Circuit for measuring Q channel current loop gain.....	25
Figure 3-8 Bode magnitude and phase diagrams of Q channel current loop gain.....	26
Figure 3-9 Schematic of voltage controller	26

Figure 3-10 Circuit for measuring Q outer voltage loop gain	28
Figure 3-11 Bode magnitude and phase diagrams of outer voltage loop gain.....	28
Figure 3-12 Location of d-q axes in the front-end rectifier with a PLL	30
Figure 3-13 Location of d-q axes in the PMG and rectifier system with a back EMF observer and a PLL-based tracking controller.....	30
Figure 3-14 Relationship between actual and estimated synchronous reference frames.....	31
Figure 3-15 Asymptotic state observer block diagram.....	32
Figure 3-16 Asymptotic state observer block diagram for PMG and rectifier system	35
Figure 3-17 Simulation scheme for back EMF test	37
Figure 3-18 Back EMF components in d-q axes calculated by the observer.....	37
Figure 3-19 PLL-based tracking controller block diagram.....	38
Figure 3-20 Simulation scheme for PLL-base tracking controller test.....	39
Figure 3-21 Comparison between the estimated angle and the actual angle	39
Figure 3-22 Simulation scheme for observer and tracking controller testing.....	40
Figure 3-23 Estimated rotor position and back EMF.....	41
Figure 3-24 Simulation waveforms of angle, PMG terminal voltage v_{ab} , ac current i_a and dc bus voltage V_{dc} at full speed with unity power factor control in the PMG and active front-end rectifier system.....	43
Figure 3-25 Simulation waveforms of angle, PMG terminal voltage v_a , ac current i_a and dc bus voltage V_{dc} when the current leads the voltage.....	44
Figure 3-26 Simulation waveforms of angle, PMG terminal voltage v_{ab} , ac current i_a and dc bus voltage V_{dc} when the current lags the voltage	44

Figure 3-27 Simulation waveforms of angle, PMG terminal voltage v_{ab} , dc bus voltage V_{dc} and ac current i_a at 2/3 of the full speed in the PMG and active front-end rectifier system.....	45
Figure 3-28 Simulation waveforms of angle, PMG terminal voltage v_{ab} , dc bus voltage V_{dc} and ac current i_a at the load step in the PMG and active front-end rectifier system.....	46
Figure 3-29 Simulation waveforms of q axis current i_q and q axis reference current i_{qref} at the load step in the PMG and active front-end rectifier system.....	46
Figure 4-1 Permanent magnet generator.....	48
Figure 4-2 Power stage and control unit.....	48
Figure 4-3 Voltage sensing circuit.....	51
Figure 4-4 2 nd order Butterworth low pass filter.....	52
Figure 4-5 A/D converter circuit.....	53
Figure 4-6 IPM block diagram.....	54
Figure 4-7 Function diagram of HCPL-4504.....	55
Figure 4-8 Circuit diagram of the optocouplers and the pre-driver of IPM.....	55
Figure 4-9 Schematic of the driver board	57
Figure 4-10 Physical structure of the IPM, the driver board and the heat sink	57
Figure 4-11 IPM motor terminal inductance variation according to the rotor position [7]	58
Figure 4-12 Motor terminal d-axis inductance L_d measurement	59
Figure 4-13 Motor terminal q-axis inductance L_q measurement	59
Figure 4-14 Steady state waveforms of angle, PMG terminal voltage v_{ab} , dc bus voltage V_{dc} and ac current i_a in the PMG and diode rectifier system	60
Figure 4-15 Input current spectrum waveforms of the diode rectifier.....	61

Figure 4-16 Steady state waveforms of angle, PMG terminal voltage v_{ab} , dc bus voltage V_{dc} and ac current i_a at full speed in the PMG and active front-end rectifier system	62
Figure 4-17 Input current spectrum waveforms at full speed of the active front-end rectifier.....	63
Figure 4-18 Steady state waveforms of angle, PMG terminal voltage v_{ab} , dc bus voltage V_{dc} and ac current i_a at half speed in the PMG and active front-end rectifier system	64
Figure 4-19 Input current spectrum waveforms at half speed of the active front-end rectifier	65
Figure 4-20 Waveforms of angle, PMG terminal voltage v_{ab} , dc bus voltage V_{dc} and ac current i_a after applying a load change from 200W to 400W in the PMG and active front-end rectifier system	66
Figure 4-21 Waveforms of dc bus voltage V_{dc} , q axis reference current i_{qref} , q axis current i_q , and ac phase current i_a after applying a load change from 200W to 400W in the PMG and active rectifier system.....	67
Figure 5-1 Reactive power distribution in the PMG and rectifier system	70
Figure 5-2 Unity power factor control at back EMF side	70
Figure 5-3 Unity power factor control at generator terminal side	70
Figure 5-4 Parameters measured from the output characteristics.....	72
Figure 5-5 DC bus voltage changes with Q_{rec} with flexible DC bus voltage	73
Figure 5-6 Converter switching loss changes with Q_{rec} with flexible DC bus voltage.....	74
Figure 5-7 Converter conduction loss changes with Q_{rec} with flexible DC bus voltage	74
Figure 5-8 Converter total loss changes with Q_{rec} with flexible DC bus voltage	75
Figure 5-9 PMG copper loss changes with Q_{rec} with flexible DC bus voltage.....	75
Figure 5-10 System overall loss changes with Q_{rec} with flexible DC bus voltage	76
Figure 5-11 System overall efficiency changes with Q_{rec} with flexible DC bus voltage.....	76

Figure 5-12 Modulation index changes with Q_{rec} with fixed DC bus voltage.....	77
Figure 5-13 Converter switching loss changes with Q_{rec} with fixed DC bus voltage.....	78
Figure 5-14 Converter conduction loss changes with Q_{rec} with fixed DC bus voltage	78
Figure 5-15 Converter total loss changes with Q_{rec} with fixed DC bus voltage	79
Figure 5-16 PMG copper loss changes with Q_{rec} with fixed DC bus voltage.....	79
Figure 5-17 System overall loss changes with Q_{rec} with fixed DC bus voltage	80
Figure 5-18 System overall efficiency changes with Q_{rec} with fixed DC bus voltage.....	80

List of Tables

Table 2-1 Parameters of the PMG	9
Table 2-2 Parameters of the active front-end rectifier	11
Table 3-1 Control system specifications.....	42
Table 4-1 Parameters of the PMG and rectifier system.....	49
Table 4-2 Truth table of HCPL-4504.....	55
Table 5-1 Parameters of the demo system for efficiency optimization study.....	71

Chapter 1 Introduction

This chapter first introduces the background of generator and rectifier system. After that, the existing research activities in this area are reviewed, which helps to identify this work and its originality. The challenges to solve the corresponding issues with unified control are then presented. At last the structure of the thesis is given.

1.1 *Background and Motivation*

Nowadays, DC power source has many applications in industry such as AC motor drive, energy storage, renewable energy, chemical electrolysis and so on. However, most power is still produced by generators and transmitted through AC grid lines. Thus AC-DC architecture has become more and more important. In the AC-DC architecture, the structure of a generator connected with a rectifier is very popular. Especially for certain applications like aircraft and vehicles, power density and efficiency is critical. It's desirable to improve the overall efficiency and power density in the generator and rectifier system. [1] - [6]

Permanent magnet synchronous machine has many advantages such as high efficiency, high power density and easy control. [7] Permanent magnet synchronous machine consists of a stator and a PM rotor part. There is no rotor current in PM motors and only stator windings are carrying currents. Therefore copper loss in PM motors can be about half of that in the induction motors, as shown in Figure 1-1. PM motors have some other advantages compared with induction motors, as shown in Figure 1-2. Permanent magnet machines are now widely used to replace synchronous machines because of magnet price reduction, magnetic material characteristic improvement and speed sensorless control theory.

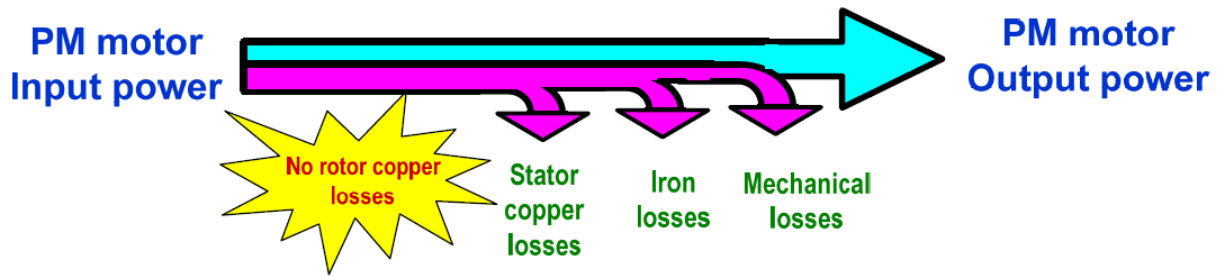


Figure 1-1 PM machines have no rotor copper loss [7]

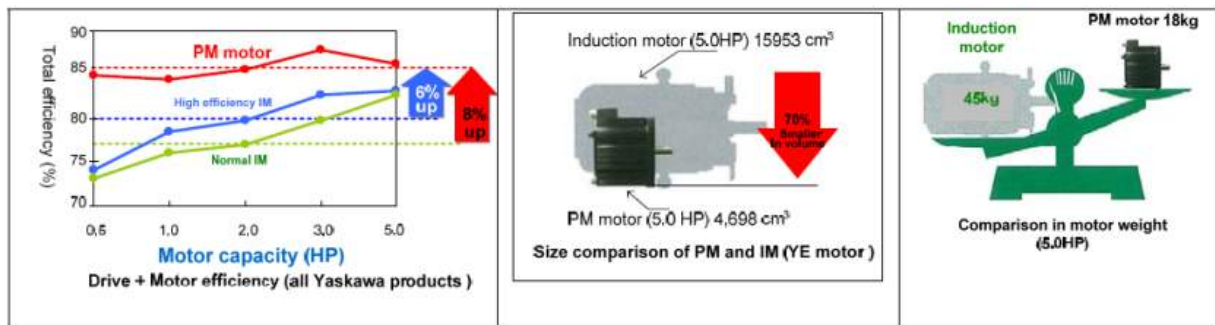


Figure 1-2 Advantage of PM motors vs. induction motors [7]

Due to the growing concerns over power quality, the scope of application of active rectifiers continues to grow in AC-DC system. It is well known that three-phase boost rectifier offers several benefits when compared with a conventional passive diode bridge rectifier. The benefits include sinusoidal input current shaping with low THD, full control of both dc bus voltage and input power factor, bidirectional power flow and so on [8] - [16]. Especially in a system with a generator as AC power source, active rectifier can significantly reduce the power loss in the generator caused by harmonic current.

During the operation of the generator and active rectifier, they can be controlled simultaneously. So it would be very desirable to develop a unified control. With this unified control, the stator inductor can limit the ac current harmonics and provides the opportunity to eliminate the need for additional boost inductor, which will significantly reduce the volume and the weight of the whole system and improve the system power density. Also the system efficiency can be improved with appropriate control strategy.

1.2 Literature Survey and Research Challenges

There are several topologies for AC-DC system. In Figure 1-3 and Figure 1-4, the topologies of a variable-speed permanent-magnet generator with a diode rectifier with and without a following dc chopper are shown respectively. The control method is introduced in [1][2][3] in details. With this configuration, however, the control of the generator power factor is not possible, which in turn, affects generator efficiency. Also, high harmonic distortion currents are obtained in the generator that reduce efficiency and produce torque oscillations.

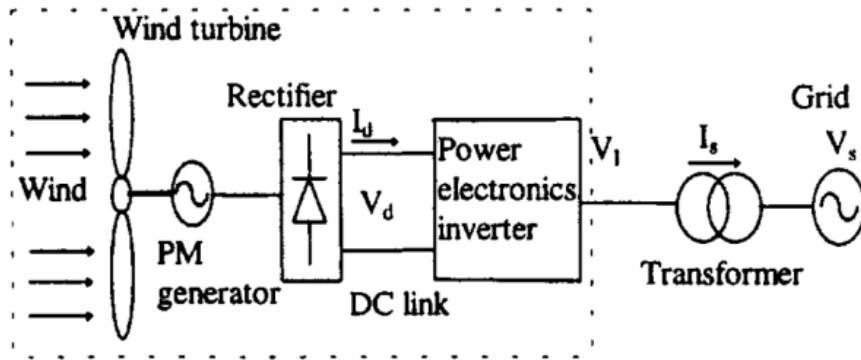


Figure 1-3 PMG with a diode rectifier [2]

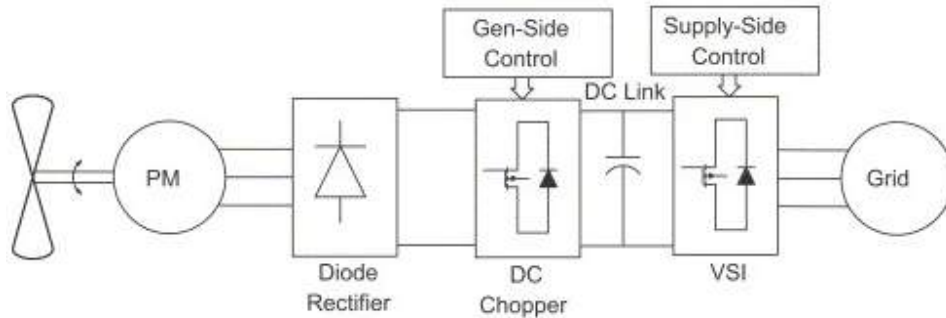


Figure 1-4 PMG with a diode rectifier followed by a dc chopper

Some papers introduce the control method for variable-speed permanent magnet synchronous generators connected with active front-end rectifier. In [4], a vector control scheme of the permanent magnet generator and rectifier is proposed. The proportional plus integral (PI) current and voltage controllers are chosen in order for the required system dynamics and stability. The

direct-axis current i_d is kept to zero to achieve minimum current. However, the power factor isn't controlled in this strategy and the system cannot obtain an optimal efficiency. Also, the sensors are used to obtain the reference angle position and the generator speed, which increase the system cost. In [5] and [6], it is mentioned that the generator reactive current component could be calculated and imposed on the generator in order to minimize power losses, both in the generator and power converter, along the whole operating range. However, no detailed method is provided and direct-axis current component is only set at zero to minimize current and resistive losses in the experimental verification.

In order to do the D-Q coordinates transformation, the electrical angle is necessary. In the conventional front-end rectifier, the input AC voltages are sensed and a phase-locked loop (PLL) is employed to locate the d-q axes by regulating q-axes voltage component v_q to be zero. In PMG and rectifier system, however, the simple PLL doesn't work since the back EMF cannot be sensed directly. In many applications, resolvers or absolute encoders are used as rotor position transducers. However, these position transducers lead to higher cost, larger volume and weight, and moreover lower system reliability. Many sensorless control strategies have been developed for the motor drives over the years [17] - [24]. In [25], a design methodology for a PM motor sensorless vector control scheme using a two-stage approach is presented. It employs a linear asymptotic state observer to estimate the machine back-EMF and a tracking controller to generate the estimated speed and rotor position. However, the sensorless vector control is for speed loop control, which has a comparatively slow dynamics. In the generator and rectifier system, the rotor position is obtained for D-Q axes transformation, which requires a much higher dynamics.

From the survey above, there are many unsolved issues on the unified control for the PMG and rectifier system application.

The main challenges include:

- (1) Method to control PMG and rectifier system without additional boost inductors.
- (2) Method to control both the DC link voltage and reactive power effectively.
- (3) Method to detect the rotor position without sensors.
- (4) Method to optimize the overall system efficiency by appropriate reactive power distribution.

1.3 Thesis Organization

The thesis presents the unified control for the permanent magnet generator and rectifier system. The chapters are organized as follows.

Chapter 2 presents the average model and small signal model of the permanent magnet generator and rectifier system, which is basis to design a unified control system. First the system topology and parameters are described, as well as the reason to select the components value in the system. Based on that, the average models for PMG and rectifier system are created on d-q axes. Finally, the unified model containing PWM and rectifier system are presented, which will be used for the next chapters in this thesis.

Based on the model developed in Chapter 2, Chapter 3 presents the unified control method for PMG and rectifier system. First, the structure of the whole control system is explained. After that, design procedure for each control loops are presented in detail, including current control loop, voltage control loop, reactive control loop and speed and rotor position estimator loop. The performance of the designed control system is analyzed and verified by simulation results.

Chapter 4 presents the hardware development for the permanent magnet generator and rectifier system. First hardware including PMG, IPM and drive board, signal conditioning board are explained in detail. After that, the experimental results with the proposed control schematic are presented and analyzed.

Chapter 5 proposes a method to optimize the overall system efficiency by appropriate reactive power distribution. First a linear loss model is given, which is the basis for loss calculation and efficiency optimization. Then the system loss is compared with different reactive power distribution and finally the optimal point is given. The two cases when the DC link voltage is flexible and the DC link voltage is fixed are discussed respectively.

Finally Chapter 6 summaries the entire thesis and discusses the future work.

Chapter 2 Model of Permanent Magnet Generator and Rectifier System

This chapter presents the average model and small signal model of the permanent magnet generator (PMG) and rectifier system, which is basis to design a unified control system. First the system topology and parameters are described, as well as the reason to select the components value in the system. Based on that, the average models for PMG and rectifier system are created on d-q axes. Finally, the unified model containing PWM and rectifier system are presented, which will be used for the next chapters in this thesis.

2.1 *Topology and Parameters*

The system under study consists of a permanent magnet generator, a two-level three phase active rectifier and a set of resistive load, as shown in Figure 2-1. There are no additional passive components involved between the PMG and the rectifier to limit the harmonic currents on ac side.

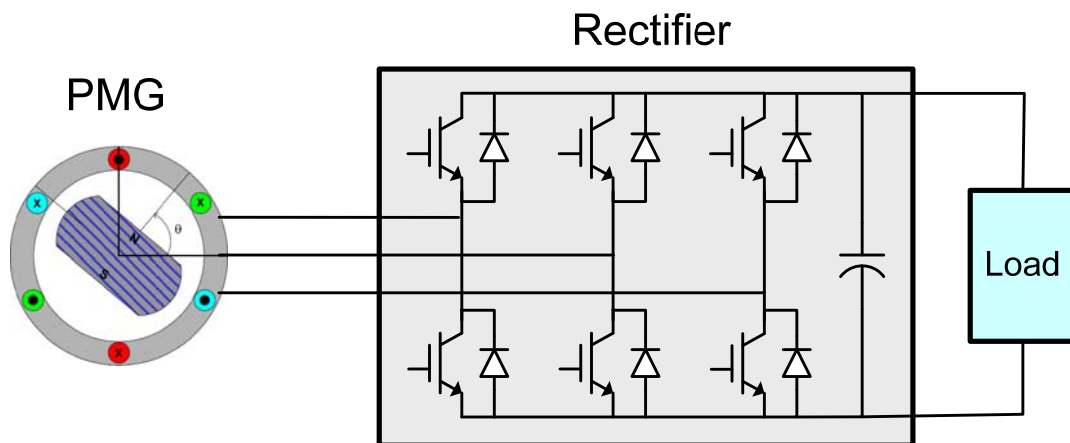


Figure 2-1 Power stage configuration of the PMG and rectifier system

2.1.1 Permanent Magnet Generator

There are two PM synchronous machine types, the surface-mounted PM (SPM) and the interior-buried PM (IPM). The magnets of the SPM machine are attached on the surface of the rotor, while the IPM machine is buried inside. Due to the structure, the rotor of the SPM machine does not have saliency. The inductance measured at the motor terminal is constant regardless of the rotor position. For the IPM, however, the reluctance of the magnetic flux path varies according to the rotor position, as shown in Figure 2-2. [1] Because of it, the inductance at the motor terminal varies according to the rotor position. Due to the inductance saliency, the control for an IPM machine is more difficult than SPM machine. The IPM machine is used under study and simulation verification.

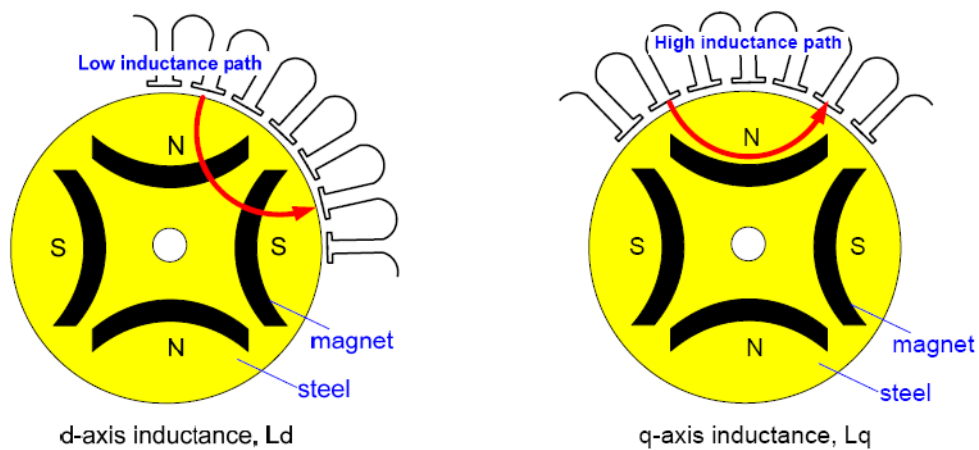


Figure 2-2 Magnetic saliency of IPM machine [7]

The parameters of the IPM generator are shown in Table 2-1. From Table 2-1, the stator inductance on d axis and q axis are really high, which does give us the opportunity to connect the PMG to rectifier directly without any other passive component to limit ac side harmonic currents, which can also be seen in the next section.

Table 2-1 Parameters of the PMG

Parameter	Symbol	Value
Stator resistance	R_s	3.4Ω
D axis stator inductance	L_d	27.5mH
Q axis stator inductance	L_q	41.2mH
Back EMF constant	λ_m	0.4022Wb
Nominal power	P_n	400W
Nominal voltage	V_n	107V
Nominal frequency	f	60Hz

2.1.2 Passive Components Selection of the Boost Rectifier

The passive components (boost inductors and DC bus capacitor) play an important role in the dynamic behavior of the system. [26][27][28] On one side, lower boost inductance means faster system dynamic response. On the other side, the boost inductor needs to attenuate the harmonic components caused by rectifier switching. So the value of boost inductance should be high enough so that the total harmonic distortion (THD) of input currents can meet the specified THD requirement. The minimum inductance value is a function of switching frequency ratio, for different THD values as shown in Figure 2-3. [1] In our case, the switching frequency is $f_s=20k$. So the per unit reactance is chosen to be 10% so that the current THD is below 2%. The desired boost inductance is given by

$$L = \frac{Z_B X_s}{2\pi f} = 22.8mH \quad (2-1)$$

For the PMG selected in the study, the PMG stator inductances L_d (27.5mH) and L_q (41.2mH) are larger than the desired boost inductance, which eliminates the need for additional passive components between the generator and the rectifier.

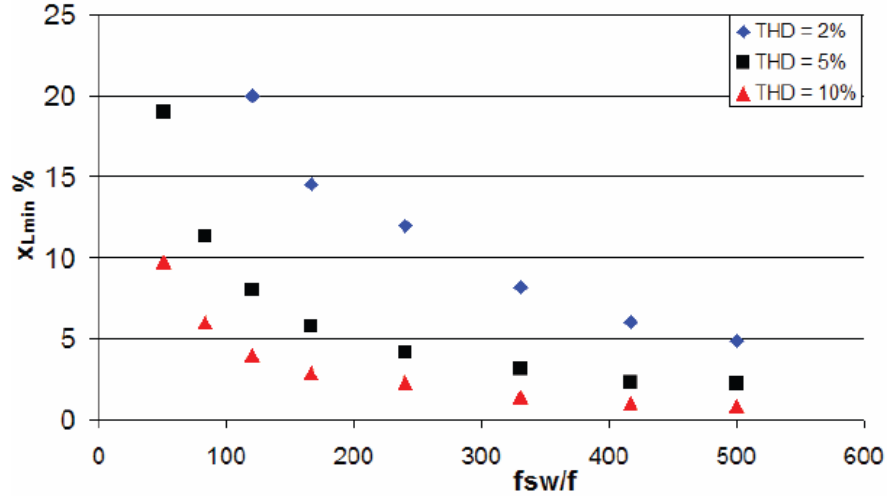


Figure 2-3 Minimum inductance L_{min} required at different switching frequency for three different THD specifications [26]

The selection of dc-link capacitor should consider two constraints: the energy storage or ripple voltage limit, the total dc side ripple current limit. Because power rating of the system under study is low, the dc side ripple current has not reached the limit which can be seen in the experimental results, only the first constraint is used to calculate the capacitance needed.

Assuming that in one switching cycle, when the rectifier input power is zero and the output power reaches maximum level, the voltage dip should be less than 0.25%, the desired capacitance can be calculated as:

$$C = \frac{P_{\max}}{(V_{dc}\Delta U + \frac{1}{2}\Delta U^2)f_s} = 89\mu F \quad (2-2)$$

In summary, the parameters of the active front-end rectifier are shown in Table 2-2.

Table 2-2 Parameters of the active front-end rectifier

Parameter	Symbol	Value
Nominal power	P_n	400W
Reference DC link voltage	V_{dref}	300V
Modulation index	M	0.875
Switching frequency	f_s	20k
DC link capacitor	C	100 μ F

2.2 Permanent Magnet Generator Model

In the study, the PM generator is mounted on the shaft of a significantly larger turbine. Thus the speed of the PM generator will not be affected by the load power rating. In other words, the output frequency won't change during operation, no matter heavy load or light load is connect. This can simplify the control system design.

The dynamic d-q model is used for the PMG to eliminate the time-varying inductances. The variables in a-b-c coordinates are transformed to d-q coordinates with the Park transformation, as shown in the following matrix equation.

$$\begin{bmatrix} i_d \\ i_q \\ i_0 \end{bmatrix} = \sqrt{\frac{2}{3}} \begin{bmatrix} \sin \omega t & \sin(\omega t - \frac{2}{3}\pi) & \sin(\omega t + \frac{2}{3}\pi) \\ \cos \omega t & \cos(\omega t - \frac{2}{3}\pi) & \cos(\omega t + \frac{2}{3}\pi) \\ \frac{1}{2} & \frac{1}{2} & \frac{1}{2} \end{bmatrix} \begin{bmatrix} i_a \\ i_b \\ i_c \end{bmatrix} \quad (2-3)$$

The structure of the stator in a PMG is similar to that of the wound rotor in a synchronous generator. In addition there is no difference between the back EMF produced by a permanent magnet and that produced by an excited coil. Hence the mathematical model of a PMG can be derived from the model of a synchronous generator. The only difference is the equations of the

damper windings and the field current dynamics can be removed. Finally, the equivalent circuits of d-axis and q-axis of a permanent magnet synchronous generator are illustrated in Figure 2-4.

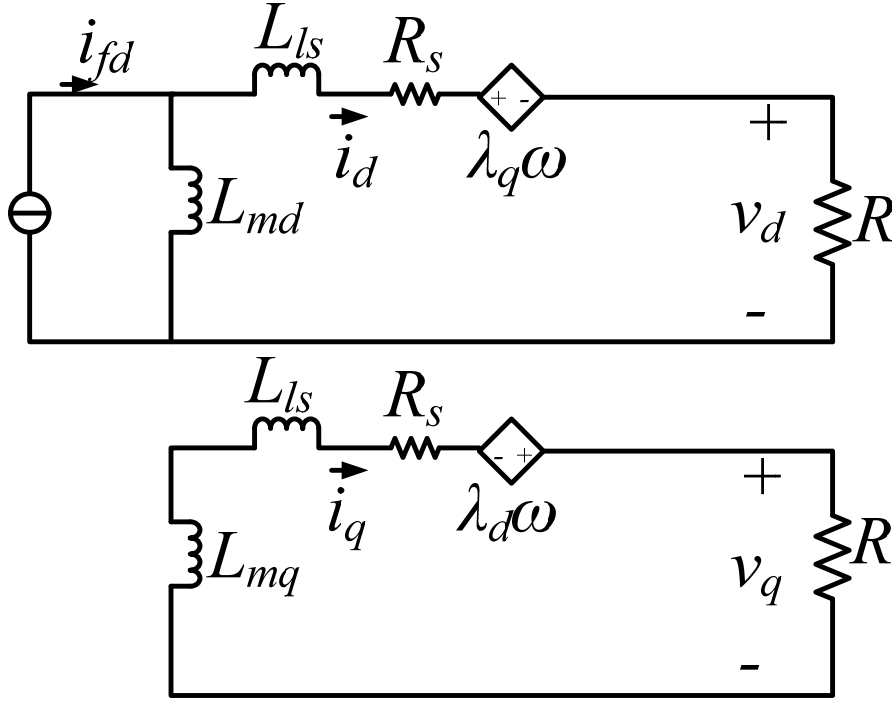


Figure 2-4 Equivalent circuits of the permanent magnet synchronous generator in d-q axes

The state-space equations for PMG are given by

$$\begin{aligned}
 v_d &= -R_s i_d - \omega \lambda_q + \frac{d\lambda_d}{dt} \\
 v_q &= -R_s i_q - \omega \lambda_d + \frac{d\lambda_q}{dt} \\
 \lambda_d &= -(L_{ls} + L_{md}) i_d + L_{md} i_{fd} \\
 \lambda_q &= -(L_{ls} + L_{mq}) i_q \\
 \lambda_m &= L_{md} i_{fd}
 \end{aligned} \tag{2-4}$$

In the model, the current i_{fd} is the equivalent magnetizing current for the permanent magnet referred to the stator side. The currents i_d , i_q and the voltages v_d , v_q represent the stator d and q currents and voltages respectively. L_{ls} and R_s represent the armature resistance and leakage

inductance. L_{md} and L_{mq} represent the d and q magnetizing inductances. λ_d and λ_q represent the magnetic flux in the d-q axes. And ω represents the electrical angular velocity. [29] - [33]

2.3 Two-level Active Rectifier Model

The topology of the two level three phase boost rectifier is shown in Figure 2-5. In Figure 2-5, each switch symbol stands for a switch pair composed of an IGBT and an anti-parallel diode, which could be modeled as a current bi-directional two-quadrant switch.

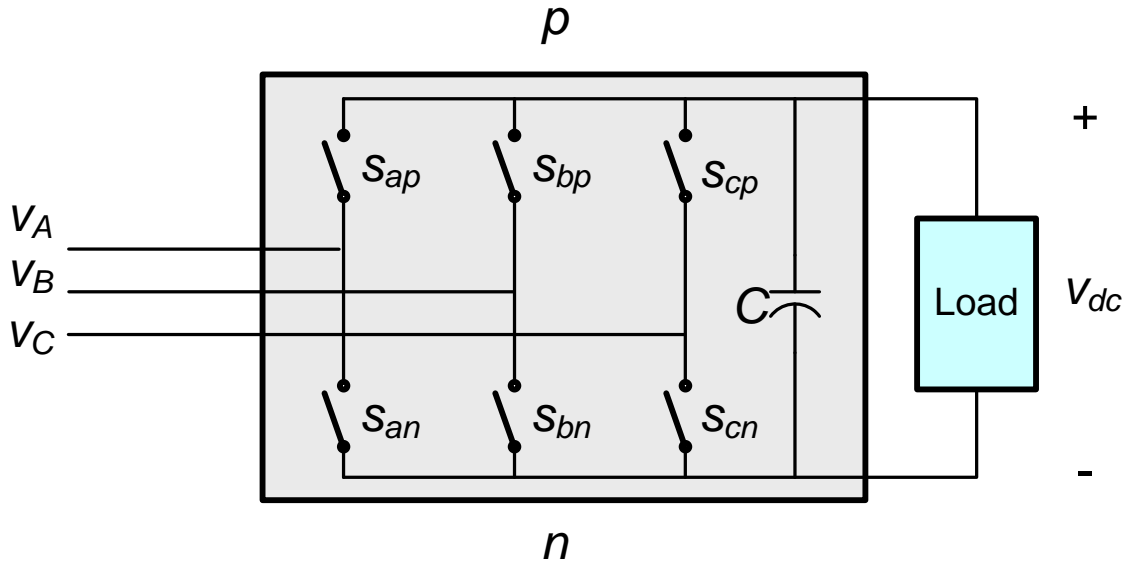


Figure 2-5 Switching model of the boost rectifier

The single-pole, single-throw switching function is defined as:

$$s = \begin{cases} 1, v = 0, \text{ if switch is closed} \\ 0, i = 0, \text{ if switch is open} \end{cases} \quad (2-5)$$

The allowed switching combinations are given by

$$s_{ip} + s_{in} = 1 \quad (i = a, b, c) \quad (2-6)$$

Furthermore, the single-pole, double-throw switching function could be defined as

$$s_i = s_{ip} = 1 - s_{in} \quad (i = a, b, c) \quad (2-7)$$

The switching function model is then implemented with the following input and output relationships equations.

$$\begin{bmatrix} v_A \\ v_B \\ v_C \end{bmatrix} = \begin{bmatrix} s_a \\ s_b \\ s_c \end{bmatrix} \cdot v_{dc} \quad (2-8)$$

$$i_{dc} = \begin{bmatrix} s_a & s_b & s_c \end{bmatrix} \cdot \begin{bmatrix} i_a \\ i_b \\ i_c \end{bmatrix} \quad (2-9)$$

By applying an average operator $\bar{x}(t) = \frac{1}{T} \int_{t-T}^t x(\tau) d\tau$ to the switching model, the average model of the three phase boost rectifier is derived. The equivalent circuit is shown in Figure 2-6.

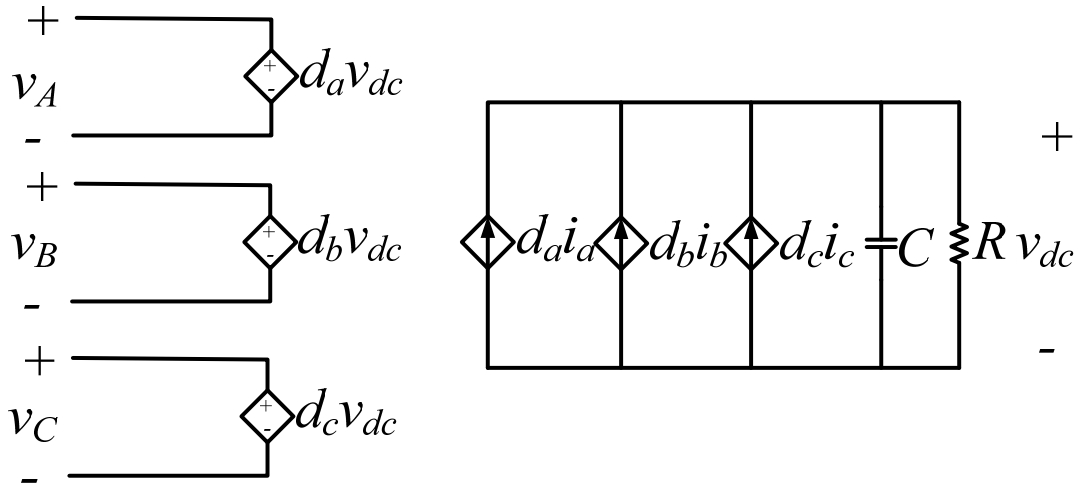


Figure 2-6 Equivalent circuit of VSR average model in a-b-c coordinates

In the average model in a-b-c coordinates, the three phase input voltages and currents are sinusoidal, which is difficult for us to find an operating point to linearize the model. Therefore, the average model in d-q coordinates is developed with the Park transformation. The equivalent circuit in d-q coordinates is shown in Figure 2-7, which will be used in this study.

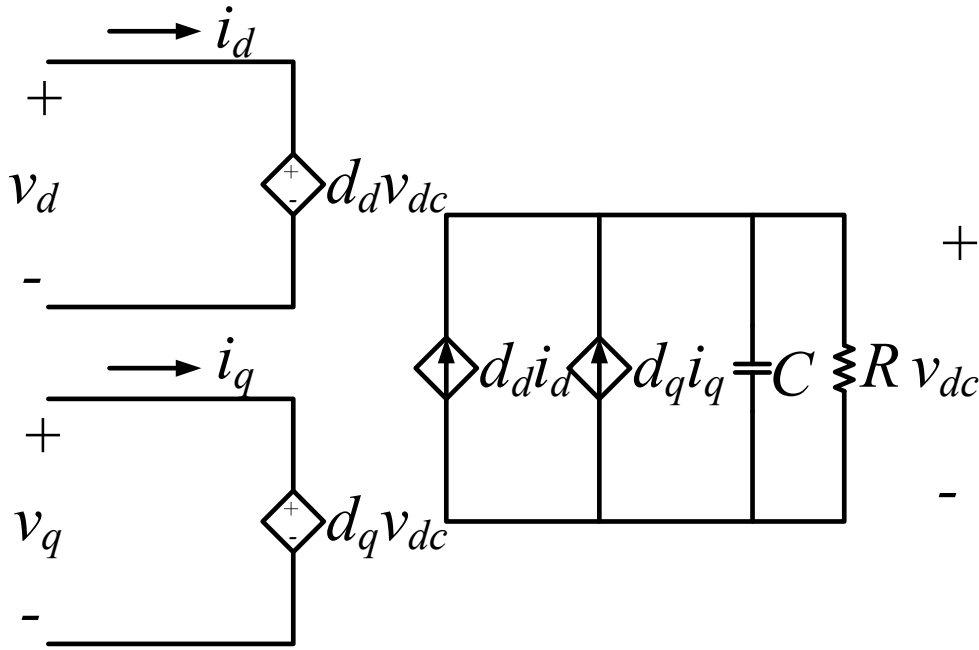


Figure 2-7 Equivalent circuit of VSR average model in d-q coordinates

2.4 PMG and Rectifier System Model

To realize the unified control of PWM and rectifier system, the model of PMG and rectifier system presented in last sections are combined together as shown in Figure 2-8. As discussed above, there are no additional passive components between the PMG and the rectifier. The PMG and the boost rectifier are modeled in the same d-q coordinates, in which the flux is on the d axis and the back EMF is on the q axis.

For the transformation between abc and dq coordinates, the rotor position should be acquired. As a result, either the rotor position sensor or a sensorless control strategy is needed to get the rotor position. In the project, an observer and a tracking controller is applied for the sensorless vector control, which will be discussed in details in later chapters.

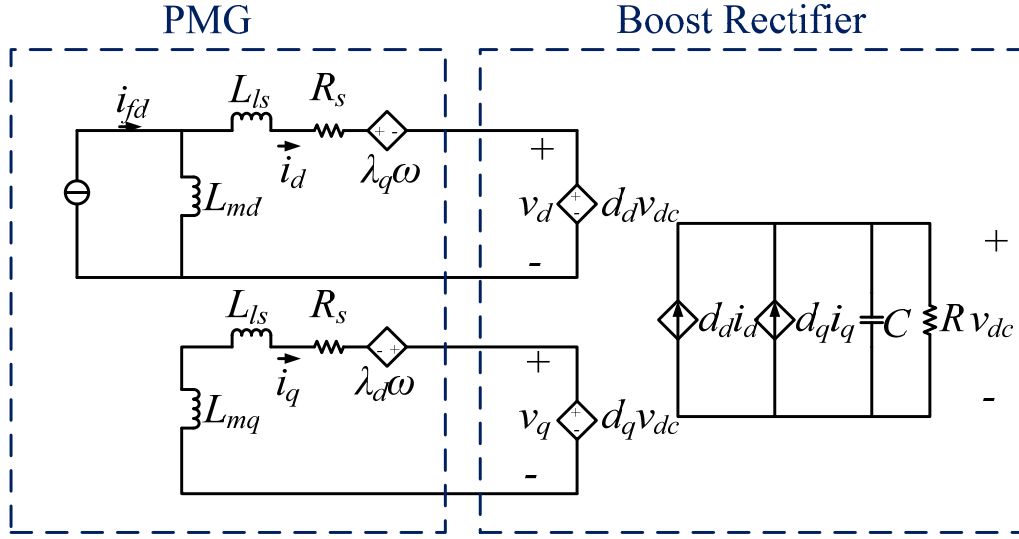


Figure 2-8 Model of PMG and rectifier system

From the average model in Figure 2-8, the state-space equations for PMG and rectifier system are given by

$$\begin{aligned}
 v_d &= -R_s i_d - \omega \lambda_q + \frac{d\lambda_d}{dt} \\
 v_q &= -R_s i_q + \omega \lambda_d + \frac{d\lambda_q}{dt} \\
 \lambda_d &= -(L_{ls} + L_{md}) i_d + L_{md} i_{fd} \\
 \lambda_q &= -(L_{ls} + L_{mq}) i_q \\
 \lambda_m &= L_{md} i_{fd} \\
 C \frac{dv_{dc}}{dt} &= d_d i_d + d_q i_q - \frac{v_{dc}}{R}
 \end{aligned} \tag{2-10}$$

As well known, to design the controller for closed-loop control, the small-signal models are necessary. And the classic control methods like bode plots can also be used in the small signal-models.

From the average model, the state-space equations in matrix form is given by

$$\begin{aligned}
\frac{d}{dt} \begin{bmatrix} \bar{i}_d \\ \bar{i}_q \end{bmatrix} &= \frac{1}{L_{ls} + L_{mq}} \begin{bmatrix} 0 \\ \omega L_{md} i_{fd} \end{bmatrix} - \begin{bmatrix} \frac{R_s}{L_{ls} + L_{md}} & -\frac{L_{ls} + L_{mq}}{L_{ls} + L_{md}} \omega \\ \frac{L_{ls} + L_{mq}}{L_{ls} + L_{md}} \omega & \frac{R_s}{L_{ls} + L_{mq}} \end{bmatrix} \cdot \begin{bmatrix} \bar{i}_d \\ \bar{i}_q \end{bmatrix} - \begin{bmatrix} \frac{d_d}{L_{ls} + L_{md}} \\ \frac{d_q}{L_{ls} + L_{mq}} \end{bmatrix} \cdot \bar{v}_{dc} \\
\frac{d\bar{v}_{dc}}{dt} &= \frac{1}{C} \cdot \begin{bmatrix} d_d & d_q \end{bmatrix} \cdot \begin{bmatrix} \bar{i}_d \\ \bar{i}_q \end{bmatrix} - \frac{\bar{v}_{dc}}{RC}
\end{aligned} \tag{2-11}$$

However, the average model is time-invariant but nonlinear. To derive the small signal model, the model is linearized by giving a perturbation at the steady-state operating point. The small-signal model is then derived as below.

$$\begin{aligned}
\frac{d}{dt} \begin{bmatrix} \tilde{i}_d \\ \tilde{i}_q \end{bmatrix} &= - \begin{bmatrix} \frac{R_s}{L_{ls} + L_{md}} & -\frac{L_{ls} + L_{mq}}{L_{ls} + L_{md}} \omega \\ \frac{L_{ls} + L_{mq}}{L_{ls} + L_{md}} \omega & \frac{R_s}{L_{ls} + L_{mq}} \end{bmatrix} \cdot \begin{bmatrix} \tilde{i}_d \\ \tilde{i}_q \end{bmatrix} - \begin{bmatrix} \frac{\tilde{d}_d}{L_{ls} + L_{md}} \\ \frac{\tilde{d}_q}{L_{ls} + L_{mq}} \end{bmatrix} \cdot V_{dc} - \begin{bmatrix} \frac{D_d}{L_{ls} + L_{md}} \\ \frac{D_q}{L_{ls} + L_{mq}} \end{bmatrix} \cdot \tilde{v}_{dc} \\
\frac{d\tilde{v}_{dc}}{dt} &= \frac{1}{C} \cdot \begin{bmatrix} \tilde{d}_d & \tilde{d}_q \end{bmatrix} \cdot \begin{bmatrix} I_d \\ I_q \end{bmatrix} + \frac{1}{C} \cdot \begin{bmatrix} D_d & D_q \end{bmatrix} \cdot \begin{bmatrix} \tilde{i}_d \\ \tilde{i}_q \end{bmatrix} - \frac{\tilde{v}_{dc}}{RC}
\end{aligned} \tag{2-12}$$

That is,

$$\frac{d}{dt} \begin{bmatrix} \tilde{i}_d \\ \tilde{i}_q \\ \tilde{v}_{dc} \end{bmatrix} = \begin{bmatrix} -\frac{R_s}{L_{ls} + L_{md}} & \frac{L_{ls} + L_{mq}}{L_{ls} + L_{md}} \omega & -\frac{D_d}{L_{ls} + L_{md}} \\ -\frac{L_{ls} + L_{mq}}{L_{ls} + L_{md}} \omega & -\frac{R_s}{L_{ls} + L_{mq}} & -\frac{D_q}{L_{ls} + L_{mq}} \\ \frac{D_d}{C} & \frac{D_q}{C} & -\frac{1}{RC} \end{bmatrix} \cdot \begin{bmatrix} \tilde{i}_d \\ \tilde{i}_q \\ \tilde{v}_{dc} \end{bmatrix} + \begin{bmatrix} -\frac{V_{dc}}{L_{ls} + L_{md}} & 0 \\ 0 & -\frac{V_{dc}}{L_{ls} + L_{mq}} \\ \frac{I_d}{C} & \frac{I_q}{C} \end{bmatrix} \cdot \begin{bmatrix} \tilde{d}_d \\ \tilde{d}_q \end{bmatrix} \tag{2-13}$$

This is the final small signal model for the PMG and rectifier system, which is the basis for controller design in the next chapter.

Chapter 3 Control Design for PMG and Rectifier System

Based on the model developed in last chapter, this chapter presents the unified control method for PMG and rectifier system. First, the structure of the whole control system is explained. After that, design procedure for each control loops are presented in detail, including current control loop, voltage control loop, reactive control loop and sensorless vector control loop. The performance of the designed control system is analyzed and verified by simulation results.

3.1 *Structure of Proposed Unified Control System*

Figure 3-1 depicts the schematic of the proposed unified control method of the system, which includes three control loops. The first part is inner current loop. Two inner current loops are involved to control the ac current in d-q axes respectively. The second part is the outer voltage loop for dc output voltage regulation, which controls the instantaneous active power by generating the i_q command. The third part is the instantaneous reactive power loop, which can control the converter active power via i_d command. Additionally, an observer and a tracking controller are used to find the rotor position and speed for the d-q coordinates transformation, which is also called sensorless control. With the proposed control method, both the DC link voltage and reactive power could be controlled accurately.

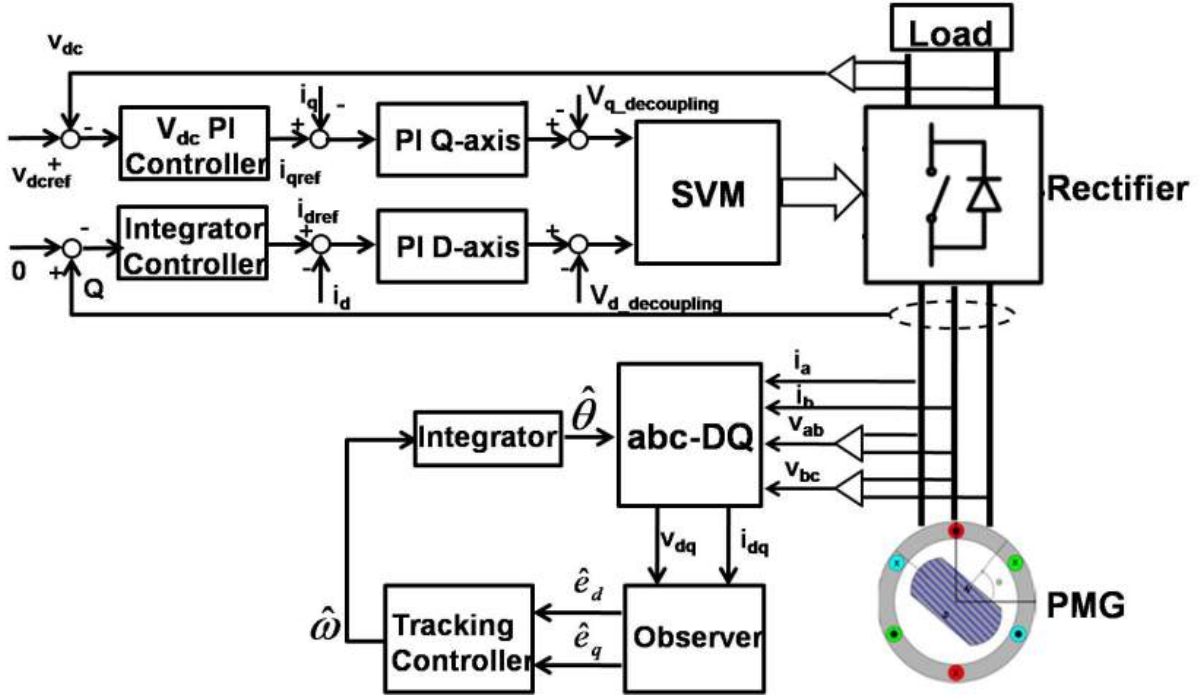


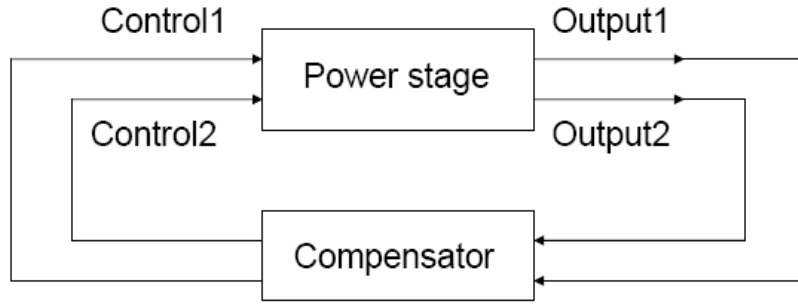
Figure 3-1 Control Schematic of PMG and rectifier system

3.2 Inner Current Loop Design

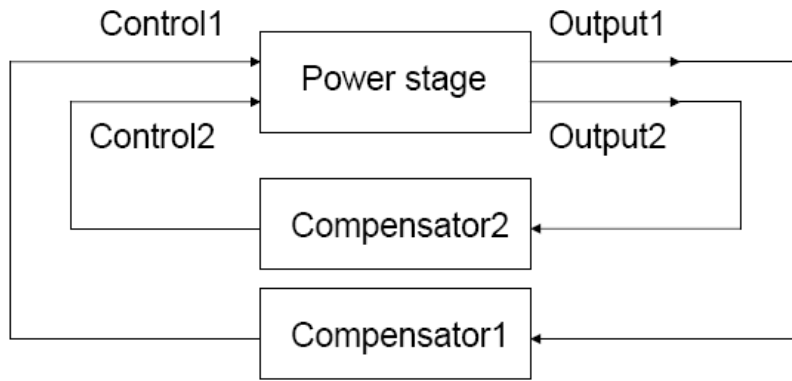
The inner current loops are designed to control the converter current in d-q coordinates. A simple PI controller structure is used for the current loops in this study as shown in Figure 3-1. The parameters used for the current loops design are obtained from the permanent magnet generator model developed in last chapter. Especially, the d-q decoupling is considered to cancel out the dynamic interactions between the two current loops.

3.2.1 D-Q Decoupling

From the small signal model, i_d and i_q both are related to d_d and d_q . In other words, the system is a multi-input-multi-output (MIMO) system. To simplify the system to two single-input-single-output (SISO) systems, decoupling components are added to the control system. Figure 3-2 shows the two structures of the MIMO and SISO. Control 1 and 2 indicate d_d and d_q and output 1 and 2 indicate i_d and i_q in our study.



(a) Multi-Input-Multi-Output Structure



(b) Single-Input-Single-Output Structure

Figure 3-2 Multi-Input-Multi-Output vs. Single-Input-Single-Output structures

The output of the current controller in d axis is modified from $\hat{d}_d = (i_{dref} - \hat{i}_d)H_{id}$ to $\hat{d}_d = (i_{dref} - \hat{i}_d)H_{id} - \omega(L_{ls} + L_{mq})\hat{i}_q / V_{dc}$. By adding the decoupling terms, the output of the voltage controlled voltage source in d axis can be expressed by

$$\hat{d}_d \cdot V_{dc} = (i_{dref} - \hat{i}_d)H_{id}V_{dc} - \omega(L_{ls} + L_{mq})\hat{i}_q \quad (3-1)$$

The additional part $\omega(L_{ls} + L_{mq})\hat{i}_q$ compensates the influence from q axis. After the D-Q decoupling, the equivalent circuit is similar to two parallel dc-dc boost converters, as shown in Figure 3-3.

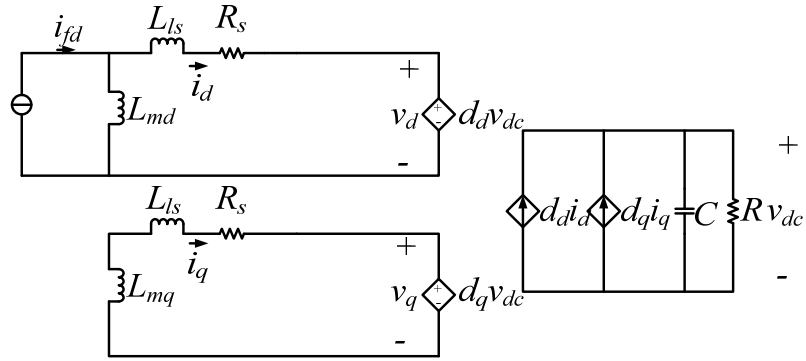


Figure 3-3 Decoupled D and Q channels

The control schematic with D-Q decoupling is shown in Figure 3-4.

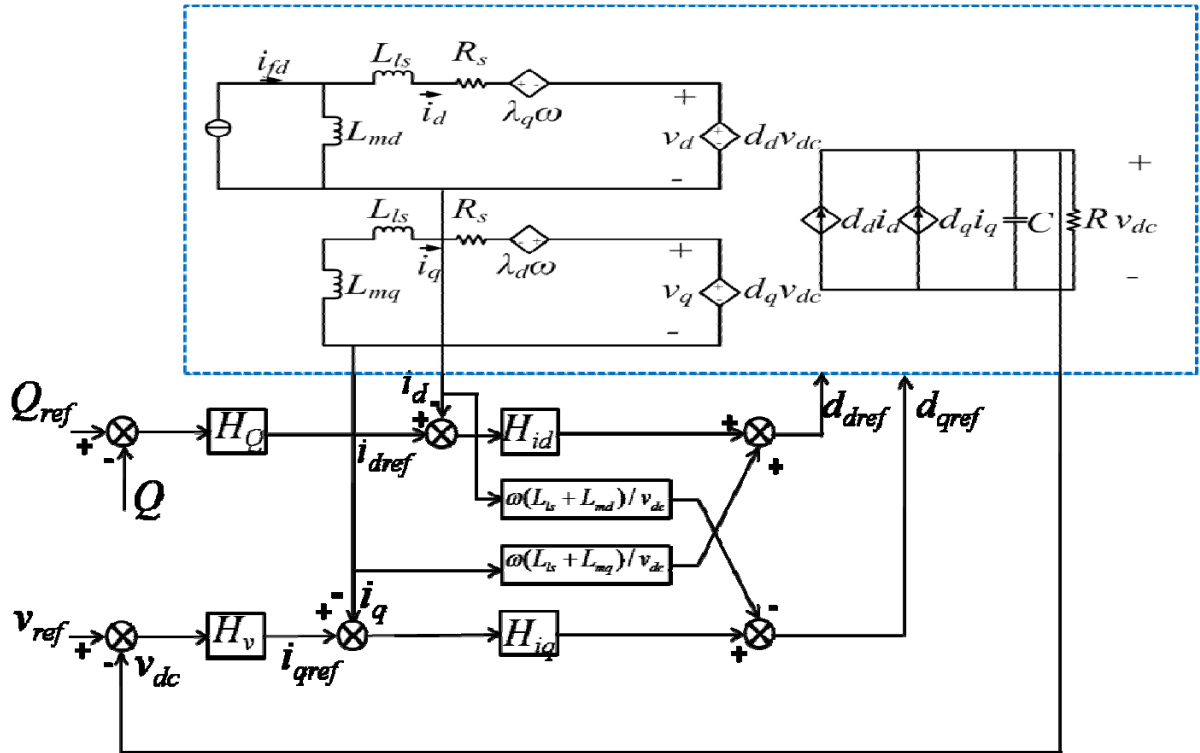


Figure 3-4 Control schematic with D-Q decoupling

3.2.2 Compensator Design

Since the inner current loops are supposed to be much faster than outer voltage loops, DC output voltage V_{dc} can be considered as constant when designing the current controller. After D-Q decoupling, the control to current transfer functions in d and q axes are derived as

$$\frac{\hat{i}_d(s)}{\hat{d}_d(s)} = -\frac{V_{dc}}{(L_{ls} + L_{md}) \cdot s + R_s} \quad (3-2)$$

$$\frac{\hat{i}_q(s)}{\hat{d}_q(s)} = -\frac{V_{dc}}{(L_{ls} + L_{mq}) \cdot s + R_s} \quad (3-3)$$

A proportional integral compensator is designed to achieve the requirement in dynamic performance and stability. To make the dynamics of the whole system as a one stage system, the PI zero is set to cancel out the machine dynamics and an integrator and gain is selected for desired bandwidth and phase margin.

$$H_{id}(s) = k_{pid} + \frac{k_{iid}}{s} = -\frac{\omega_i(L_{ls} + L_{md})}{V_{dc}} \frac{s + \frac{R_s}{L_{ls} + L_{md}}}{s} \quad (3-4)$$

$$H_{iq}(s) = k_{piq} + \frac{k_{iiq}}{s} = -\frac{\omega_i(L_{ls} + L_{mq})}{V_{dc}} \frac{s + \frac{R_s}{L_{ls} + L_{mq}}}{s} \quad (3-5)$$

where ω_i is the desired current loop control bandwidth.

By multiplying the control to current transfer function in (3-2) and function of the compensator in (3-4), the current loop gain can be found as

$$H_{id}(s) \cdot \frac{\hat{i}_d(s)}{\hat{d}_d(s)} = \frac{\omega_i}{s} \quad (3-6)$$

$$H_{iq}(s) \cdot \frac{\hat{i}_q(s)}{\hat{d}_q(s)} = \frac{\omega_i}{s} \quad (3-7)$$

Then the closed current loops transfer functions are

$$\frac{\hat{i}_d(s)}{\hat{d}_{dref}(s)} = \frac{\omega_i}{s + \omega_i} \quad (3-8)$$

$$\frac{\hat{i}_q(s)}{\hat{d}_{qref}(s)} = \frac{\omega_i}{s + \omega_i} \quad (3-9)$$

The system is controlled to be like a first stage system as desired.

3.2.3 Small-signal Analysis in Saber

An average model is built in Saber to perform the small-signal analysis. The parameters of the compensators are obtained from last section and the PMG is modeled in MAST language based on its state-space equations in (2-4).

The verification approach of the D-Q axes compensator is shown below. First, with all the current loops and voltage loop open, the D axis control to current transfer function is measured. So the D axis current loop gain can be obtained. Then with D axis current loop closed, Q axis control to current transfer function is measured. Finally the loop gain the Q axis compensator H_{iq} is obtained.

Figure 3-5 and Figure 3-6 depict the D channel current loop gain after compensation and the method for measurement. With Q axis current loop open, D_q and I_{dref} are given to provide the steady state operating point. After that an AC perturbation is added in the D axis current loop. Then the D axis loop gain could be derived as B/A.

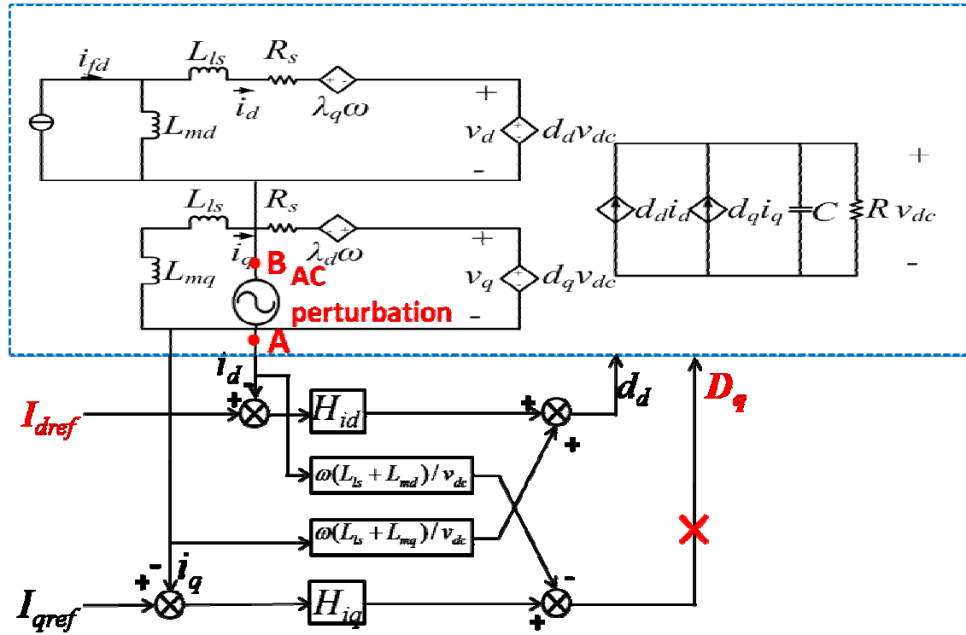


Figure 3-5 Circuit for measuring D channel current loop gain

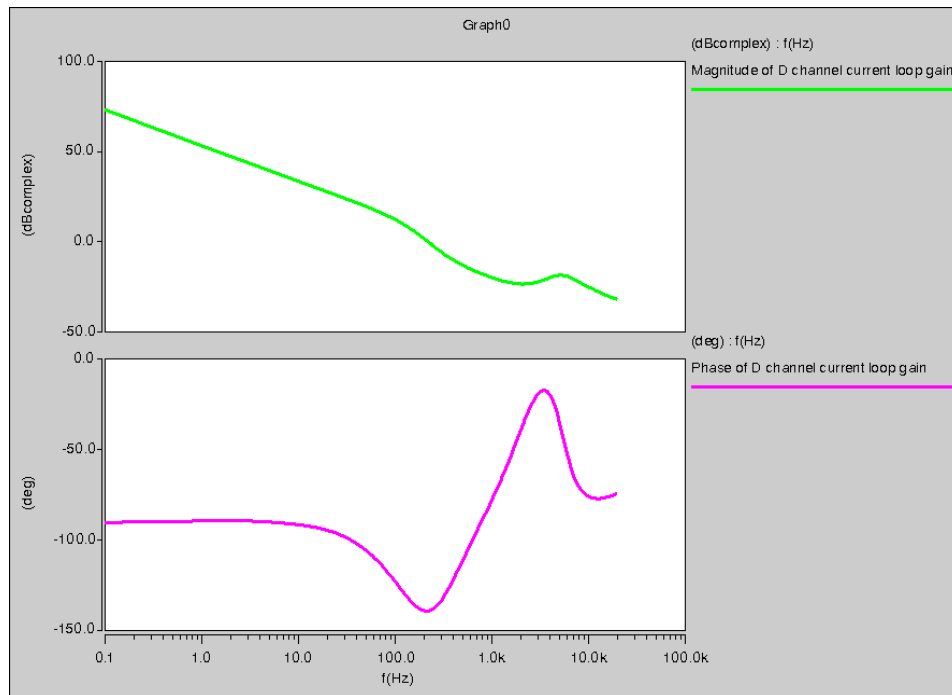


Figure 3-6 Bode magnitude and phase diagrams of D channel current loop gain

Figure 3-7 and Figure 3-8 depict the Q channel current loop gain after compensation of both current loops and the method for measurement. With voltage loop open and D and Q axes

current loop closed, I_{dref} and I_{qref} are given to provide the steady state operating point. An AC perturbation is added in the Q axis current loop. Then the Q axis loop gain could be derived as B/A.

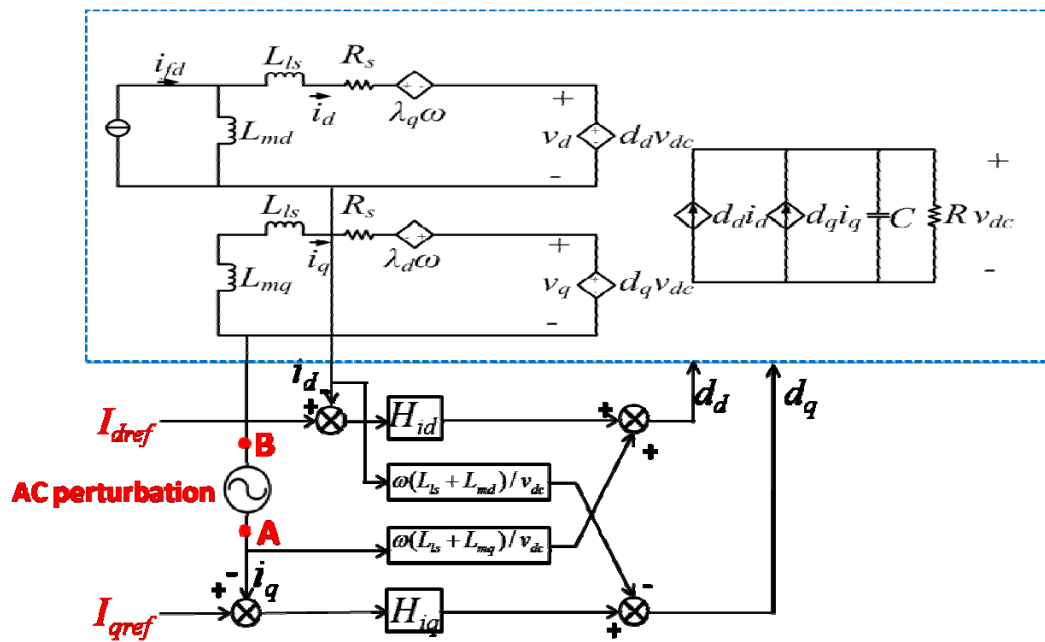


Figure 3-7 Circuit for measuring Q channel current loop gain

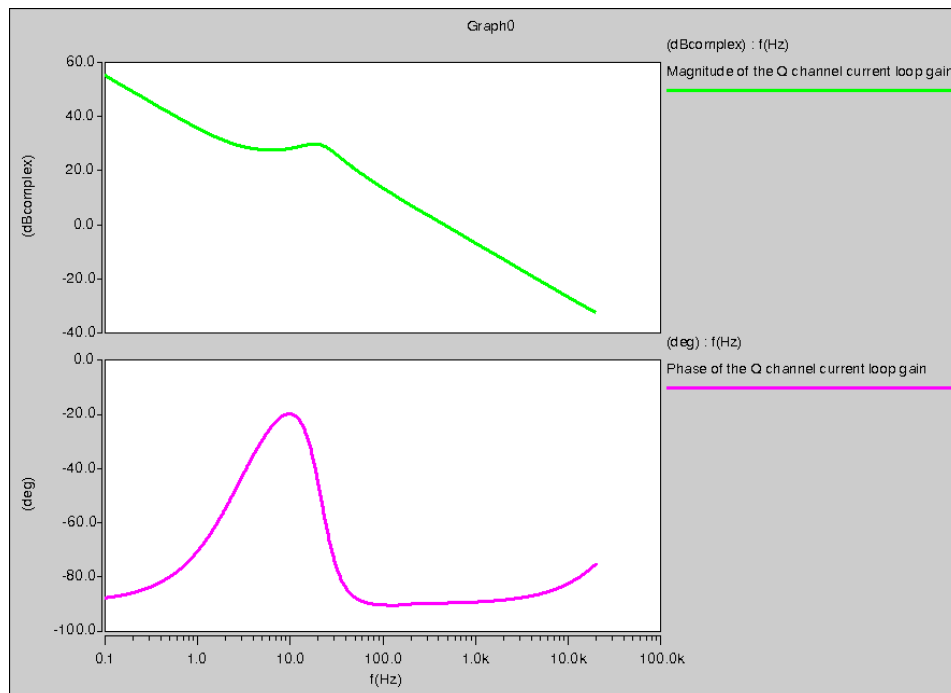


Figure 3-8 Bode magnitude and phase diagrams of Q channel current loop gain

The current loops in d and q axes are verified by simulation. The average model is not correct above half of the switching frequency. In our case the switching frequency is 20 kHz, so all the bode plots are drawn from 0.1 Hz to 10 kHz. The delay is not included in the simulation. From the bode plots of the current loops, the system achieves the desired bandwidth and phase margin.

3.3 Outer Voltage Loop Design

3.3.1 Compensator Design

Figure 3-9 depicts the schematic of the voltage controller. The outer voltage loop regulates the dc link voltage. The output of the controller provides the reference of the q-axis current. H_v is the transfer function of the compensator.

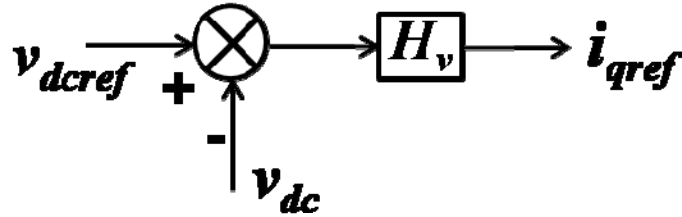


Figure 3-9 Schematic of voltage controller

From state-space equations, the current to voltage transfer function is given by

$$\frac{d\tilde{v}_{dc}}{dt} = \frac{1}{C} \cdot \begin{bmatrix} \tilde{d}_d & \tilde{d}_q \end{bmatrix} \cdot \begin{bmatrix} I_d \\ I_q \end{bmatrix} + \frac{1}{C} \cdot \begin{bmatrix} D_d & D_q \end{bmatrix} \cdot \begin{bmatrix} \tilde{i}_d \\ \tilde{i}_q \end{bmatrix} - \frac{\tilde{v}_{dc}}{RC} \quad (3-10)$$

Some approximations are made to simplify the derivation of the current to voltage transfer function. In unity power factor control at back EMF side, $I_q = \tilde{i}_q = 0$. The equation above could be simplified to

$$\frac{d\tilde{v}_{dc}}{dt} = \frac{1}{C} \cdot \tilde{d}_d \cdot I_d + \frac{1}{C} \cdot D_d \cdot \tilde{i}_d - \frac{\tilde{v}_{dc}}{RC} \quad (3-11)$$

Since the current loops are much faster than the voltage loop, $\frac{1}{C} \cdot \tilde{d}_d \cdot I_d$ could be regarded as the perturbations to output voltage. Then the current to voltage transfer function is given by

$$\frac{v_{dc}}{i_q} = -\frac{D_q}{C \cdot s + \frac{1}{R}} \quad (3-12)$$

Designing a proportional integral transfer compensator from the transfer function

$$H_v(s) = -\frac{\omega_v C}{D_q} \cdot \frac{s + \frac{1}{RC}}{s} \quad (3-13)$$

So the outer voltage loop gain can be found as

$$H_v(s) \cdot \frac{v_{dc}}{i_q} = \frac{\omega_v}{s} \quad (3-14)$$

The closed current loop is

$$\frac{\hat{i}_d(s)}{\hat{d}_{dref}(s)} = \frac{\omega_i}{s + \omega_i} \quad (3-15)$$

3.3.2 Small Signal Analysis in Saber

A small signal analysis in Saber is complemented to verify the voltage loop design. First, the Q channel current to voltage transfer function is obtained. Then the voltage compensator is added and the voltage loop gain is measured.

Figure 3-10 and Figure 3-11 depict the outer voltage loop gain and the method for measurement. With both of the voltage loop and current loops closed, an AC perturbation is added in the outer voltage loops. The outer voltage loop gain could be derived as B/A.

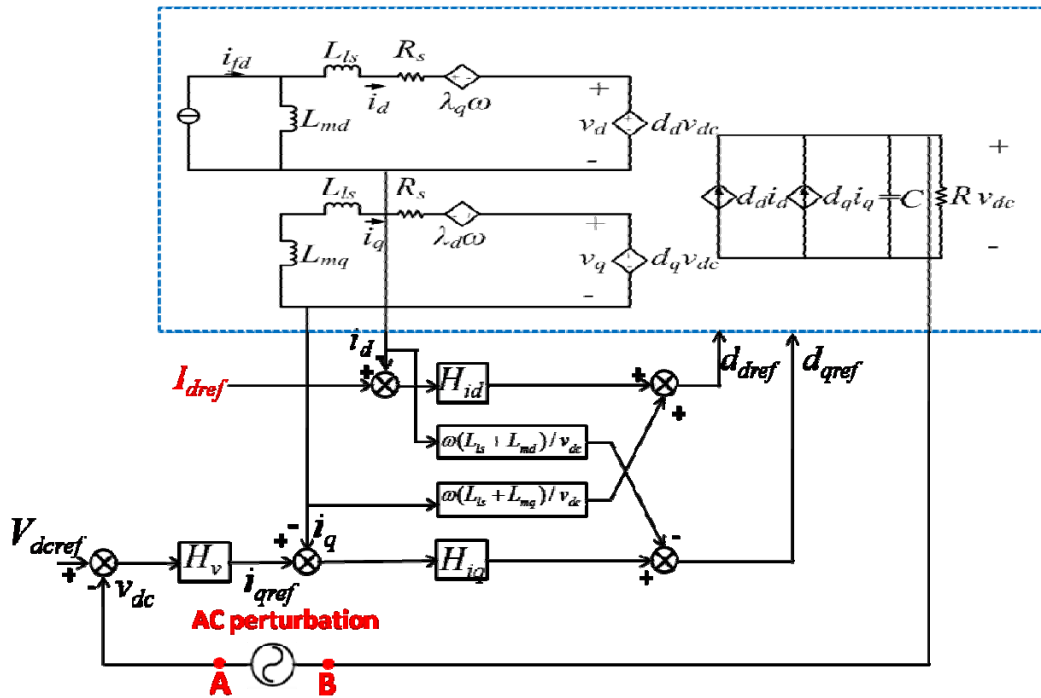


Figure 3-10 Circuit for measuring Q outer voltage loop gain

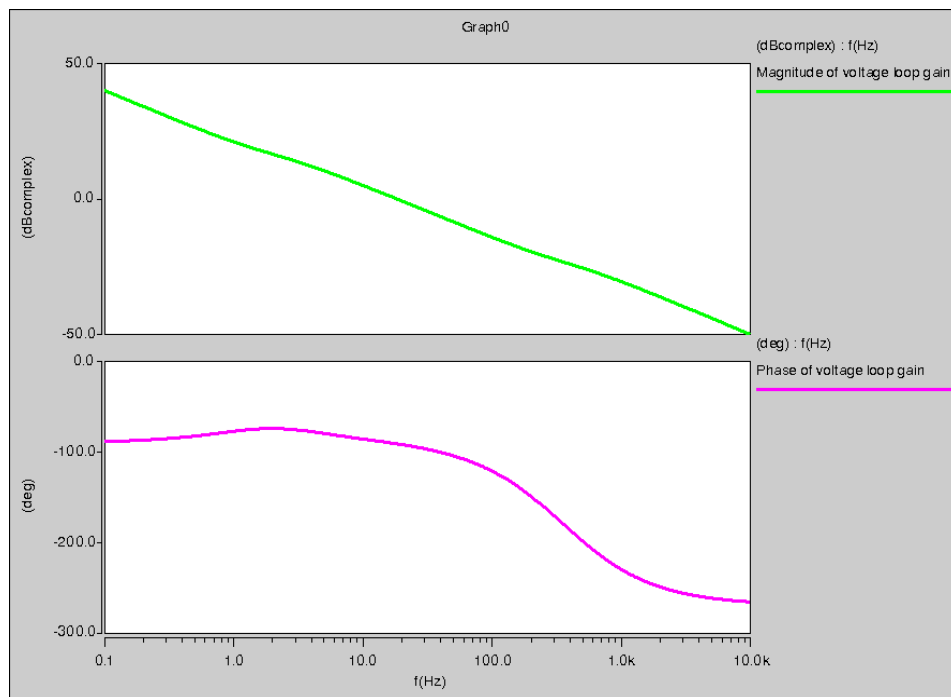


Figure 3-11 Bode magnitude and phase diagrams of outer voltage loop gain

From the bode plots of the voltage loop, the system achieves the desired bandwidth and phase margin.

3.4 Instantaneous Reactive Power Loop Control

The q-axis current component controls the active power while the d-axis current component controls the reactive power. [34] - [39] The outer reactive power loop regulates the instantaneous reactive power in the system. Instantaneous reactive power in abc coordination can be given by

$$Q = \frac{1}{\sqrt{3}}[(u_b - u_c)i_a + (u_c - u_a)i_b + (u_a - u_b)i_c] \quad (3-16)$$

Then an integrator compensator is designed for desired bandwidth and stability.

3.5 Sensorless Vector Control

For the convenience of controller design, the PMG and boost rectifier are modeled on the same d-q axes. The location of the d-q axes is determined by the rotor position independently of the stator voltages and currents. In conventional front-end rectifier, the input AC voltages are sensed and a PLL is employed to locate the d-q axes by regulating q-axes voltage component v_q to be zero. In PMG and rectifier system, however, the back EMF cannot be sensed directly without a transducer such as resolvers or absolute encoders. The PMG terminal voltages and currents are sensed, an additional back EMF observer is needed to calculate the back EMF, and a PLL-based tracking controller located the d-q axes by forcing the d-axes back EMF component to be zero. Figure 3-12 depicts how the d-q axes are located in the front-end rectifier with a PLL. Figure 3-13 depicts how the d-q axes are located in the PMG and rectifier system with a back EMF observer and a PLL-base tracking controller.

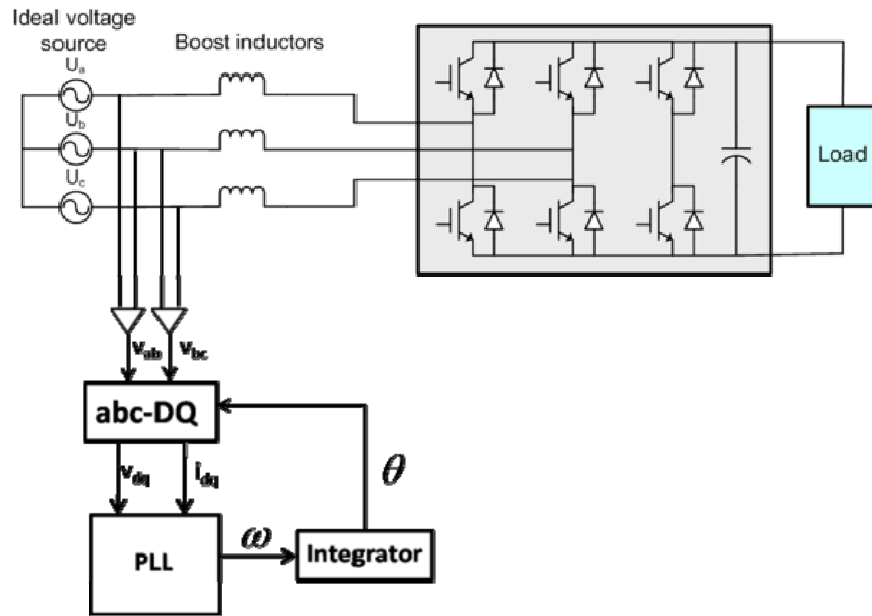


Figure 3-12 Location of d-q axes in the front-end rectifier with a PLL

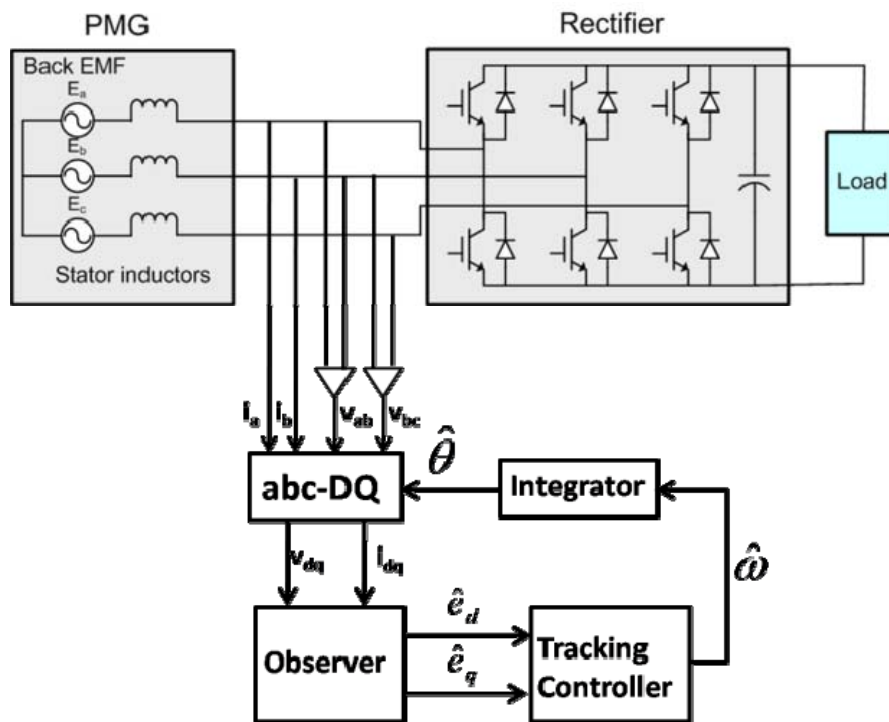


Figure 3-13 Location of d-q axes in the PMG and rectifier system with a back EMF observer and a PLL-based tracking controller

3.5.1 Speed Estimation Strategy

Figure 3-14 illustrated the relationship between the estimated \hat{d} - \hat{q} frame and the actual d-q frame. The relative phase error between the actual and estimated synchronous reference frames is defined as

$$\tilde{\theta} = \theta - \hat{\theta} \quad (3-17)$$

The PMG back EMF voltages in the estimated reference frame is given by (3-18) and (3-19). When the displacement between the estimated frame and actual frame is zero, the PMG back EMF voltage will equal $\omega\lambda_m$ and be reflected on the q-axis.

$$\hat{e}_d = \omega\lambda_m \sin \tilde{\theta} \quad (3-18)$$

$$\hat{e}_q = \omega\lambda_m \cos \tilde{\theta} \quad (3-19)$$

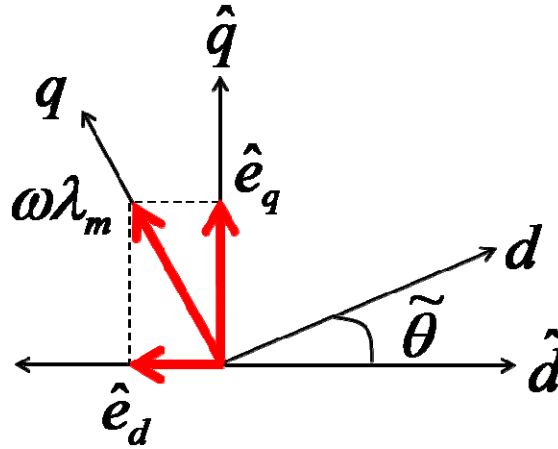


Figure 3-14 Relationship between actual and estimated synchronous reference frames

An observer is employed to estimate the back EMF voltages in the d-q frame to ensure zero steady state error. As shown in (3-18), the estimated voltages determine angular difference between the real and estimated d-q frames. With the error information, the tracking controller generates the estimated speed of PMG and the rotor position by forcing the angular error to be zero.

3.5.2 Back EMF Observer Design

A. Asymptotic Observers

For the linear systems of the following form, an asymptotic state observer could be employed to estimate the state variables, as shown in Figure 3-15.

$$\dot{\mathbf{x}} = \mathbf{Ax} + \mathbf{Bu} \quad (3-20)$$

$$\mathbf{y} = \mathbf{Cx} \quad (3-21)$$

Because the state variables \mathbf{x} is not known, the system outputs \mathbf{u} is used as the feedback. The error signal is used to drive the estimator, which is given by

$$\mathbf{y} - \hat{\mathbf{y}} = \mathbf{Cx} - \mathbf{C}\hat{\mathbf{x}} = \mathbf{C}\tilde{\mathbf{x}} \quad (3-22)$$

The estimator for the state variable \mathbf{x} is given by

$$\dot{\hat{\mathbf{x}}} = \mathbf{A}\hat{\mathbf{x}} + \mathbf{Bu} + \mathbf{LC}\tilde{\mathbf{x}} \quad (3-23)$$

where \mathbf{L} is the feedback gain matrix.

Then the state error dynamics of the asymptotic observer could be described by

$$\dot{\tilde{\mathbf{x}}} = \dot{\mathbf{x}} - \dot{\hat{\mathbf{x}}} = (\mathbf{A} - \mathbf{LC})\tilde{\mathbf{x}} \quad (3-24)$$

The feedback gain matrix \mathbf{L} is selected to achieve the desired dynamic response.

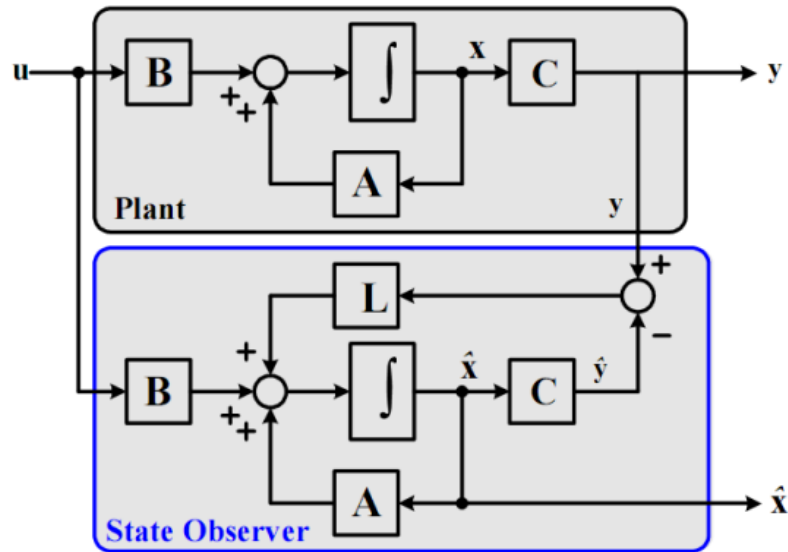


Figure 3-15 Asymptotic state observer block diagram

B. Back EMF Observer

For the PMG and rectifier system, the state space equations in the estimated reference frame is given by

$$\frac{d}{dt} \begin{bmatrix} \hat{i}_d \\ \hat{i}_q \\ \hat{e}_d \\ \hat{e}_q \end{bmatrix} = \begin{bmatrix} -\frac{R_s}{L_s} & \hat{\omega} & \frac{1}{L_s} & 0 \\ -\hat{\omega} & -\frac{R_s}{L_s} & 0 & -\frac{1}{L_s} \\ 0 & 0 & 0 & 0 \\ 0 & 0 & 0 & 0 \end{bmatrix} \cdot \begin{bmatrix} \hat{i}_d \\ \hat{i}_q \\ \hat{e}_d \\ \hat{e}_q \end{bmatrix} + \begin{bmatrix} \frac{1}{L_s} & 0 \\ 0 & \frac{1}{L_s} \\ 0 & 0 \\ 0 & 0 \end{bmatrix} \cdot \begin{bmatrix} v_d \\ v_q \end{bmatrix} \quad (3-25)$$

It can be rewritten in the form of

$$\dot{\mathbf{x}} = \mathbf{Ax} + \mathbf{Bu} \quad (3-26)$$

$$\mathbf{y} = \mathbf{Cx} \quad (3-27)$$

where the state variables \mathbf{x} and the system outputs \mathbf{y} can be defined by

$$\mathbf{x} = \begin{bmatrix} \hat{i}_d \\ \hat{i}_q \\ \hat{e}_d \\ \hat{e}_q \end{bmatrix} \quad (3-28)$$

$$\mathbf{y} = \begin{bmatrix} \hat{i}_d \\ \hat{i}_q \end{bmatrix} \quad (3-29)$$

and matrices \mathbf{A} , \mathbf{B} and \mathbf{C} by

$$\mathbf{A} = \begin{bmatrix} -\frac{R_s}{L_s} & \hat{\omega} & \frac{1}{L_s} & 0 \\ -\hat{\omega} & -\frac{R_s}{L_s} & 0 & -\frac{1}{L_s} \\ 0 & 0 & 0 & 0 \\ 0 & 0 & 0 & 0 \end{bmatrix} \quad (3-30)$$

$$B = \begin{bmatrix} \frac{1}{L_s} & 0 \\ 0 & \frac{1}{L_s} \\ 0 & 0 \\ 0 & 0 \end{bmatrix} \quad (3-31)$$

$$C = \begin{bmatrix} 1 & 0 & 0 & 0 \\ 0 & 1 & 0 & 0 \end{bmatrix} \quad (3-32)$$

As mentioned above, the estimator for the state variable \mathbf{x} is given by

$$\dot{\hat{\mathbf{x}}} = \mathbf{A}\hat{\mathbf{x}} + \mathbf{B}\mathbf{u} + \mathbf{L}\mathbf{C}\tilde{\mathbf{x}} \quad (3-33)$$

where the feedback gain matrix \mathbf{L} is defined by

$$L = \begin{bmatrix} l_{11} & l_{12} \\ l_{21} & l_{22} \\ l_{31} & l_{32} \\ l_{41} & l_{42} \end{bmatrix} \quad (3-34)$$

Then the asymptotic state observer for the PMG and rectifier system could be derived from (3-25), as shown in Figure 3-16.

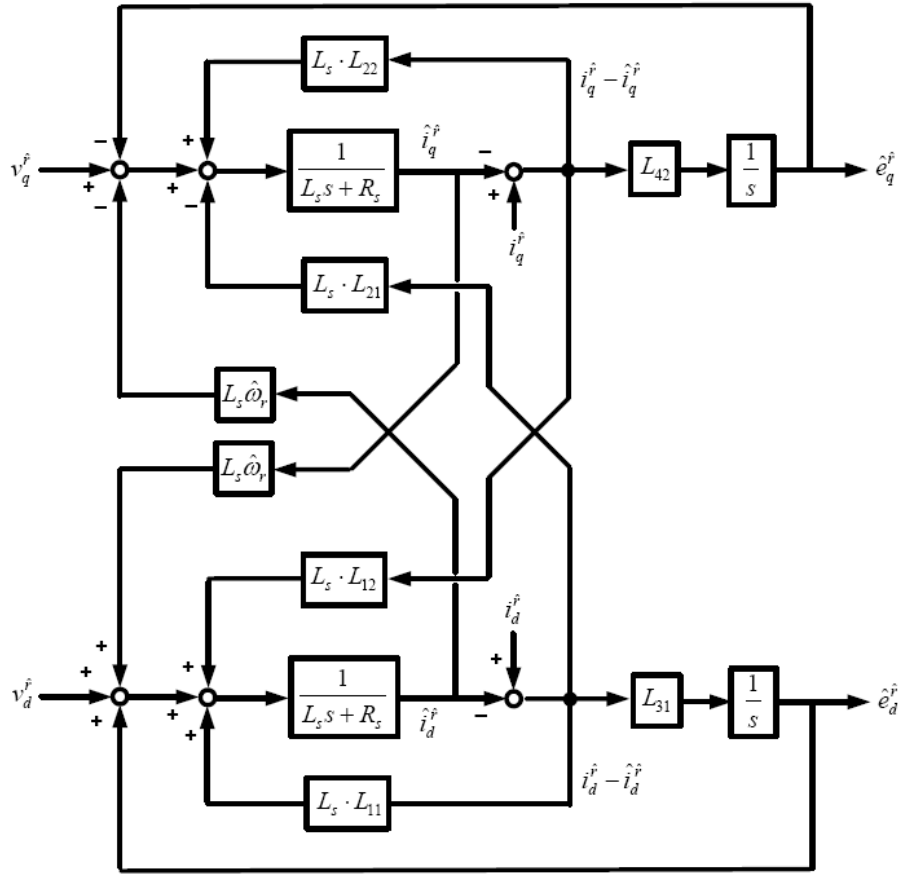


Figure 3-16 Asymptotic state observer block diagram for PMG and rectifier system

The state error dynamics of the asymptotic observer is described by

$$\dot{\tilde{\mathbf{x}}} = \dot{\mathbf{x}} - \dot{\hat{\mathbf{x}}} = (\mathbf{A} - \mathbf{LC})\tilde{\mathbf{x}} \quad (3-35)$$

where

$$\mathbf{A} - \mathbf{LC} = \begin{bmatrix} -\frac{R_s}{L_s} - l_{11} & \hat{\omega} - l_{12} & \frac{1}{L_s} & 0 \\ -\hat{\omega} - l_{21} & -\frac{R_s}{L_s} - l_{22} & 0 & -\frac{1}{L_s} \\ -l_{31} & -l_{32} & 0 & 0 \\ -l_{41} & -l_{42} & 0 & 0 \end{bmatrix} \quad (3-36)$$

The matrix above shows it is a 4th order system. In order to degrade it to two orthogonal systems aligned with the d and q axes respectively, l_{32} and l_{41} are selected to be zero. Gains l_{11}

and l_{22} are chosen to cancel out the electrical time constant of the system, while gains l_{12} and l_{21} are chosen to cancel out the effect of the estimated speed. With a desired natural frequency ω_o and damping coefficient ξ , the matrix \mathbf{L} is then given by

$$L = \begin{bmatrix} -\frac{R_s}{L_s} + 2\xi\omega_o & \hat{\omega} \\ -\hat{\omega} & -\frac{R_s}{L_s} + 2\xi\omega_o \\ \omega_o^2 L_s & 0 \\ 0 & -\omega_o^2 L_s \end{bmatrix} \quad (3-37)$$

The desired error dynamics is given by

$$c_o(s) = (s^2 + 2\xi\omega_o s + \omega_o^2)^2 \quad (3-38)$$

C. Simulation Verification

The observer is to calculate the back EMF voltages in the given d-q frame and ensure zero steady state error. Figure 3-17 depicts the scheme for the observer test in Saber simulation. The PMG is connected directly to the resistive load. The generator terminal voltages and currents are sensed and the actual d-q frame is given to the observer. Figure 3-18 shows the back EMF components in d and q axes respectively. At steady state, the PMG back EMF voltage equal $\omega\lambda_m$ and is reflected on the q-axis in the actual d-q frame, which verifies the design of the observer.

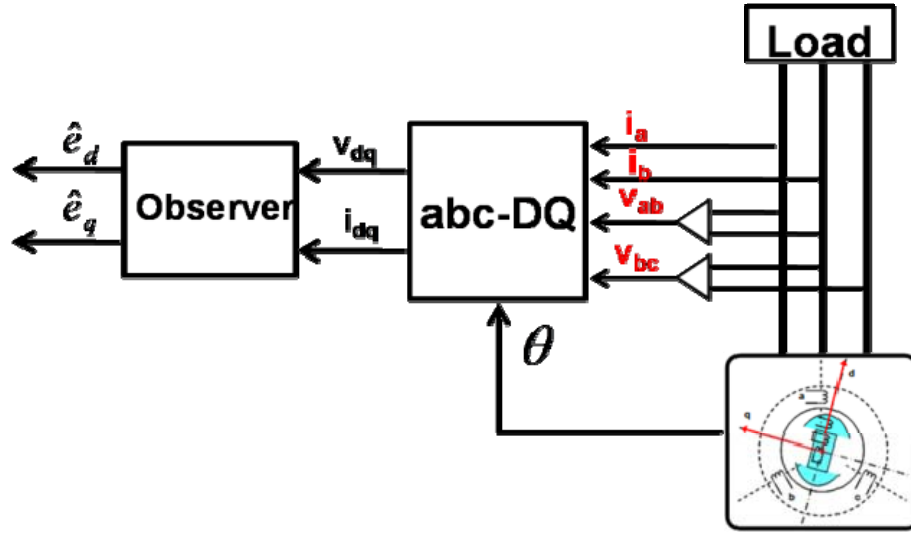


Figure 3-17 Simulation scheme for back EMF test

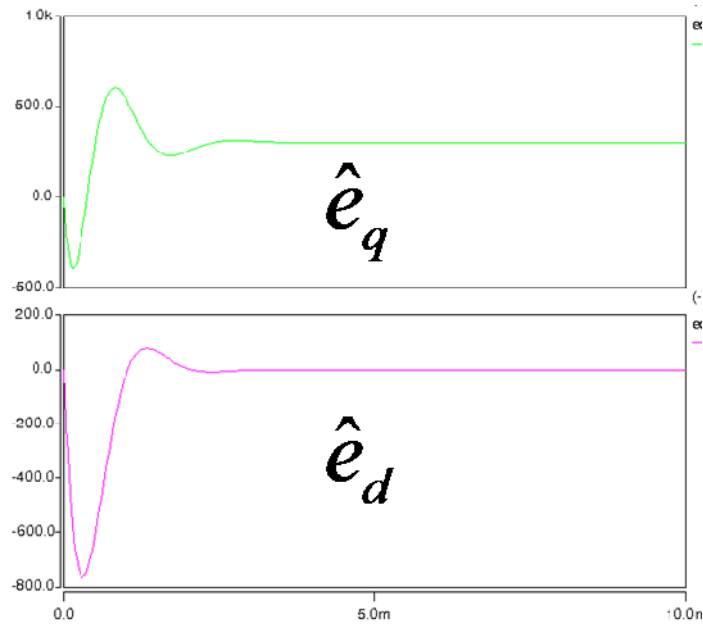


Figure 3-18 Back EMF components in d-q axes calculated by the observer

3.5.3 Tracking Controller Design

A. PLL-based tracking controller design

The PLL tracking controller synchronizes the estimated d-q frame with the actual d-q frame by regulating the d-axis back EMF component to zero. Figure 3-19 shows the PLL-based tracking controller block diagram, where \hat{e}_d is fed back in a closed-loop and a PI regulator is

used to provide the estimated speed $\hat{\omega}$. Then the estimated rotor position $\hat{\theta}$ is obtained through the integration of $\hat{\omega}$. In order to linearize the PLL dynamics and thus ensure a constant dynamic response through the whole operating range, state linearization is used with the gain of $-1/k_{lin}$, where

$$k_{lin} = \sqrt{\hat{e}_q^2 + \hat{e}_d^2} \quad (3-39)$$

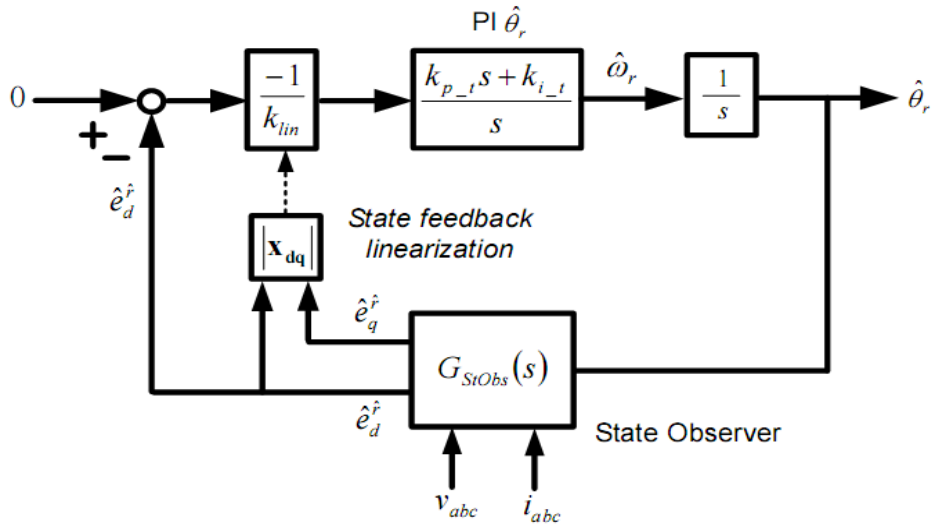


Figure 3-19 PLL-based tracking controller block diagram

The closed-loop transfer function of the PLL-based tracking controller is then given by

$$\frac{\hat{e}_d(s)}{\hat{e}_{d_ref}(s)} = \frac{k_{pt}s + k_{it}}{s^2 + k_{pt}s + k_{it}} \quad (3-40)$$

The gains are given by

$$k_{pt} = 2\xi\omega_t \quad (3-41)$$

$$k_{it} = \omega_t^2 \quad (3-42)$$

where ω_t is the desired rotor position tracking controller bandwidth and ξ is the damping coefficient.

B. Simulation Verification

The PLL tracking controller synchronizes the estimated d-q frame with the actual d-q frame. Figure 3-20 depicts the scheme for the PLL-based tracking controller test in Saber simulation. The PMG is connected directly to the resistive load. The actual angle of PMG is given. The back EMF in d-q axes are calculated with the difference between the actual angle and the estimated angle from PLL output, and then are used as the input of the PLL tracking controller. Figure 3-21 shows the estimated angle from the tracking controller and the actual angle. At steady state, the estimated angle equals the actual one, which verifies the design of the tracking controller.

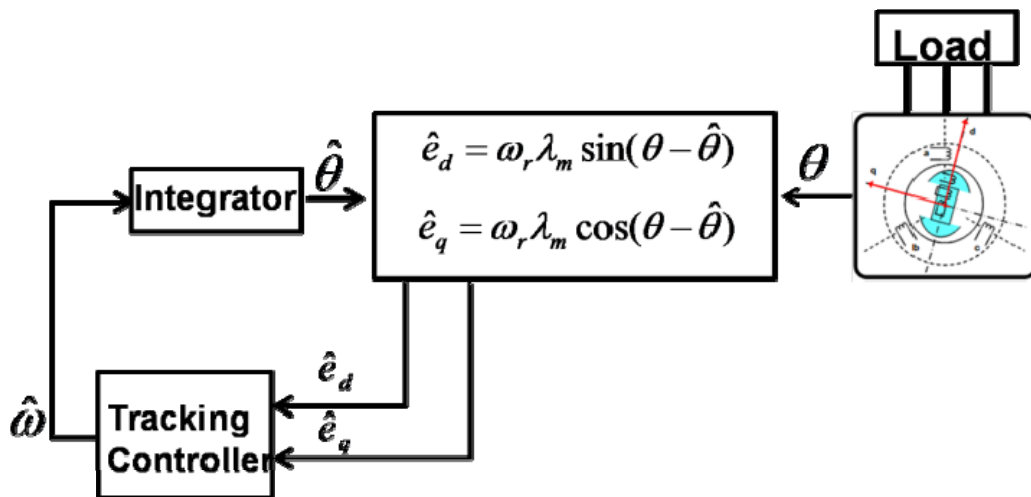


Figure 3-20 Simulation scheme for PLL-base tracking controller test

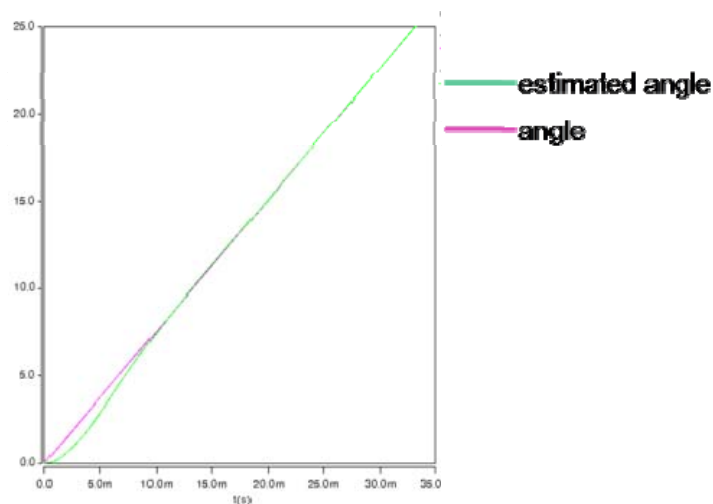


Figure 3-21 Comparison between the estimated angle and the actual angle

3.5.4 Simulation Verification

Figure 3-22 depicts the scheme of the observer and tracking controller testing for the sensorless vector control in Saber simulation. The PMG is connected directly to the resistive load. The observer is to calculate the back EMF voltages with the voltages and currents sensed from the PMG terminal side. The PLL tracking controller synchronizes the estimated d-q frame with the actual d-q frame by regulating the d-axis back EMF component to zero. Figure 3-23 shows that the estimated angle from the tracking controller tracks the actual angle well in the Saber simulation.

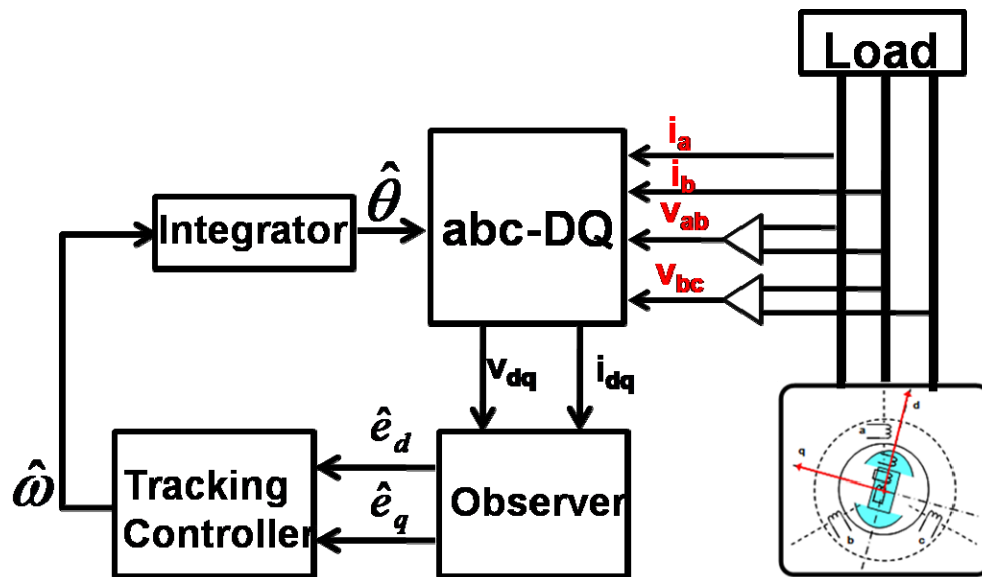


Figure 3-22 Simulation scheme for observer and tracking controller testing

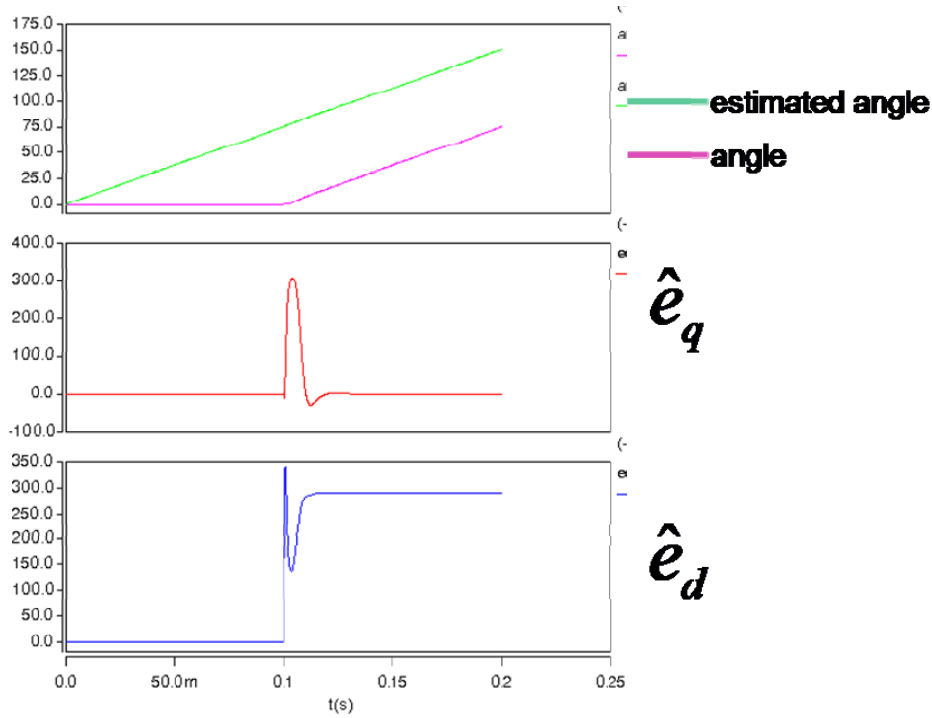


Figure 3-23 Estimated rotor position and back EMF

3.6 Control System Specifications

The design of the proposed sensorless vector control strategy for the PMG and rectifier system has two key elements, the vector control and the speed and rotor position estimation. In the vector control design, the inner current loop should be much faster than the outer voltage loop so that the inner loops and the outer loop can be decoupled to simplify the control design after a few approximations are made. Through empirical testing and taking into consideration the dynamic requirement, the relationship between the bandwidth of inner current loop ω_i and outer voltage ω_v is chosen to be

$$\omega_i = 10 \cdot \omega_v \quad (3-43)$$

In the rotor position estimation design, the observer estimates and generates the d-q axes back EMF as output. The machine back EMF is in turn used as the input for the tracking controller which generates the estimated rotor speed and rotor position as output. The dynamic response of

the observer should be much faster than that of the tracking controller. A ratio of 10 times between the observer and tracking controller shows excellent performance, as given by

$$\omega_{ob} = 10 \cdot \omega_{tr} \quad (3-44)$$

The vector control design is the function of the estimator employed. Thus the observer represents the fastest dynamic in the proposed sensorless vector control strategy, which is much faster than the current loops. A ratio of 6 times between the observer and current loop bandwidth is good enough for the control design. Table 3-1 shows the control system specification.

Table 3-1 Control system specifications

Parameter	Symbol	Value
D axis current loop bandwidth	f_{id}	500Hz
Q axis current loop bandwidth	f_{iq}	500Hz
Voltage loop bandwidth	f_v	50Hz
Observer bandwidth	f_{ob}	3000Hz
Tracking controller bandwidth	f_{tr}	300Hz
Damping coefficient	ζ	0.707

3.7 Simulation Verification in Saber for PMG and Rectifier System

The average model of PMG and rectifier system is built in Saber to verify the proposed control method. With the closed-loop control, the steady state waveforms of the PMG and active front-end rectifier system at full speed are shown in Figure 3-24. The traces from top to bottom are: rotor angle, ac phase voltage v_a , ac phase current i_a and dc bus voltage V_{dc} . At full speed, the line frequency is 60Hz. The modulation index is 87.35%. The dc bus voltage is controlled

effectively at 300V. The ac current is in phase with generator terminal voltage in the unity power factor control.

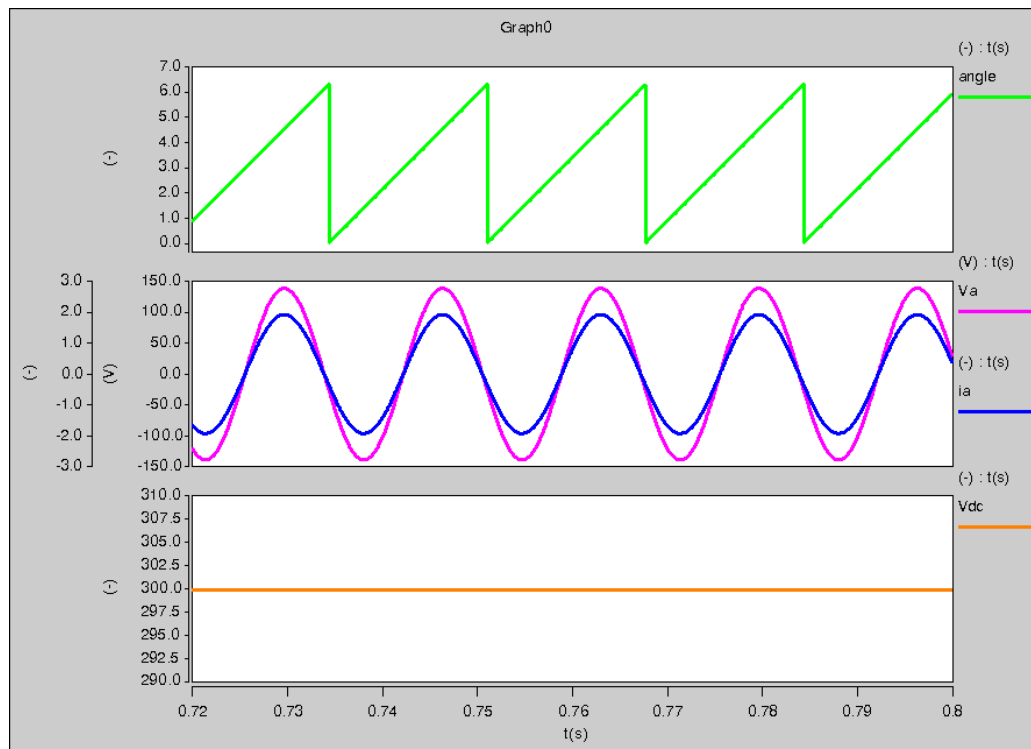


Figure 3-24 Simulation waveforms of angle, PMG terminal voltage v_{ab} , ac current i_a and dc bus voltage V_{dc} at full speed with unity power factor control in the PMG and active front-end rectifier system

With the outer reactive power loop, the boost rectifier can maintain a sinusoidal current waveform at ac side with an arbitrary value of fundamental power factor. Figure 3-25 shows the simulation waveforms when the current leads the voltage. Figure 3-26 shows the simulation waveforms when the current lags the voltage. The traces from top to bottom are: rotor angle, ac phase voltage v_a , ac phase current i_a and dc bus voltage V_{dc} . The dc bus voltage is controlled effectively at 300V.

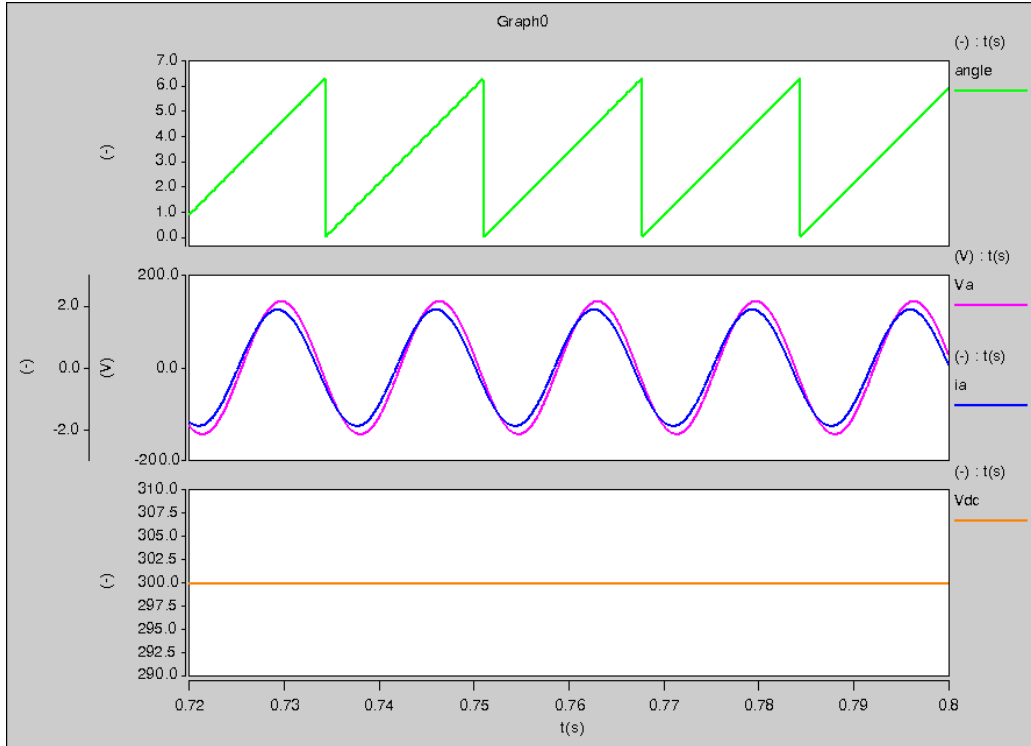


Figure 3-25 Simulation waveforms of angle, PMG terminal voltage v_a , ac current i_a and dc bus voltage V_{dc} when the current leads the voltage

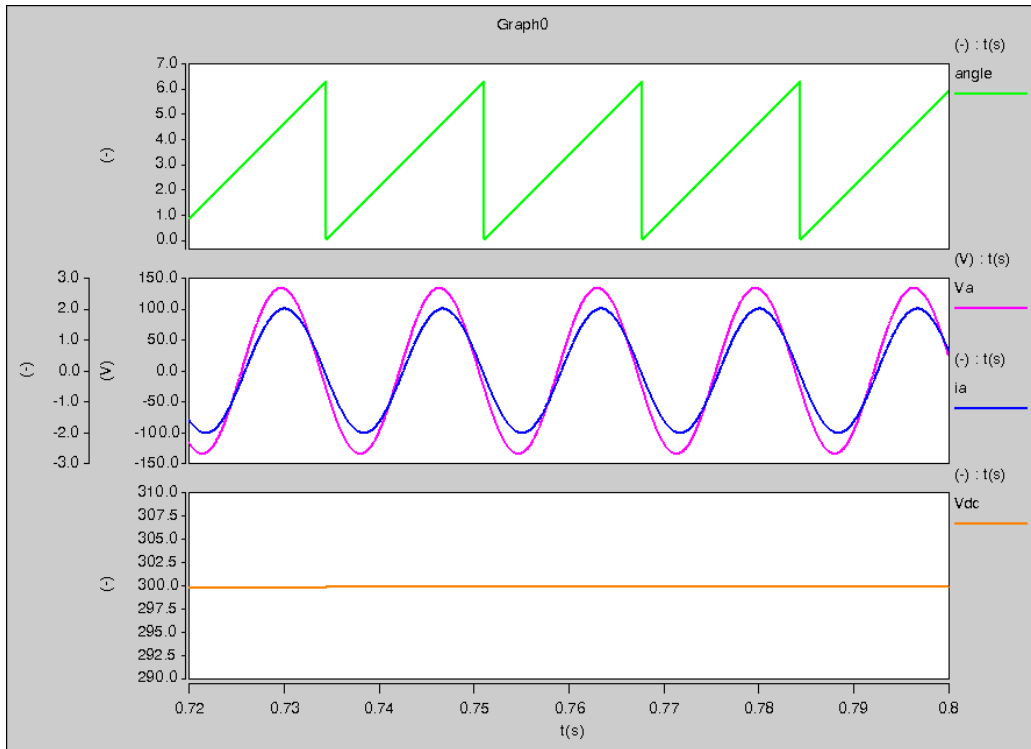


Figure 3-26 Simulation waveforms of angle, PMG terminal voltage v_{ab} , ac current i_a and dc bus voltage V_{dc} when the current lags the voltage

The voltage control is tested under two conditions, namely load step and generator speed change. Figure 3-27 shows the simulation waveforms of the PMG and active front-end rectifier system at 2/3 of the full speed. The line frequency is 40Hz. The modulation index is 65.04%. The dc bus voltage is controlled effectively at 300V. Figure 3-28 and Figure 3-29 show the waveforms of the PMG and active front-end rectifier system after applying a load step from 200W to 400W at 0.5s. After the load step, the ac input current increases to match the load power demand. The q axis current i_q tracks its reference i_{qref} well. There is a small dc voltage dip at the time of the load step. After that the dc output voltage is at controlled effectively at 300V.

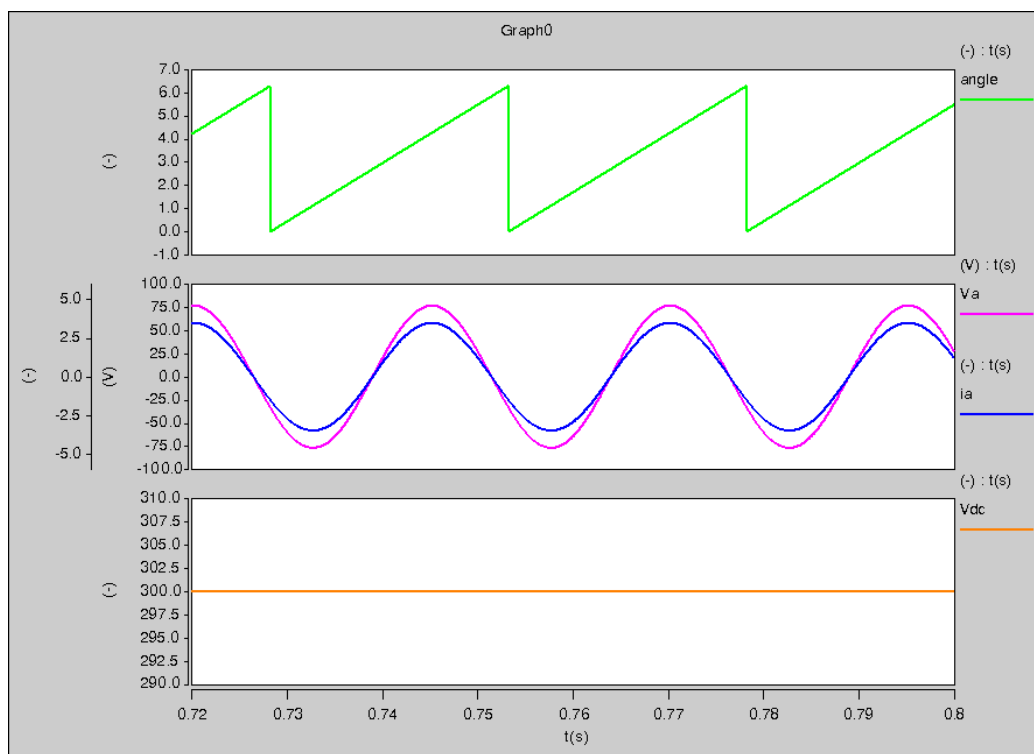


Figure 3-27 Simulation waveforms of angle, PMG terminal voltage v_{ab} , dc bus voltage V_{dc} and ac current i_a at 2/3 of the full speed in the PMG and active front-end rectifier system

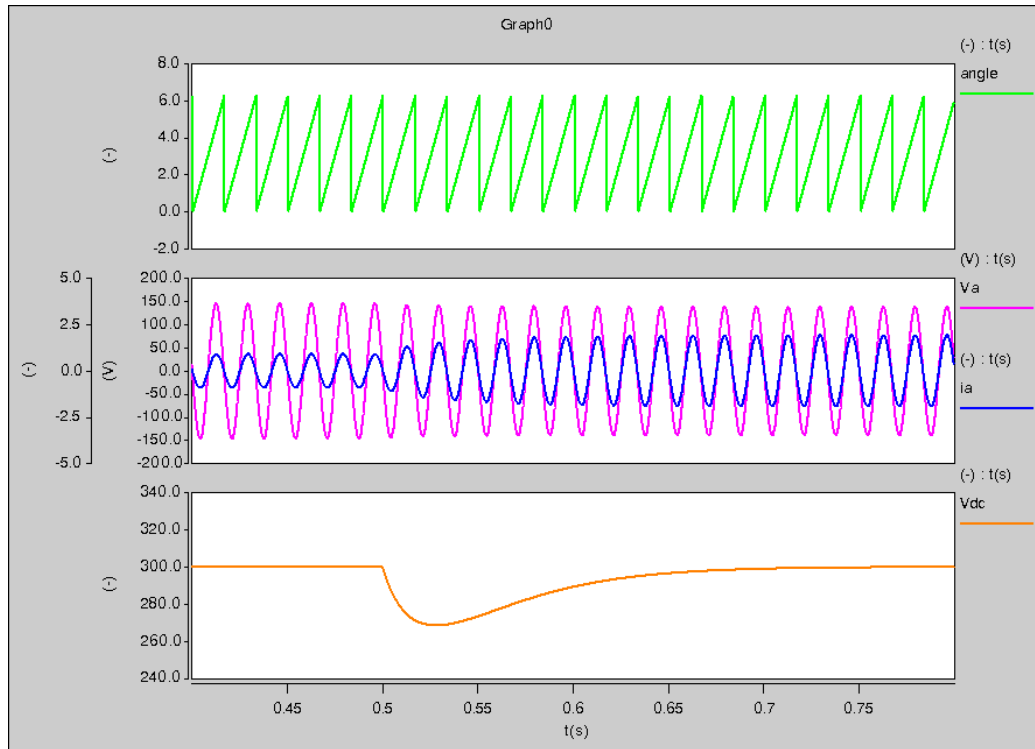


Figure 3-28 Simulation waveforms of angle, PMG terminal voltage v_{ab} , dc bus voltage V_{dc} and ac current i_a at the load step in the PMG and active front-end rectifier system

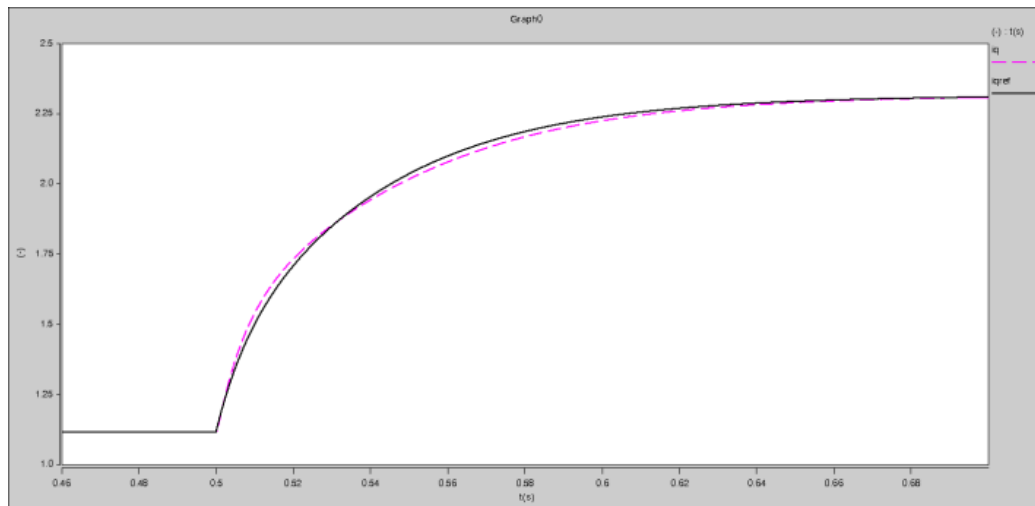


Figure 3-29 Simulation waveforms of q axis current i_q and q axis reference current i_{qref} at the load step in the PMG and active front-end rectifier system

Chapter 4 Hardware Development and Experiments

The chapter presents the hardware development for the permanent magnet generator and rectifier system. First hardware including PMG, IPM and drive board, signal conditioning board are explained in detail. After that, the experimental results with the proposed control scheme are presented. Both the voltage control and reactive power control of the PMG and rectifier system are verified through experiment.

4.1 *System Configuration*

A 400W prototype of PMG and rectifier system is built to verify the control strategy. The rectifier system is composed of two parts: the power stage, including active front-end rectifier and DC link, and the control circuit, including driver board, signal conditioning board and digital controller (universal controller). An SPM generator is used for experiment, due to the limitations in the laboratory. Figure 4-1 shows the permanent magnet generator, which provides the three phase ac power. Figure 4-2 shows the power stage and control circuit. The basic system information and parameters are summarized in Table 4-1.

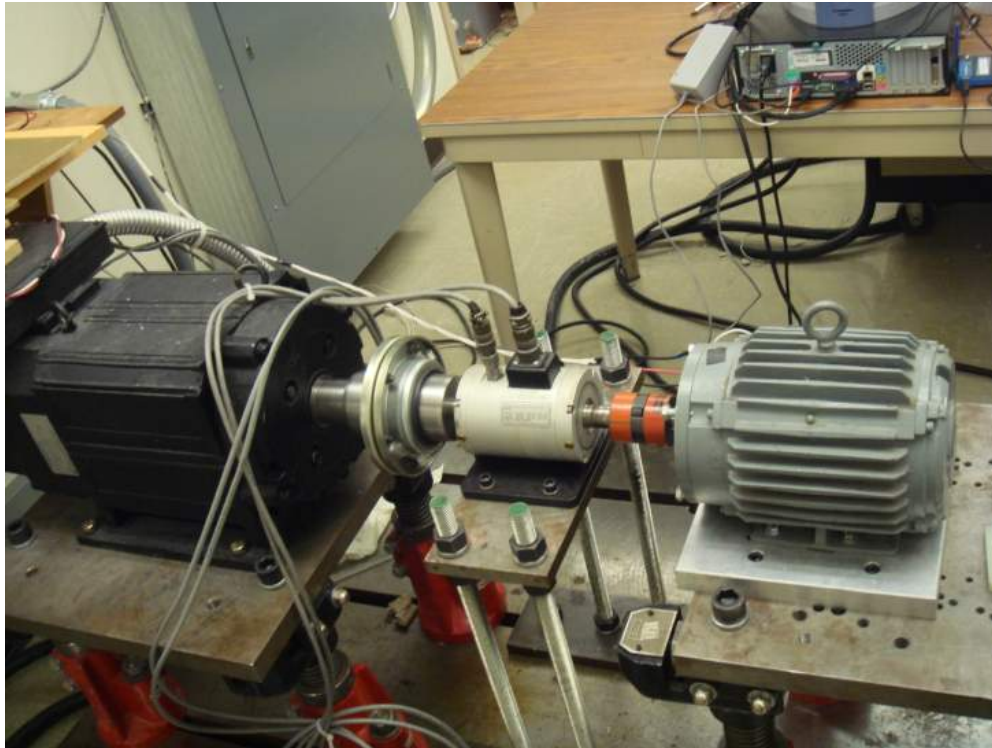


Figure 4-1 Permanent magnet generator

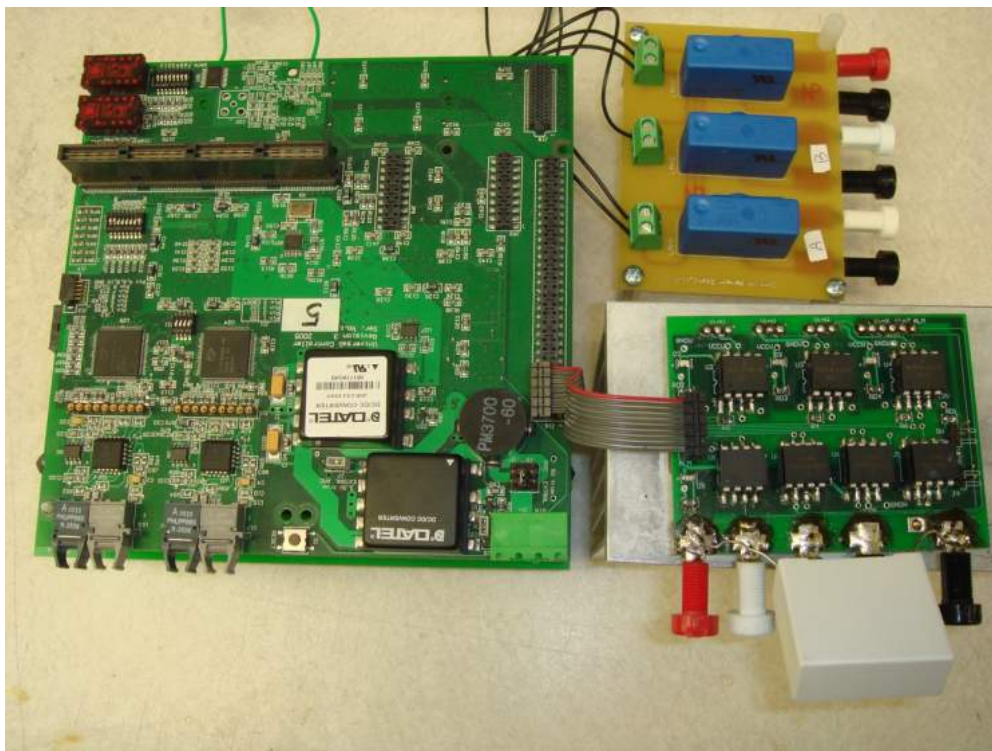


Figure 4-2 Power stage and control unit

Table 4-1 Parameters of the PMG and rectifier system

Parameter	Symbol	Value
Permanent magnet generator:		
Stator resistance	R_s	3.4 Ω
Stator inductance	L_s	27.5mH
Back EMF constant	λ_m	0.4022Wb
Nominal power	P_n	400W
Nominal voltage	V_n	107V
Nominal frequency	f	60Hz
Boost rectifier:		
Reference DC link voltage	V_{dcref}	300V
Modulation index	M	0.875
Switching frequency	f_s	20k
DC link capacitor	C	500 μ F
Controller:		
D axis current loop bandwidth	f_{id}	500Hz
Q axis current loop bandwidth	f_{iq}	500Hz
Voltage loop bandwidth	f_v	50Hz
Observer bandwidth	f_{ob}	3000Hz
Tracking controller bandwidth	f_{tr}	300Hz
Damping coefficient	ζ	0.707

4.2 Hardware Design

4.2.1 Signal Conditioning Board

The signal conditioning board performs two main functions, including sensing the analog signals and converting the analog signals to digital data.

A. Voltage Sensing Circuit

The voltage sensing circuit sense two input AC voltages and DC link voltage. LV 20-P from LEM Inc., a closed loop voltage transducer using the Hall effect, is used to measure the dc and ac voltages. Figure 4-3 depicts the voltage sensing circuit diagram. The external resistor R1 is connected in series with the primary circuit to transform the voltage signal to a certain scaled current signal. Then the sensor transforms the current signal from primary side to secondary side by a ratio of 1000:2500. The resistor R2 transforms the secondary side current flowing out from the sensor to voltage signal for the AD input. For the R1 selection, the maximum measured voltage and the nominal primary RMS current are considered. The primary nominal RMS current is 10mA and DC link voltage, the largest measured voltage, is 300V. Considering the voltage spike, the resistor R1 is given by

$$R1 = \frac{350V}{10mA} = 35k\Omega \quad (4-1)$$

Since the primary voltage is high, the resistor R1 needs to have certain power dissipation capability, which is given by

$$P = \frac{(350V)^2}{35k\Omega} = 3.5W \quad (4-2)$$

For the R2 selection, secondary nominal current RMS is 25mA and the AD input is $\pm 10V$. Then the resistor R2 is given by

$$R2 = \frac{8.75V}{25mA} = 350\Omega \quad (4-3)$$

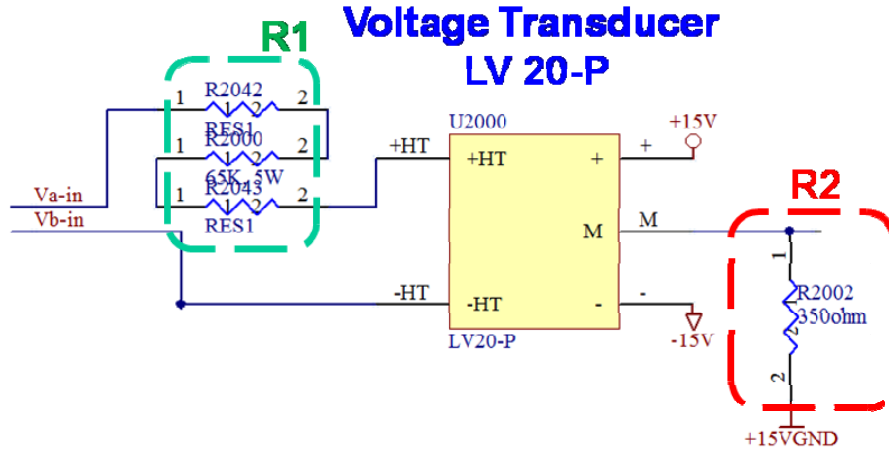


Figure 4-3 Voltage sensing circuit

B. Current Sensing Circuit

The current sensing circuits sense the three phase input AC currents. LAH 25-NP from LEM Inc., a closed loop multi-range current transducer using the Hall effect, is used to measure the dc and ac currents. The sensor transforms the current signal from primary side to secondary wide by a ratio of 1000:1-2-3. The ratio of 1000:3 is selected. For the ratio the primary nominal current is 8A, which is enough for this experiment. Then a resistor transforms the secondary side current flowing out from the sensor to voltage signal for the AD input. For the resistance selection, secondary nominal current RMS is 25mA and the AD input is $\pm 10V$. With certain margin for protection, the resistor R is given by

$$R = \frac{8.75V}{25mA} = 350\Omega \quad (4-4)$$

C. Low Pass Filter

The low pass filter is needed to reduce the high frequency harmonics before the signal is sent to AD chips. Figure 4-4 depicts a 2nd order Butterworth low pass filter. TL074 are chosen as the operational amplifier. The cut-off frequency and the dc gain are determined by the resistance and capacitance values. The transfer function of the 2nd order Butterworth low pass filter is given by

$$\frac{V_o}{V_i} = \frac{1}{R_2 R_3 C_2 C_3 s^2 + (R_2 + R_3) C_2 s + 1} \quad (4-5)$$

For simple calculation, we select $R_1=R_2$, $C_1=2C_2$. The corner frequency is the given by

$$f_{corner} = \frac{1.414}{2\pi R_1 C_1} \quad (4-6)$$

For the system, the line frequency is 60Hz and the switching frequency is 20kHz, so the corner frequency of 5kHz is appropriate to reduce the switching ripple and has limited effect on fundamental components. To realize that, $R_1=7.15k\Omega$ and $C=6nF$.

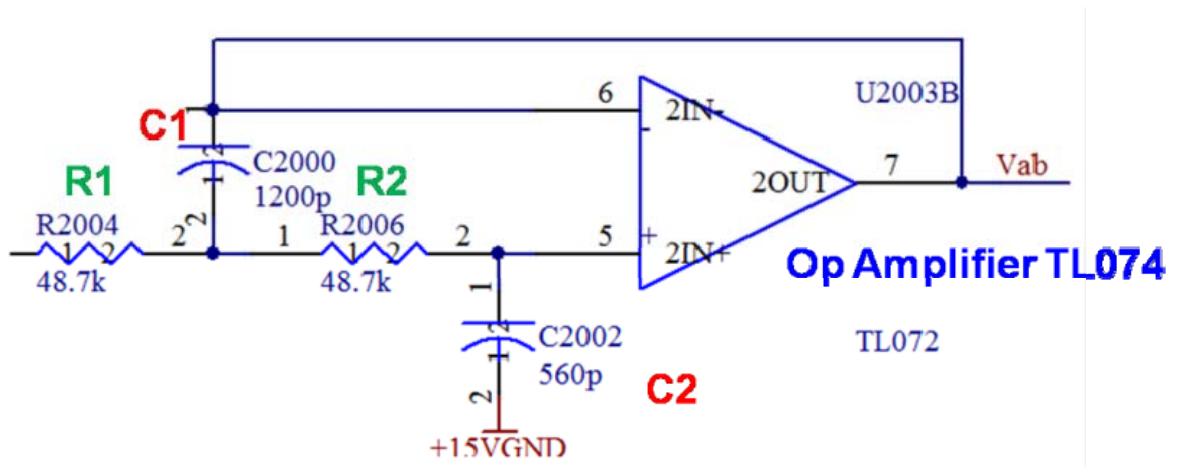


Figure 4-4 2nd order Butterworth low pass filter

D. A/D converter

A/D converter convert analog signal to digital format for the digital signal processing. In the case, six channels of ADC are required, which are one DC voltage, two AC voltages and three AC currents. AD 7864 is chosen, as shown in Figure 4-5, which is a high speed, low power, 4-channel, simultaneous sampling 12-bit analog-to-digital converter.

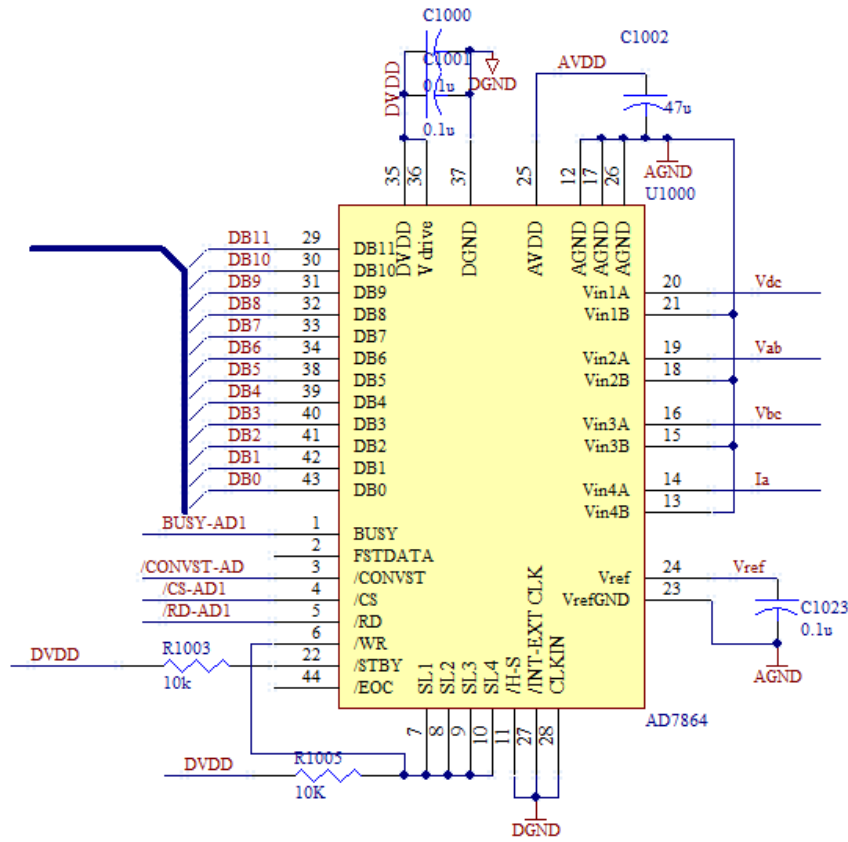


Figure 4-5 A/D converter circuit

4.2.2 IPM and the Driver Board

A. IPM

For the power stage of the converter, we select the IGBT-IPM 6MBP30RH060, a module consisting of six 600V/30A IGBTs in one package. The block diagram is shown in Figure 4-6. The pre-drivers have the function including amplifier for drive, power supply under-voltage protection and IGBT chip overheating protection. For the control circuit, the recommended operating power supply voltage of pre-drive is 15V. The input threshold turn on voltage is 1.35V and turn off voltage is 1.6V. Input zener voltage is 8V.

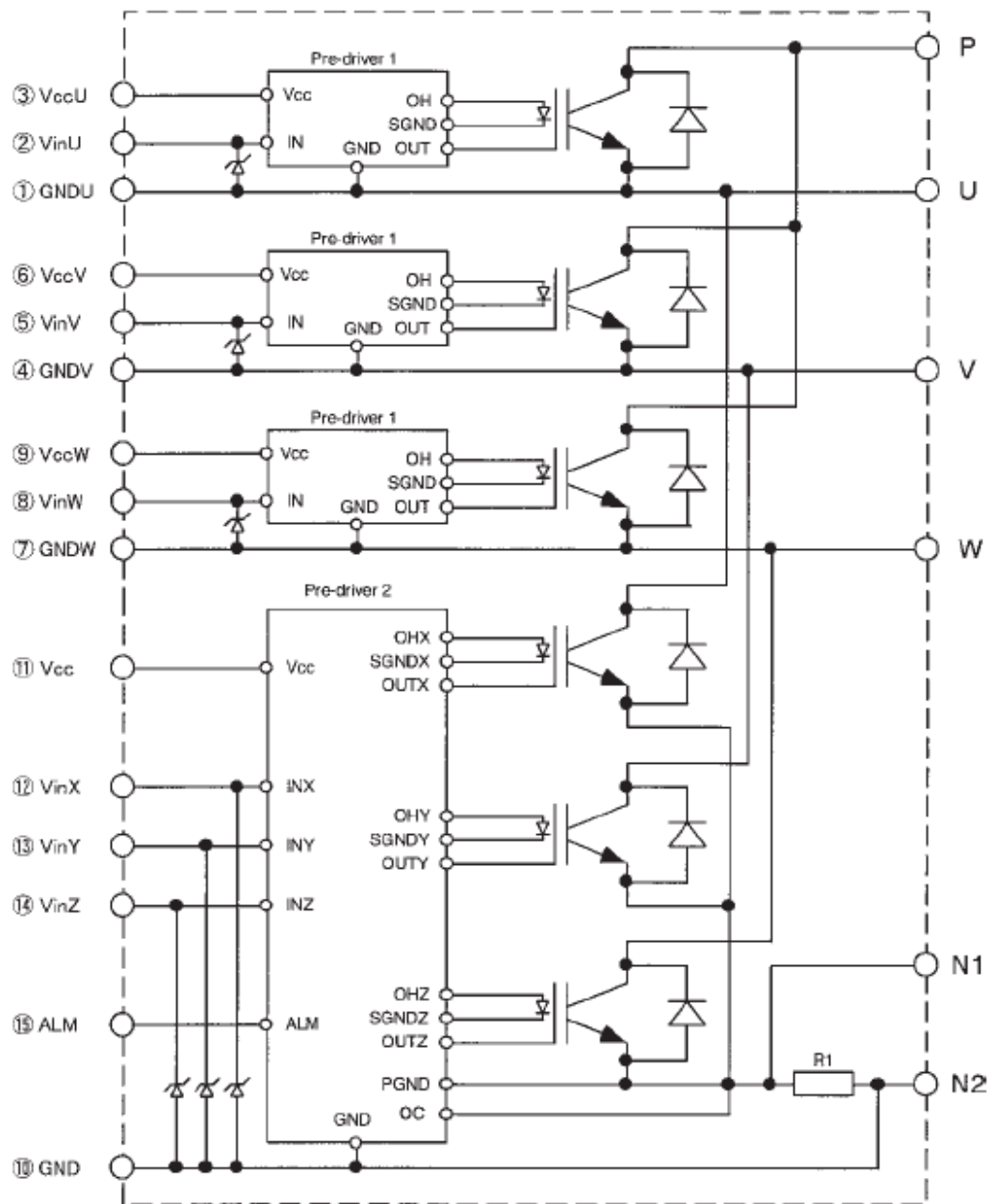


Figure 4-6 IPM block diagram

B. Driver Board

For the IPM proper operation, optocouplers are used for isolation. HCPL-4504 from Agilent Technologies is selected, the functional diagram of which is shown in Figure 4-7. Table 4-2 depicts the truth table of HCPL-4504.

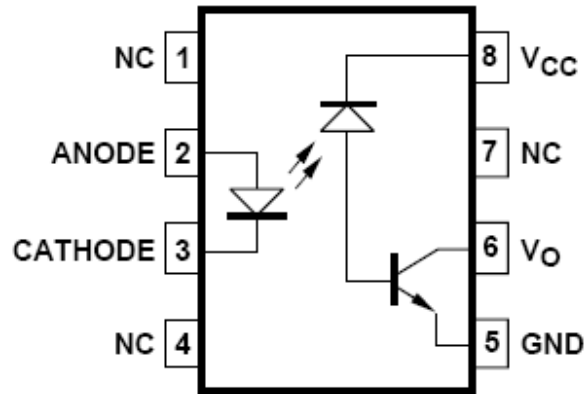


Figure 4-7 Function diagram of HCPL-4504

Table 4-2 Truth table of HCPL-4504

LED	V_o
ON	LOW
OFF	HIGH

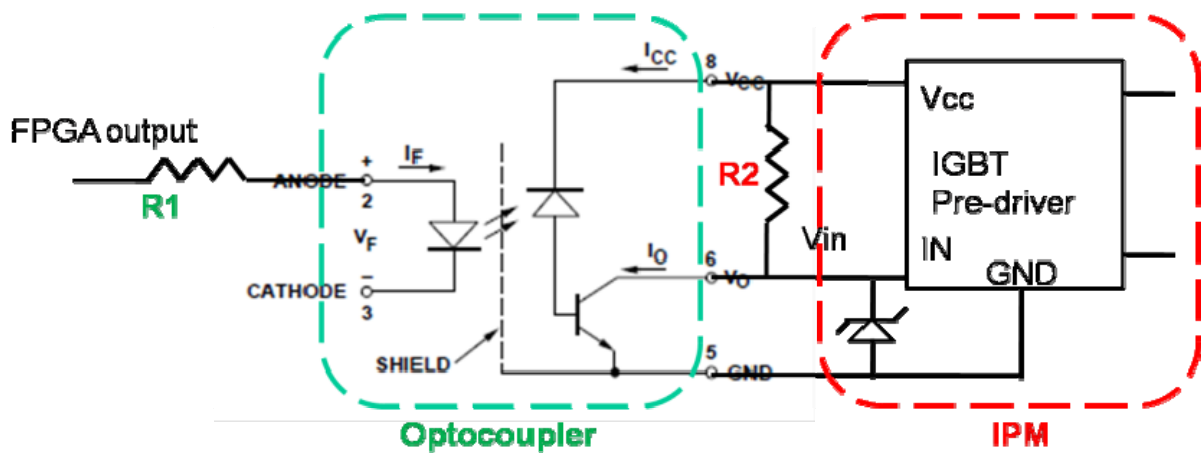


Figure 4-8 Circuit diagram of the optocouplers and the pre-driver of IPM

In Figure 4-8, R1 is selected to limit the input forward current, which is related to the FPGA output voltage, the optocoupler input forward voltage and current. The FPGA output voltage is 3.3V and the optocoupler input forward voltage is 1.5V. The typical value of the input forward current is 16mA. The value of 8mA is selected so that it doesn't exceed the FPGA output current capability. The value of R1 is then given by

$$R1 = \frac{3.3V - 1.5V}{8mA} = 225\Omega \quad (4-7)$$

R2 is selected to limit the output current through the transistor and provide the input current of pre-driver. The power supply V_{cc} is 15V. When the output voltage of the optocoupler is low, the current through the transistor should be small than 8mA, so R2 is given by

$$R2 \geq \frac{15V}{8mA} = 1.88K\Omega \quad (4-8)$$

The input zener voltage of the pre-driver is 8V. When the output voltage of the optocoupler is high, the input current of the pre-driver should be larger than 2mA, so R2 is given by

$$R2 \leq \frac{15V - 8V}{2mA} = 3.5K\Omega \quad (4-9)$$

The value of R2 is finally selected to be 3k Ω based on the discussions above.

Figure 4-9 shows the schematic of the driver board. Figure 4-10 shows the physical structure of the IPM, the driver board and the heat sink.

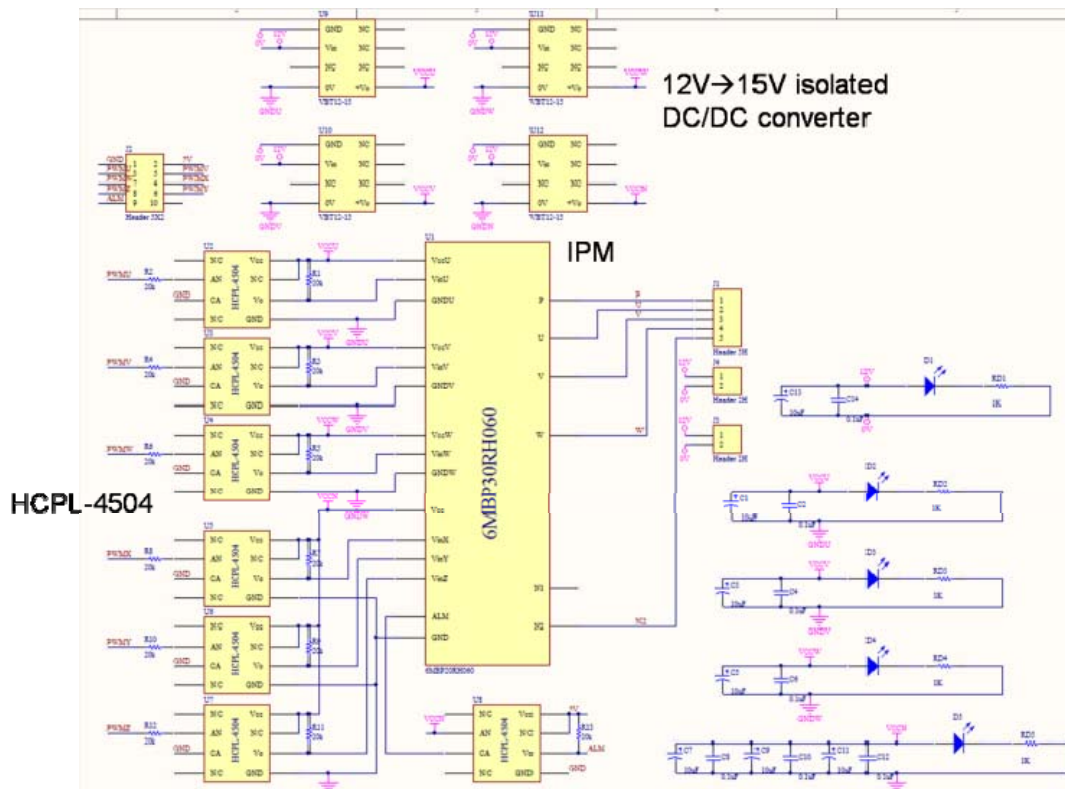


Figure 4-9 Schematic of the driver board

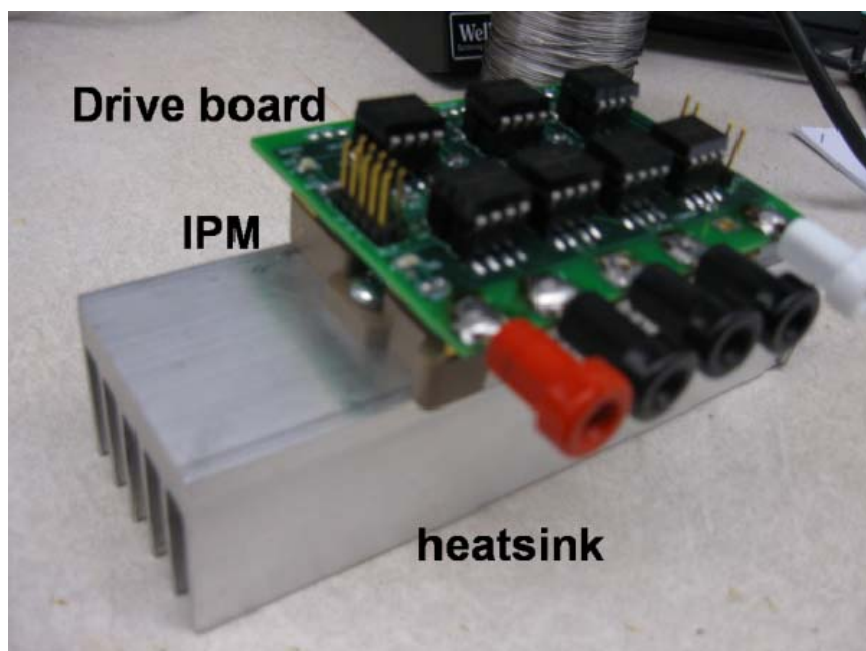


Figure 4-10 Physical structure of the IPM, the driver board and the heat sink

4.2.3 PMG Parameters Measurement

As shown in Figure 4-11, the terminal inductance value changes according to the rotor position in IPM motor. It can be given by

$$L_{terminal} = 1.5 \left[\left(\frac{L_d + L_q}{2} + \frac{L_d - L_q}{2} \cos 2\theta \right) \right] \quad (4-10)$$

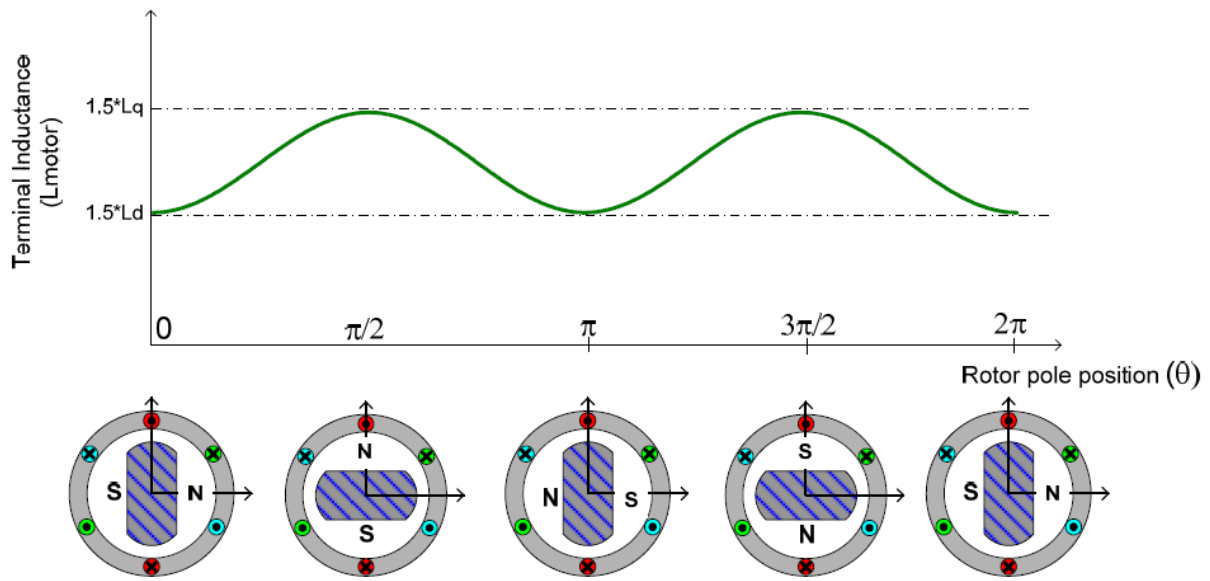


Figure 4-11 IPM motor terminal inductance variation according to the rotor position [7]

Figure 4-12 and Figure 4-13 show a measurement method of the terminal inductances in d and q axes for a PMG respectively.

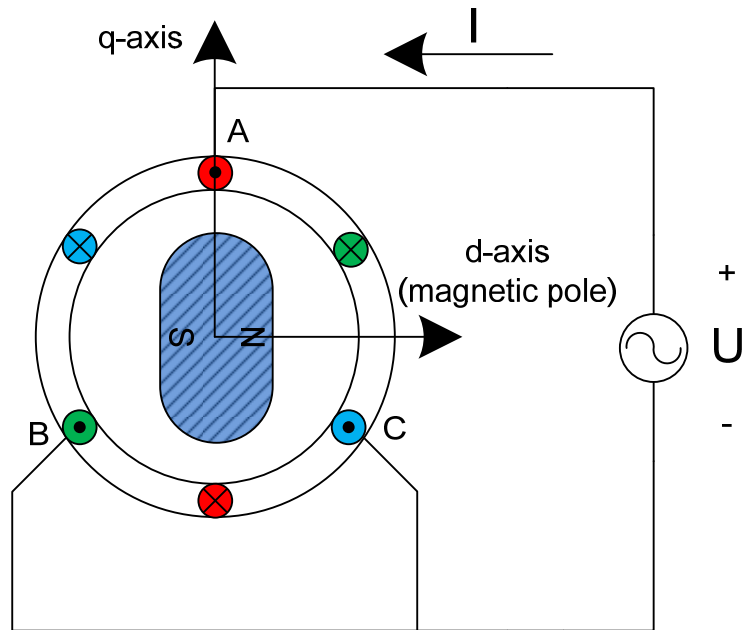


Figure 4-12 Motor terminal d-axis inductance L_d measurement

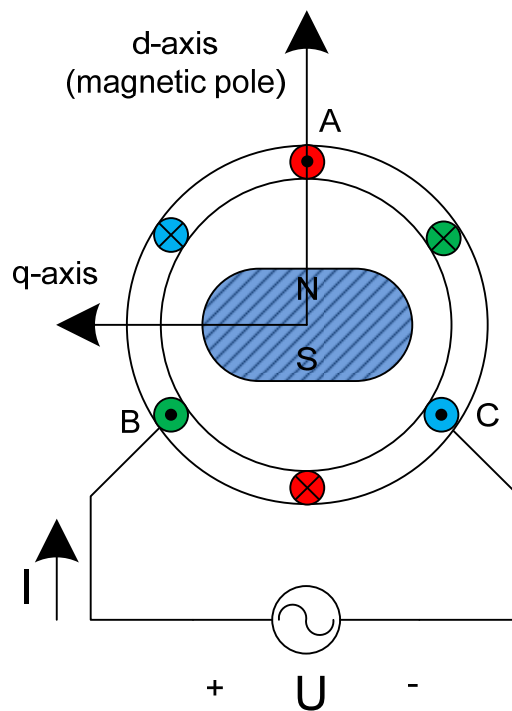


Figure 4-13 Motor terminal q-axis inductance L_q measurement

Stator resistance can be measured with multi-meter.

The measured results are shown in and used for control design.

4.3 Experimental Verification

4.3.1 PMG and diode rectifier system experiment

PMG is connected with the diode bridge without control. Figure 4-14 shows the steady state waveforms of PMG and the diode rectifier system. The traces from top to bottom are: rotor angle, ac line to line voltage v_{ab} , dc bus voltage V_{dc} and ac phase current i_a .

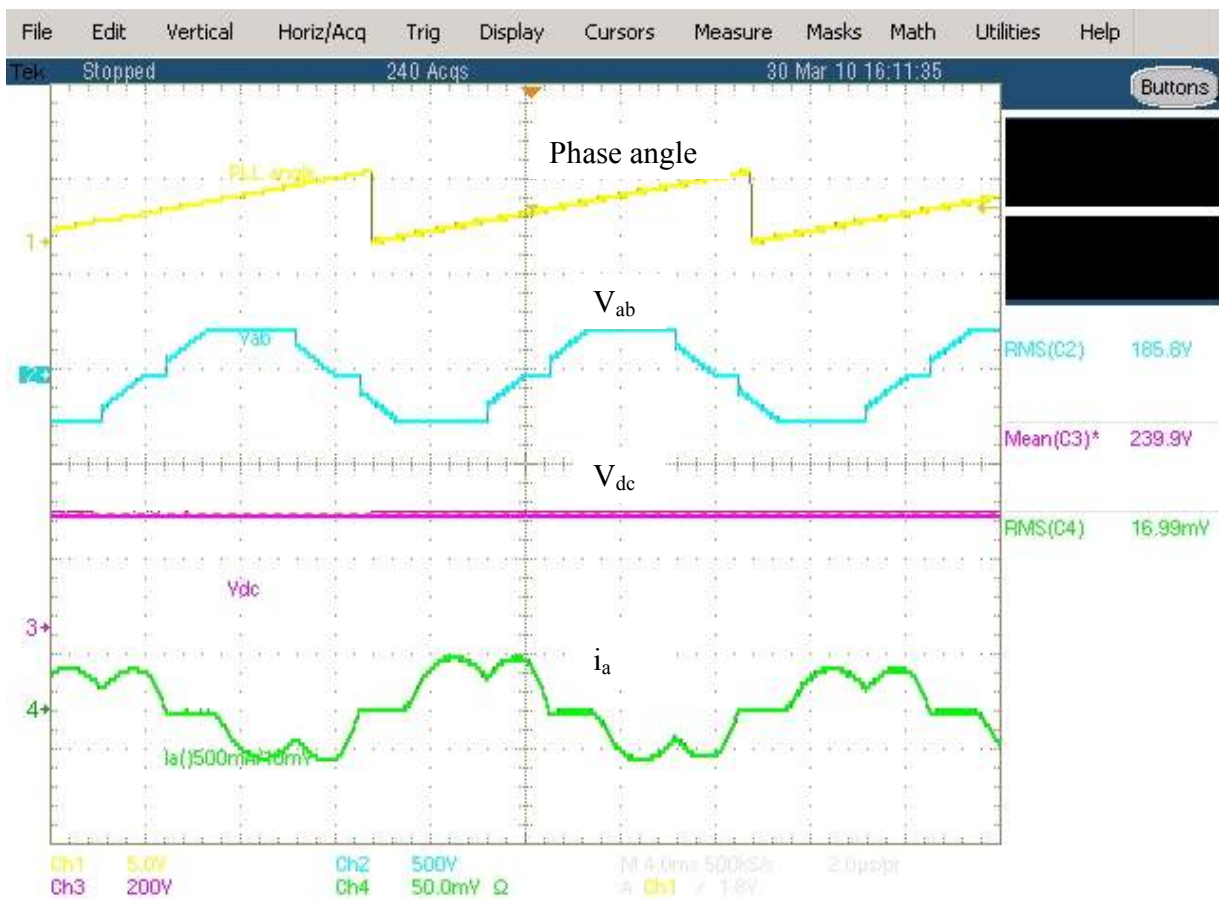


Figure 4-14 Steady state waveforms of angle, PMG terminal voltage v_{ab} , dc bus voltage V_{dc} and ac current i_a in the PMG and diode rectifier system

The average value of the dc output voltage is 240V, a fixed value depending on the PMG terminal voltage. Figure 4-15 shows the Fourier analysis result for the ac input current. The ac current THD is 30.31%.

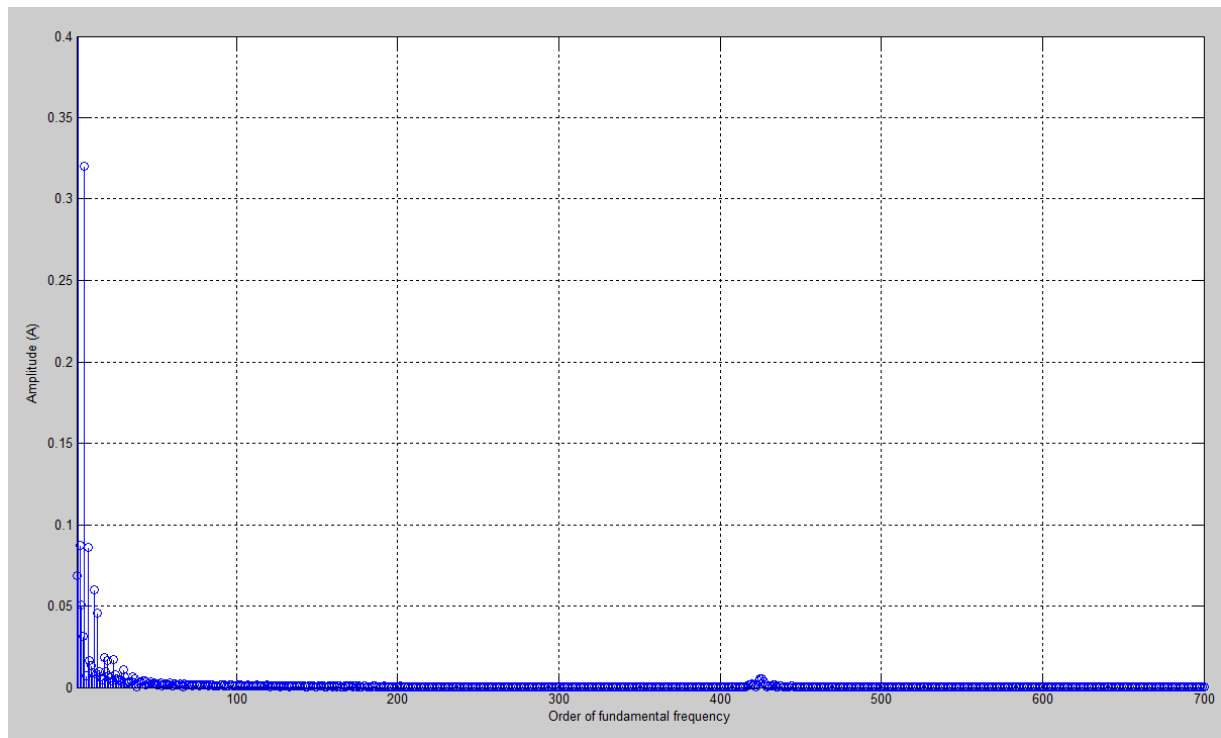


Figure 4-15 Input current spectrum waveforms of the diode rectifier

In the PMG and diode rectifier system, the dc output voltage is a fixed value depending on the ac input voltage. The THD of the ac input current is large, among which the low frequency harmonic components take a large portion.

4.3.2 PMG and active front-end rectifier system experiment

With the closed-loop control, the steady state waveforms of the PMG and active front-end rectifier system at full speed are shown in Figure 4-16. The traces from top to bottom are: rotor angle, ac line to line voltage v_{ab} , dc bus voltage V_{dc} and ac phase current i_a . At full speed, the line frequency is 60Hz. The RMS value of PMG terminal line to line voltage is 185V. The modulation index is 87.35%. The dc bus voltage is controlled effectively at 296.5V. Figure 4-17

shows the Fourier analysis result for the ac input current. The ac current THD is 4.39%, among which the ac current THD due to high frequency harmonics is 3.26%.

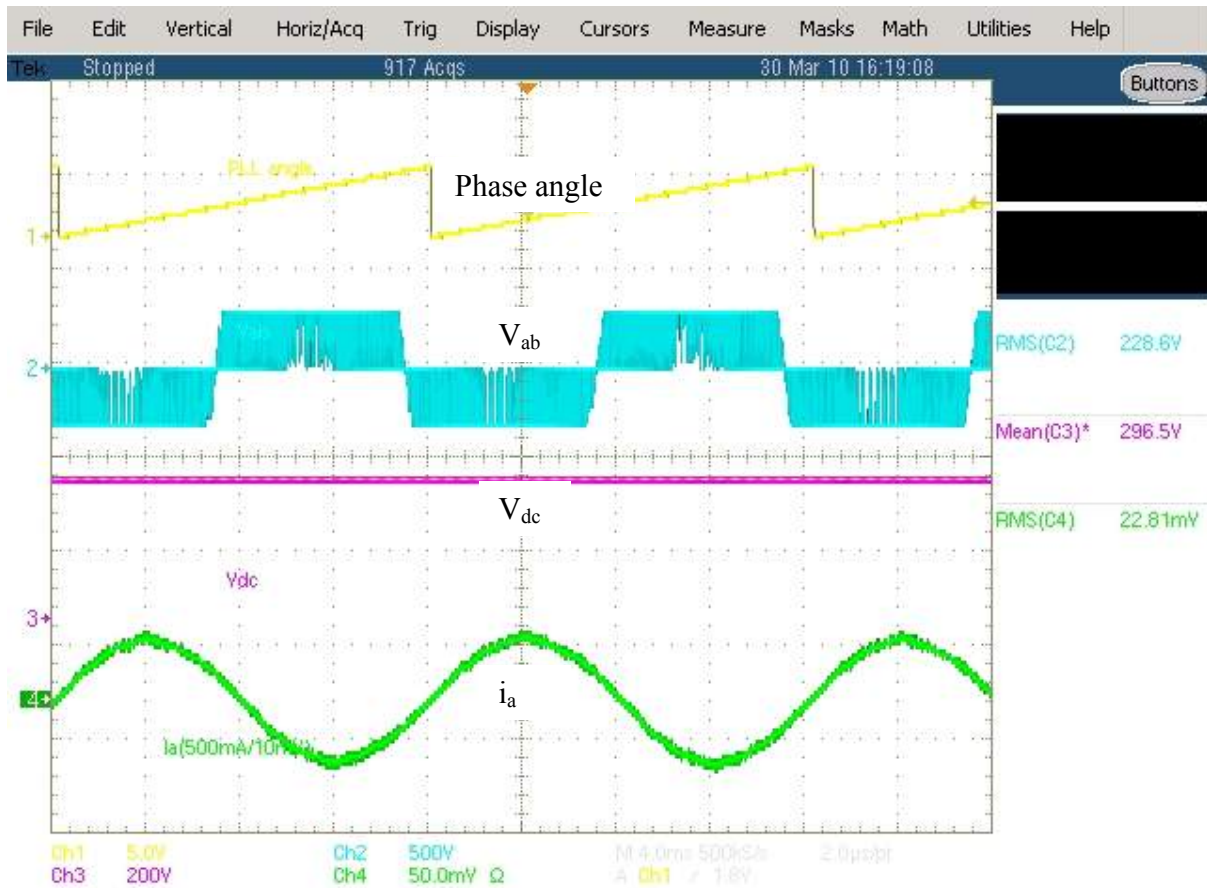


Figure 4-16 Steady state waveforms of angle, PMG terminal voltage v_{ab} , dc bus voltage V_{dc} and ac current i_a at full speed in the PMG and active front-end rectifier system

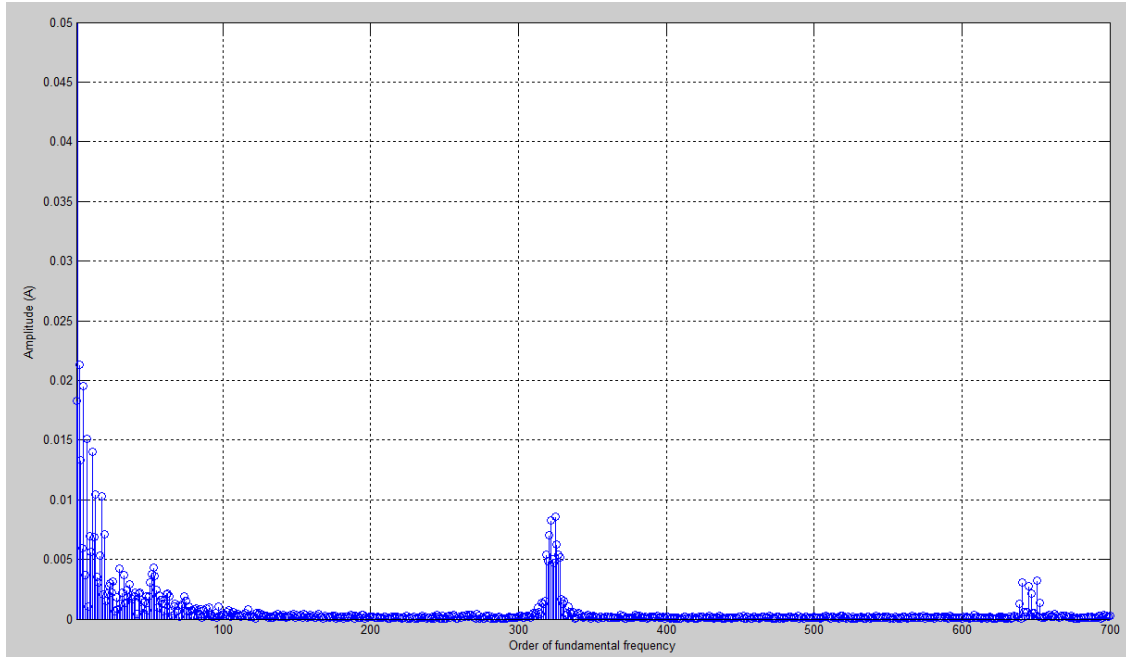


Figure 4-17 Input current spectrum waveforms at full speed of the active front-end rectifier

With the closed-loop control, the steady state waveforms of the PMG and active front-end rectifier system at half speed are shown in Figure 4-18. The traces from top to bottom are: rotor angle, ac line to line voltage v_{ab} , dc bus voltage V_{dc} and ac phase current i_a . At half speed, the line frequency is 30Hz. The RMS value of PMG terminal line to line voltage is 92V. The modulation index is 43.36%. The dc bus voltage is controlled effectively at 297.1V. Figure 4-19 shows the Fourier analysis result for the ac input current. The ac current THD is 6.46%, among which the ac current THD due to high frequency harmonics is 0.89%.

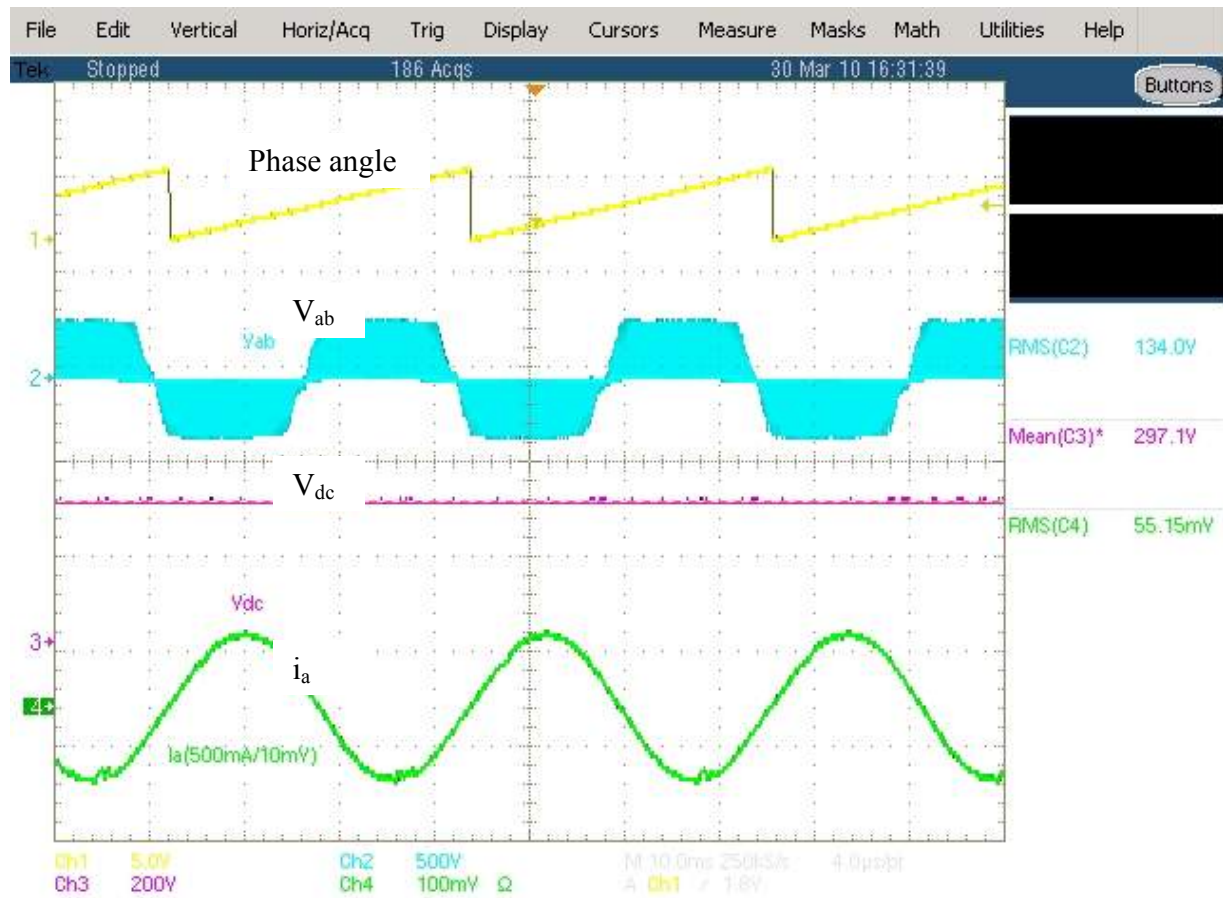


Figure 4-18 Steady state waveforms of angle, PMG terminal voltage v_{ab} , dc bus voltage V_{dc} and ac current i_a at half speed in the PMG and active front-end rectifier system

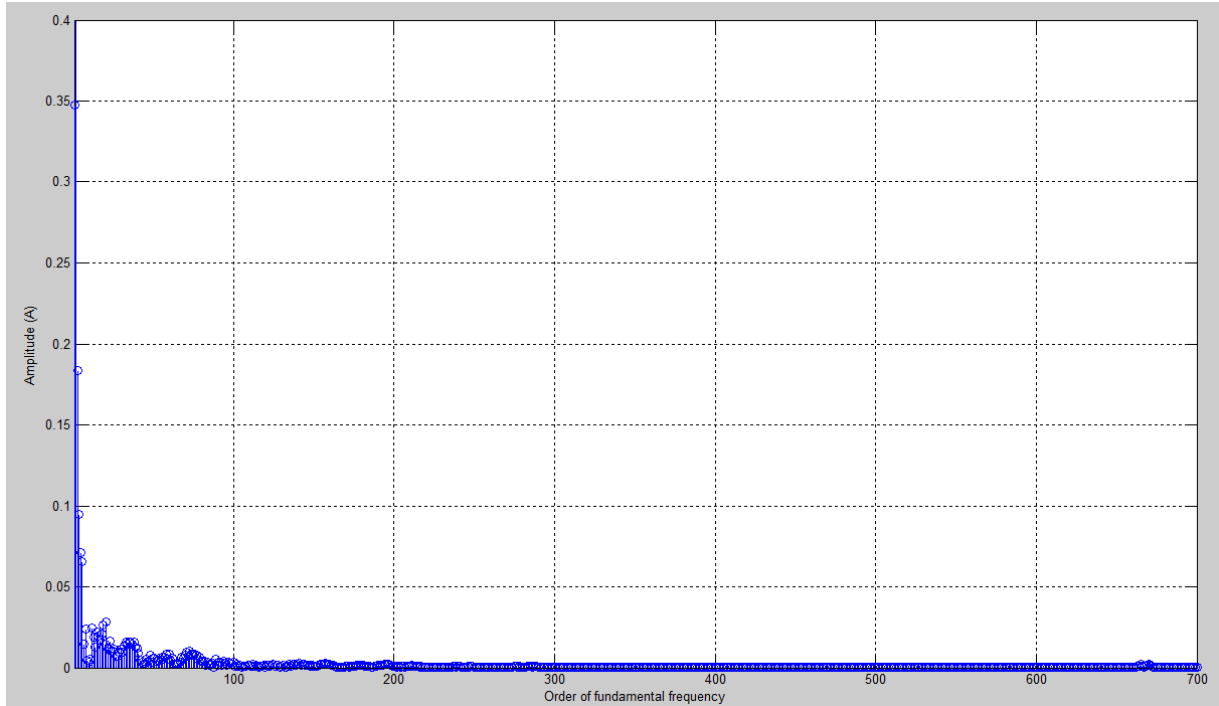


Figure 4-19 Input current spectrum waveforms at half speed of the active front-end rectifier

The waveforms of the PMG and active front-end rectifier system after applying a load step from 200W to 400W are shown in Figure 4-20 and Figure 4-21. The traces from top to bottom are: rotor angle, ac line to line voltage v_{ab} , dc bus voltage V_{dc} and ac phase current i_a in Figure 4-20 and dc bus voltage V_{dc} , q axis reference current i_{qref} , q axis current i_q , and ac phase current i_a in Figure 4-21. After the load step, the ac input current increases to match the load power demand. The q axis current i_q tracks its reference i_{qref} well. There is a small dc voltage dip at the time of the load step. After that the dc output voltage is at controlled effectively at 296.5V.

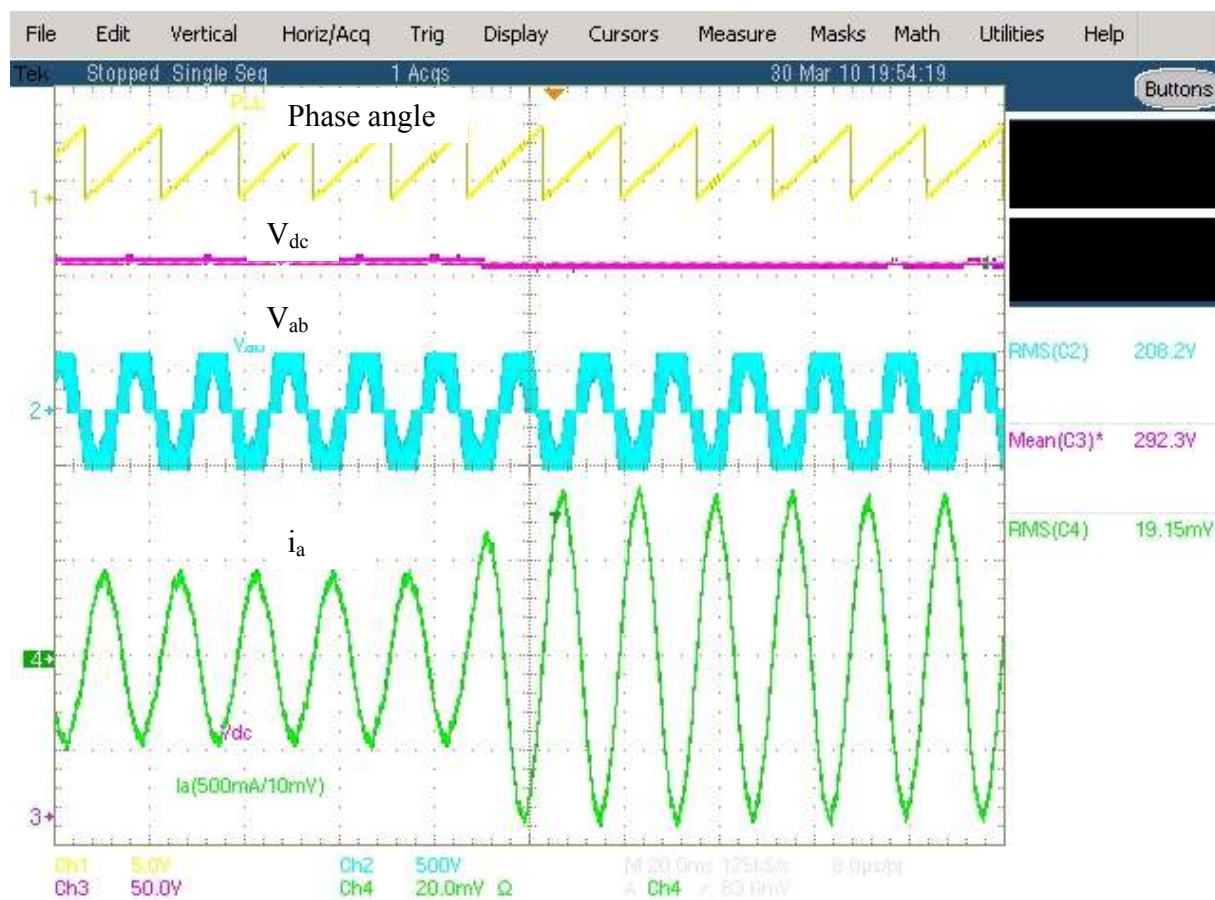


Figure 4-20 Waveforms of angle, PMG terminal voltage v_{ab} , dc bus voltage V_{dc} and ac current i_a after applying a load change from 200W to 400W in the PMG and active front-end rectifier system

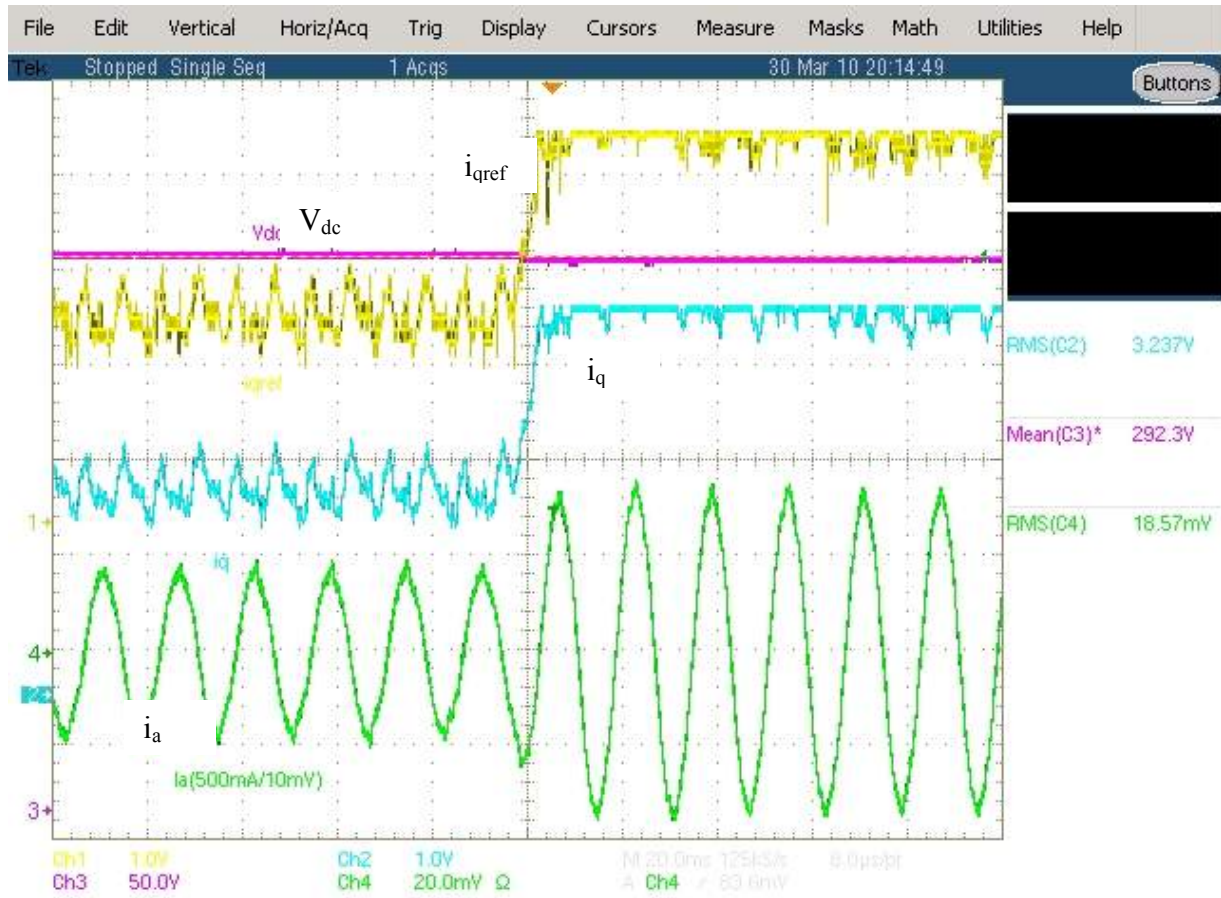


Figure 4-21 Waveforms of dc bus voltage V_{dc} , q axis reference current i_{qref} , q axis current i_q , and ac phase current i_a after applying a load change from 200W to 400W in the PMG and active rectifier system

Compared with the diode rectifier, the active front-end rectifier has many benefits. The dc output voltage is regulated when the generator operates at a wide range of speed. The current harmonics on ac side is much lower, which significantly reduce the power loss in the generator caused by harmonic current.

In the PMG and active rectifier system, the generator speed changes and load steps are applied to test the control algorithm. The dc output voltage is controlled effectively in the tests.

When the PMG runs at half speed, the line frequency is reduced to half while the switching frequency remains, thus the high frequency harmonics due to switching is reduced. Besides, the fundament current doubles reduces the high frequency THD furthermore. However, the THD due

to low frequency harmonics is increased, which might be caused by the generator harmonics when operating at low speed and control. The dc voltage is controlled effectively at 297.1V.

At the load step, the ac input current increases quickly to match the load power demand. The q axis current i_q tracks its reference i_{qref} well. There is a small dc voltage dip at the time of the load step. After that the dc output voltage is at controlled effectively at 296.5V.

Chapter 5 System Efficiency Optimization

This chapter proposes a method to optimize the overall system efficiency by appropriate reactive power distribution. First a linear loss model is given, which is the basis for loss calculation and efficiency optimization. Then the system loss is compared with different reactive power distribution and finally the optimal point is given. The two cases when the DC link voltage is flexible and the DC link voltage is fixed are discussed respectively.

5.1 Reactive Power Distribution

In the PMG and rectifier system, the stator inductance consumes certain reactive power at the operating point, as shown in Figure 5-1. Either the PMG or the rectifier should provide the reactive power. If the rectifier provides all of the reactive power needed by the stator inductor, the unity power factor control is achieved at the back EMF side, as shown in Figure 5-2. If the PMG provides all of the reactive power needed by the stator inductor, the unity power factor control is achieved at the generator terminal side, as shown in Figure 5-3. The overall system efficiency can be optimized by appropriate reactive power distribution between the PMG and the rectifier. The two cases when the DC link voltage is flexible and the DC link voltage is fixed are discussed respectively.

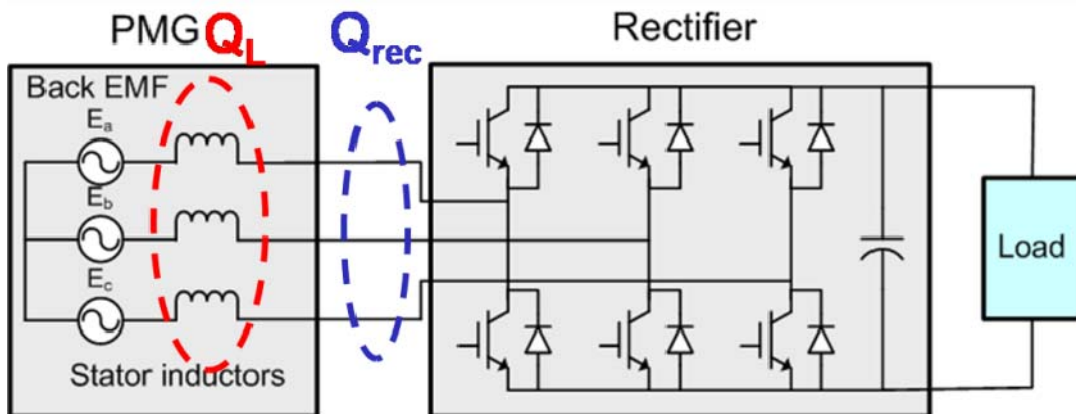


Figure 5-1 Reactive power distribution in the PMG and rectifier system

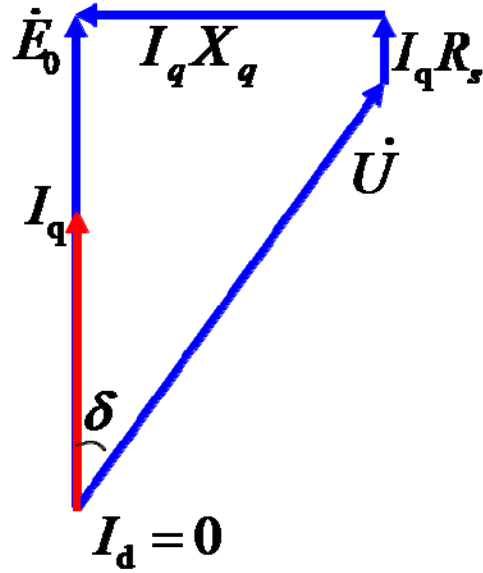


Figure 5-2 Unity power factor control at back EMF side

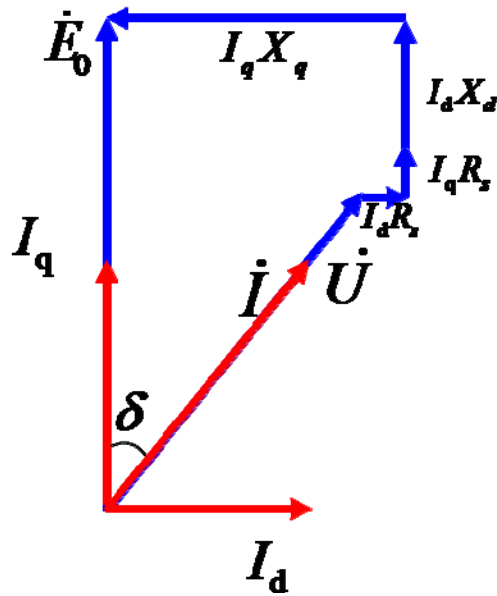


Figure 5-3 Unity power factor control at generator terminal side

The power rating of the system above is 400W. Since the power rating is comparatively small, the difference between the unity power factor control at back EMF side and terminal side is not obvious. So, for the efficiency optimization study, we use a demo system with the power rating of 3500W. The parameters are shown in Table 2-1.

Table 5-1 Parameters of the demo system for efficiency optimization study

Parameter	Symbol	Value
Permanent magnet generator:		
Stator resistance	R_s	0.2Ω
Stator inductance	L_s	3.66mH
Back EMF constant	λ_m	0.113Wb
Nominal power	P_n	3500W
Nominal voltage	V_n	111.9V
Nominal frequency	f	60Hz
Boost rectifier:		
Reference DC link voltage	V_{dcref}	300V
Switching frequency	f_s	20k
DC link capacitor	C	500μF

5.2 Loss Calculation

The loss of the converter includes the conduction loss, the switching loss, the leakage current loss and the driving loss. In our study the leakage current loss and the driving loss are neglected. The conduction loss and switching loss are calculated based on a linear loss model. [40] - [44]

The switching loss is given by

$$P_{sw} = (E_{on} + E_{off} + E_D) \frac{V_{dc} i}{V_{rated} I_{rated}} f_s \quad (5-1)$$

where E_{on} and E_{off} are the rated IGBT turn on loss, turn off loss given for the reference commutation voltage and current V_{rated} and I_{rated} . E_D is the turn off loss of the diode due to reverse recovery charge current. V_{dc} and i indicate the actual commutation current and voltage respectively. f_s is the switching frequency.

The conduction loss of the IGBT and diode is calculated with the close-form equations, which is given by

$$P_{con_IGBT} = \frac{1}{2} \cdot I \cdot V_t \left(\frac{1}{\pi} + \frac{M}{2\sqrt{3}} \cos \phi \right) + I^2 R_{ce} \left(\frac{1}{8} + \frac{2M}{3\sqrt{3}\pi} \cos \phi \right) \quad (5-2)$$

$$P_{con_diode} = \frac{1}{2} \cdot I \cdot V_f \left(\frac{1}{\pi} - \frac{M}{2\sqrt{3}} \cos \phi \right) + I^2 R_{ak} \left(\frac{1}{8} - \frac{2M}{3\sqrt{3}\pi} \cos \phi \right) \quad (5-3)$$

where V_t and V_f are the threshold voltage of the IGBT and diode respectively, while R_{ce} and R_{ak} are the differential resistance the IGBT and diode respectively. These four parameters can be obtained from the output characteristics in datasheet, as shown in Figure 5-4. M is the modulation index. ϕ is the displacement angle between the fundament of the voltage and the load current.

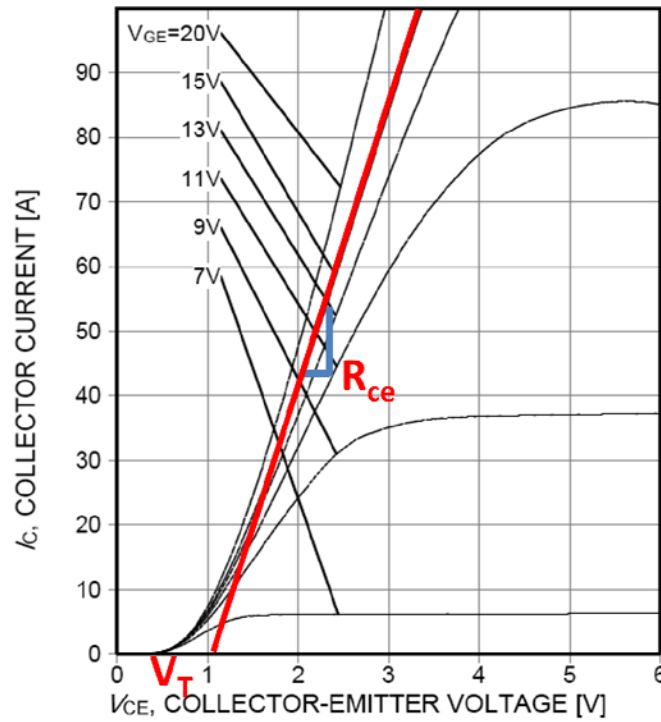


Figure 5-4 Parameters measured from the output characteristics

The loss of the generator includes copper loss, iron loss and mechanical loss. In the study, only the iron loss is considered for simplicity. Iron loss and mechanical loss are neglected. The copper loss is given by

$$P_{copper} = R_s i^2 \quad (5-4)$$

Where R_s is the stator resistance and i is the ac current.

5.3 System efficiency optimization with flexible DC link voltage

In some cases, the DC link voltage is flexible, like AC-DC-AC system. In this case, we assume that the modulation index remains the same. In other words, the DC link voltage changes linearly with the generator terminal voltage. With the reactive power that rectifier provides Q_{rec} changes from zero to all that stator inductance need, the loss and efficiency change as shown in Figure 5-5 to Figure 5-11.

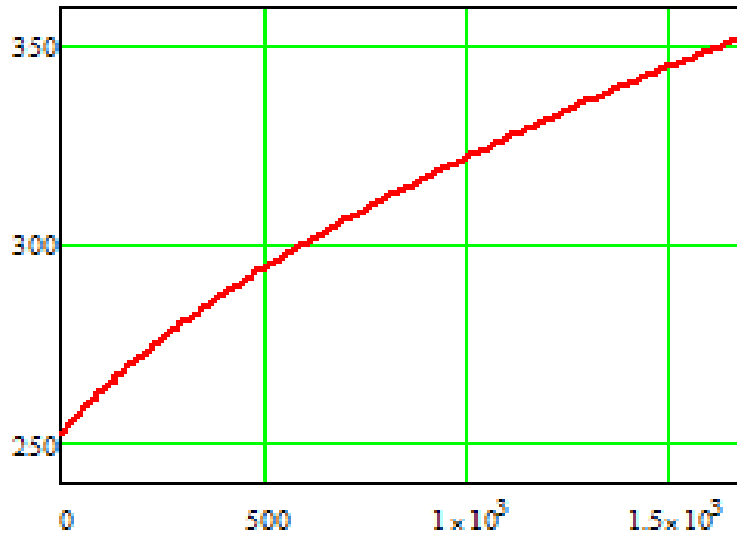


Figure 5-5 DC bus voltage changes with Q_{rec} with flexible DC bus voltage

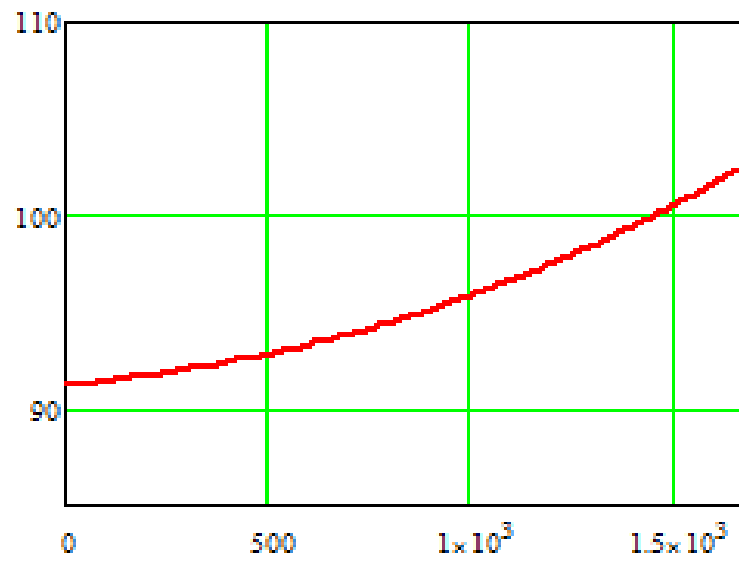


Figure 5-6 Converter switching loss changes with Q_{rec} with flexible DC bus voltage

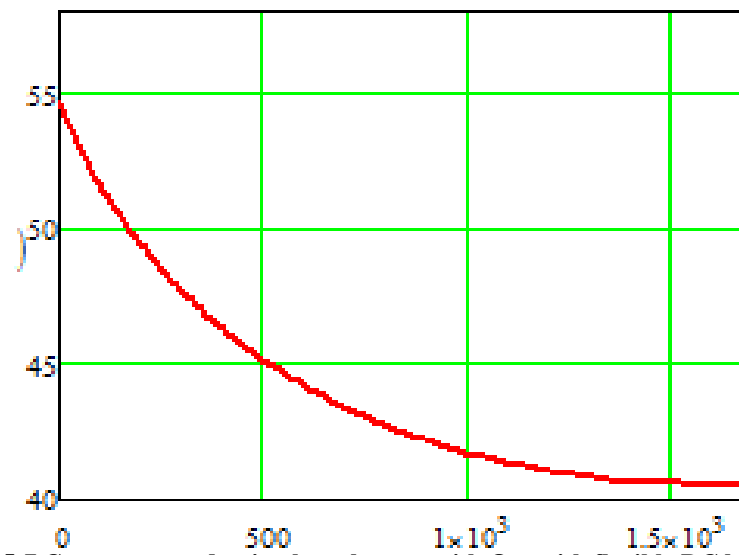


Figure 5-7 Converter conduction loss changes with Q_{rec} with flexible DC bus voltage

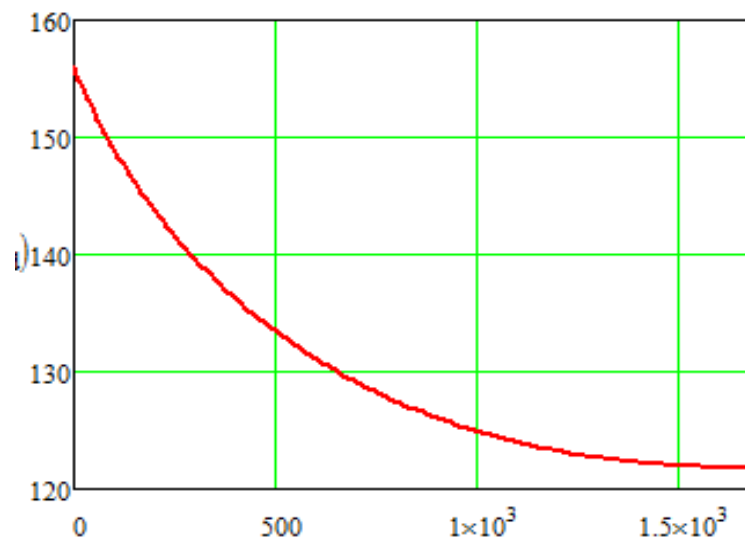


Figure 5-8 Converter total loss changes with Q_{rec} with flexible DC bus voltage

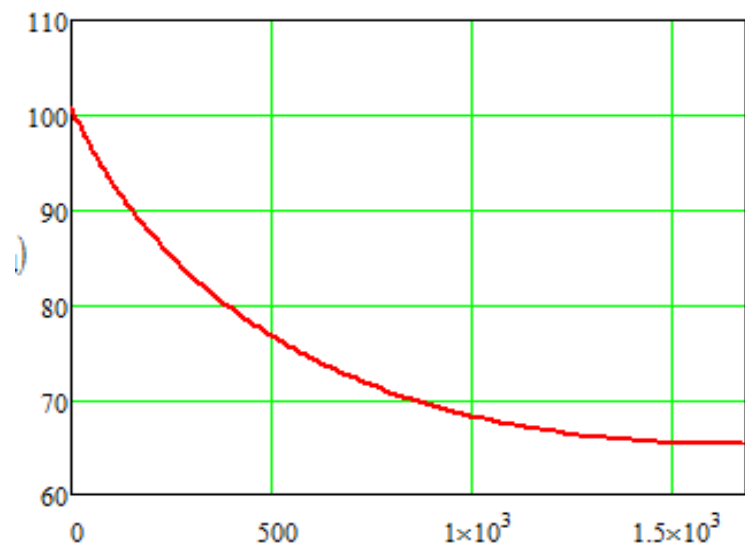


Figure 5-9 PMG copper loss changes with Q_{rec} with flexible DC bus voltage

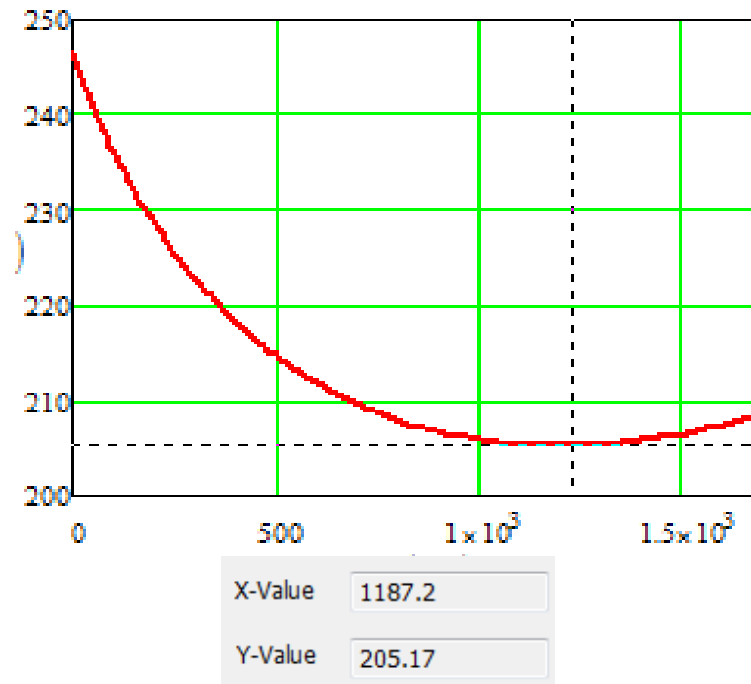


Figure 5-10 System overall loss changes with Q_{rec} with flexible DC bus voltage

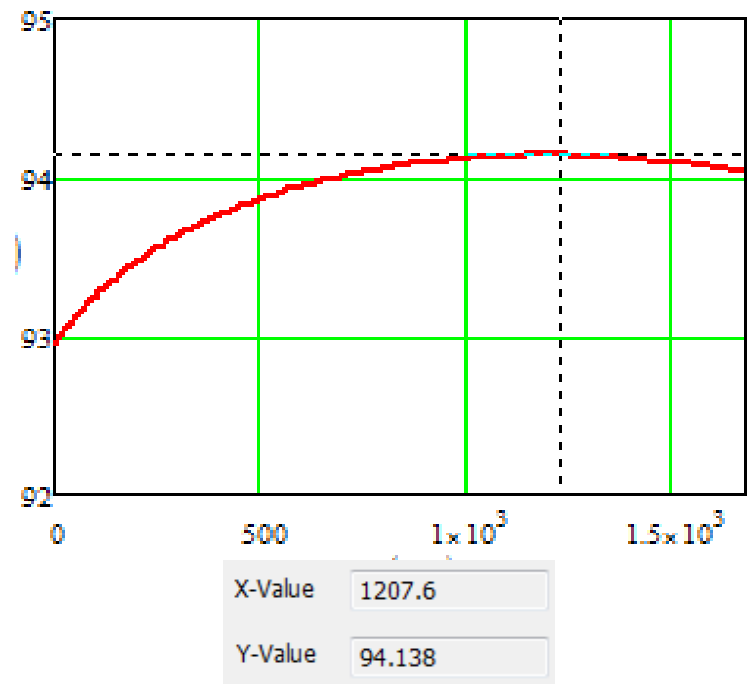


Figure 5-11 System overall efficiency changes with Q_{rec} with flexible DC bus voltage

As the reactive power provided by the rectifier increases, the generator terminal voltage increases while the ac current decreases. The increase of the generator terminal voltage leads to the increase of the DC link voltage when the modulation index keeps the same. The decrease of

the ac current reduces the conduction loss of the rectifier and the copper loss of the generator directly. The switching loss depends on both of the DC link voltage and ac current. It decreases first and then increases and has an optimal point. In the case, the total loss reaches the optimal point when the reactive power provided by the rectifier is 1187.2 VAR, as shown in Figure 5-10. By appropriate reactive power distribution, the efficiency can be improved from 93% to 94.1%.

5.4 System efficiency optimization with fixed DC link voltage

In some cases, the DC link voltage is fixed, like AC-DC system. In this case, the modulation index changes to keep the DC link voltage the same. With the reactive power that rectifier provides Q_{rec} changes from zero to all that stator inductance need, the loss and efficiency change as shown in Figure 5-12 to Figure 5-18.

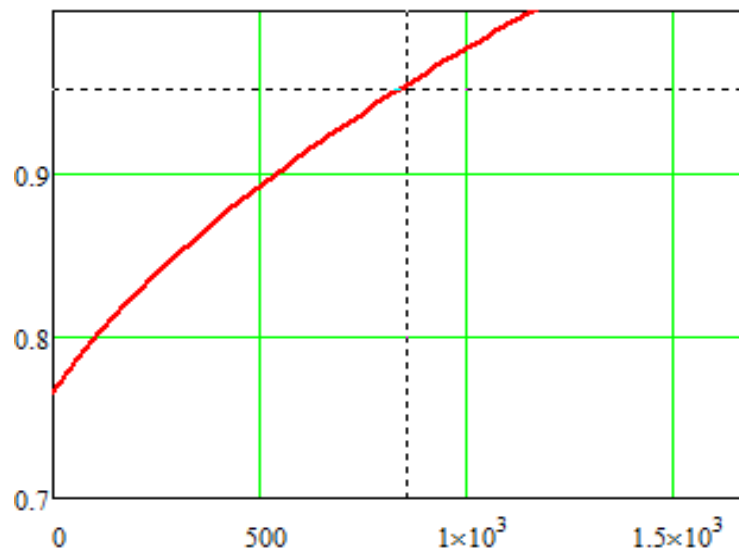


Figure 5-12 Modulation index changes with Q_{rec} with fixed DC bus voltage

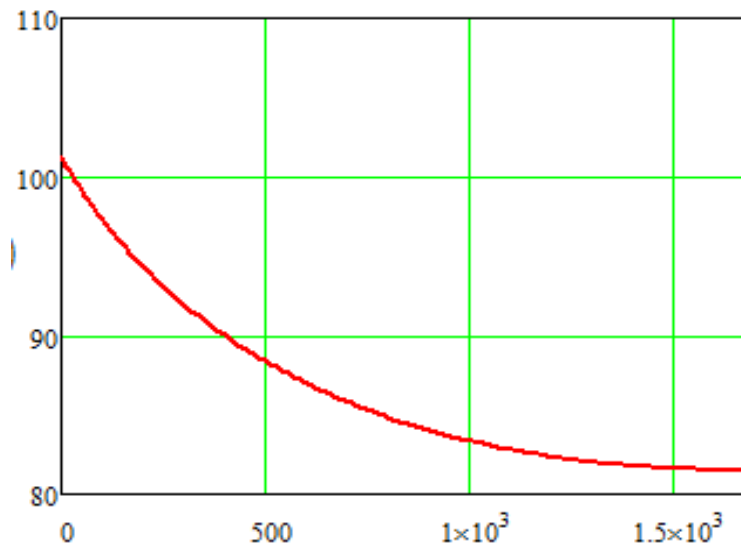


Figure 5-13 Converter switching loss changes with Q_{rec} with fixed DC bus voltage

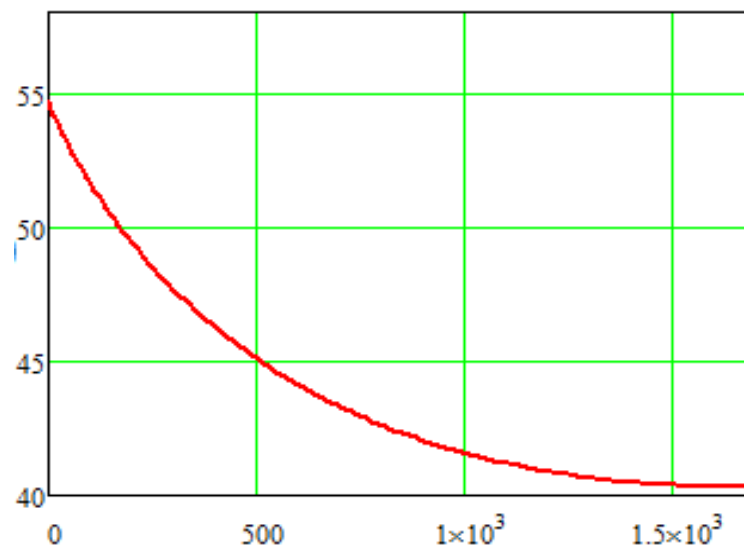


Figure 5-14 Converter conduction loss changes with Q_{rec} with fixed DC bus voltage

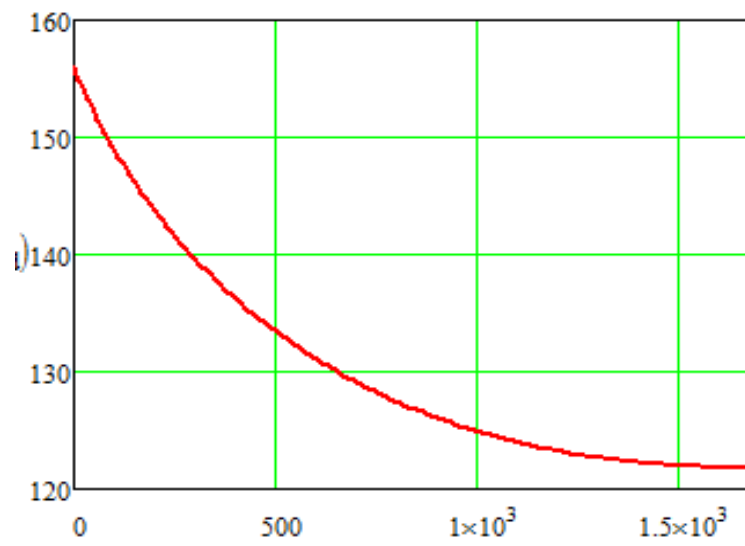


Figure 5-15 Converter total loss changes with Q_{rec} with fixed DC bus voltage

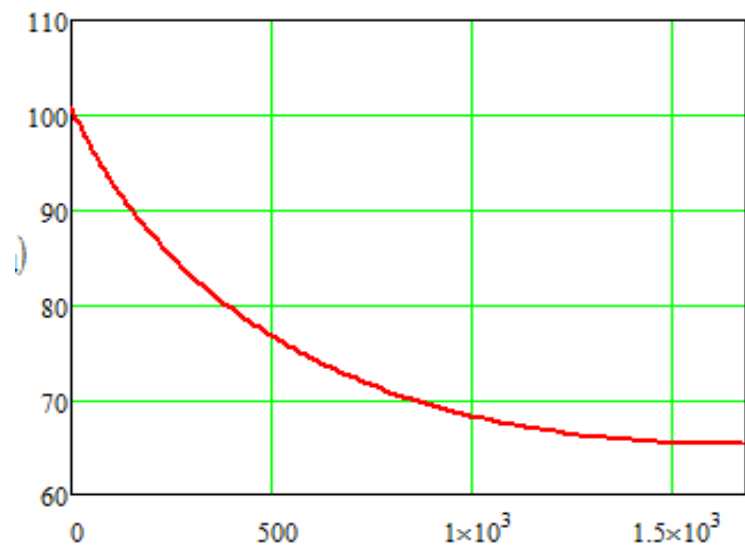


Figure 5-16 PMG copper loss changes with Q_{rec} with fixed DC bus voltage

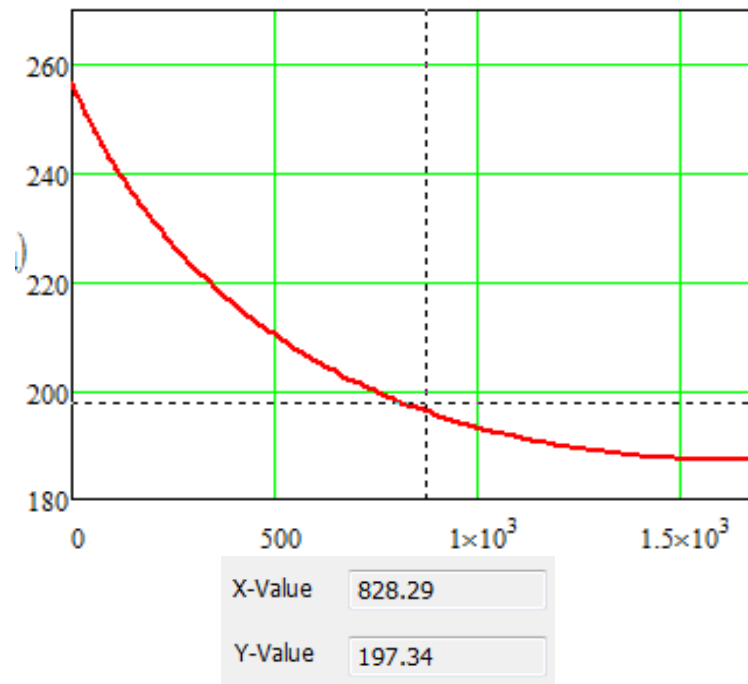


Figure 5-17 System overall loss changes with Q_{rec} with fixed DC bus voltage

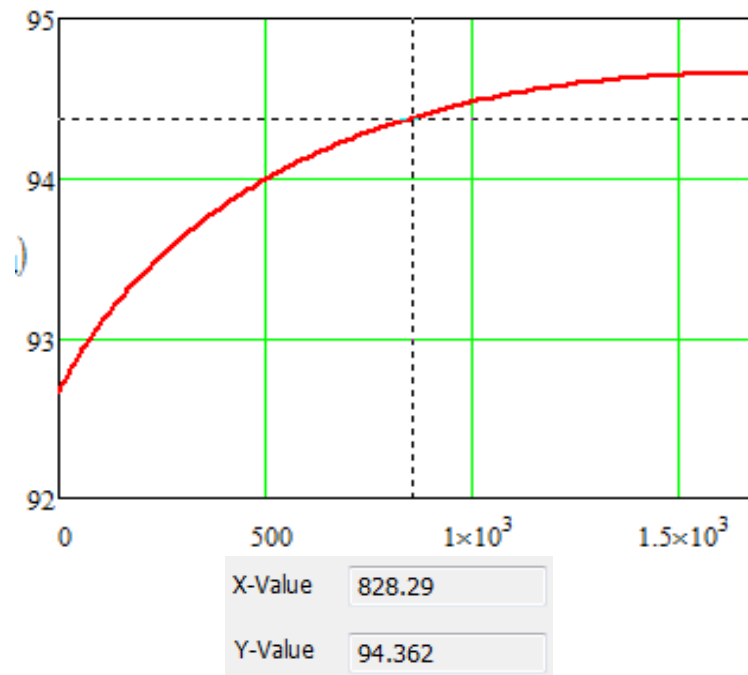


Figure 5-18 System overall efficiency changes with Q_{rec} with fixed DC bus voltage

As the reactive power provided by the rectifier increases, the dc link voltage remains while the ac current decreases, which reduces the conduction loss, the switching loss and the copper loss. As a result, the total loss decreases. When the rectifier provides all the reactive power

needed by the stator inductors, the loss reaches the minimum. However, at this point, the system might be over-modulated. Suppose the modulation index should not exceed 0.95, then the highest efficiency can be reached when the modulation index is 0.95, as shown in Figure 5-18. By appropriate reactive power distribution, the efficiency can be improved from 92.7% to 94.4%.

Chapter 6 Conclusions and Future Work

The chapter summarizes the entire thesis and discusses some idea for the future work.

6.1 *Conclusions*

The paper presented a unified control for the permanent magnet generator and rectifier system. The need for additional boost inductor is eliminated to reduce the volume and weight. Both the DC link voltage and generator power factor can be controlled effectively with the sensorless vector control. The performance of the designed control system is analyzed and verified by simulation and experimental results. System overall efficiency is optimized by appropriate reactive power distribution.

Firstly, the system topology and parameters are described, as well as the reason to select the components value in the system. The unified model containing PWM and rectifier system are presented, which is the basis to design a unified control system.

Secondly, the unified control method for PMG and rectifier system is presented. The design procedure for each control loops are presented in detail, including current control loop, voltage control loop, reactive control loop and speed and rotor position estimator loop. The performance of the designed control system is analyzed and verified by simulation results.

Thirdly, the hardware development for the permanent magnet generator and rectifier system is presented. The hardware including PMG, IPM and drive board, signal conditioning board are explained in detail. Both the voltage control and reactive power control of the PMG and rectifier system are verified through experiment.

Fourthly, a method to optimize the overall system efficiency by appropriate reactive power distribution is proposed. A linear loss model is given, which is the basis for loss calculation and

efficiency optimization. The system loss is compared with different reactive power distribution and the optimal point is given. The two cases when the DC link voltage is flexible and the DC link voltage is fixed are considered.

6.2 *Future Work*

In order to further improve the benefit of unified control for AC-DC system, future work can be carried out in the following directions.

- 1) In the thesis, the efficiency optimization is studied for only a certain operating point. Next the optimization analysis should be given along the whole operating range. Additionally, a more complete loss model should be used.
- 2) The unified control of the synchronous generator and rectifier system is continued to be study. The system optimization will be achieved by both the field control and reactive power factor control.
- 3) The overall system benefits will be studied, including the stability, weight and so on.

REFERENCE

- [1] Z. Chen and E. Spooner, "Simulation of a direct drive variable speed energy converter," *Proc. of ICEM 1998*, pp. 2045 – 2050.
- [2] Z. Chen and E. Spooner, "Grid power quality with variable speed wind turbines," *IEEE Trans. Energy Conversion*, vol. 16, no. 2, 2001, pp. 148 - 154.
- [3] S. B. Papaefthimiou and S. A. Papathanassiou, "Simulation and control of a variable speed wind turbine with synchronous generator," *Proc. of ICEM 2006*, pp. 593 – 598.
- [4] I. Schiemenz and M. Stiebler, "Control of a permanent magnet synchronous generator used in a variable speed wind energy system," *Proc. of IEMDC 2001*, pp. 872 - 877.
- [5] Q. Deng, G. Liu and F. Xiao, "Control of variable-speed permanent magnet synchronous generators wind generation system," *Proc. of ICEM 2008*, pp. 2454 - 2458.
- [6] M. Chinchilla and S. Burgos, "Control of permanent-magnet generators applied to variable-speed wind-energy systems connected to the grid," *IEEE Trans. Energy Conversion*, vol. 21, no. 1, 2006, pp. 130 - 135.
- [7] J. Kang, "General Purpose Permanent Magnet Motor Drive without Speed and Position Sensor", [http://www.yaskawa.com/site/dmdrive.nsf/link2/NKOE-7U9HJG/\\$file/WP.AFD.05.pdf](http://www.yaskawa.com/site/dmdrive.nsf/link2/NKOE-7U9HJG/$file/WP.AFD.05.pdf)
- [8] M. Rastogi, R. Naik and N. Mohan, "A comparative evaluation of harmonic reduction techniques in three-phase utility interface of power electronic loads," *IEEE Trans. Industrial Application*, vol. 30, no. 5, 1994, pp. 1149 - 1155.
- [9] V. Blasko and V. Kaura, "A new mathematical model and control of a three-phase AC-DC voltage source converter," *IEEE Trans. Power Electronics*, vol. 12, no. 1, 1997, pp. 116 - 123.
- [10] A. Draou, Y. Sato and T. Kataoka, "A new state feedback based transient control of PWM AC to DC voltage type converters," *IEEE Trans. Power Electronics*, vol. 10, no. 6, 1995, pp.716 -724.
- [11] P. Verdelho and G.D. Marques, "DC voltage control and stability analysis of PWM-voltage-type reversible rectifiers," *IEEE Trans. Industrial Electronics*, vol. 45, no. 2, 1998, pp. 263 - 273.
- [12] S. Hiti, D. Boroyevich and C. Cuadros, "Small-signal modeling and control of three-phase PWM converters," *Proc. of IAS 1994*, pp. 1143 - 1150.
- [13] S. Miller and J. Sun, "Comparative study of three-phase PWM rectifiers for wind energy conversion," *Proc. of APEC 2006*, pp. 937-943.

- [14] M. Rashid, *Power Electronics Circuits, Devices and Applications, Chapter 10—Controlled Rectifiers*
- [15] S. Hiti and D. Boroyevich, "Control of front-end three-phase boost rectifier," *Proc. of APEC 1994*, pp. 927 - 933.
- [16] S. Rosado, R. Burgos, S. Ahmed, F. Wang and D. Boroyevich, "Modeling of power electronics for simulation based analysis of power systems," *Proc. of SCSC 2007*, pp. 19 - 26.
- [17] K. Tatematsu, D. Hamada, K. Uchida, S. Wakao and T. Onuki, "New approaches with sensorless drives," *IEEE Industrial Application Mag.*, 2000, pp. 44 - 50.
- [18] O. Wallmark, L. Hernefors, and O. Carlson, "Sensorless control of PMSM drives for hybrid electric vehicles," *Proc. of PESC 2004*, pp. 4017 - 4023.
- [19] R. Lorenz, and K. Van Patten, "High-resolution velocity estimation for all-digital, AC servo drives," *IEEE Trans. on Ind. Industrial Application*, vol. 27, no. 4, 1991, pp. 701 - 705.
- [20] J.-R. Kim, S.-K. Sul, and M.H. Park, "Speed sensorless vector control of induction motor using extended Kalman filter," *IEEE Trans. Industrial Application*, vol. 30, no. 5, 1994, pp. 1225 - 1233.
- [21] J.-S. Kim and S.-K. Sul, "New approach for high-performance PMSM drives without rotational position sensors," *IEEE Trans. Power Electronics*, vol. 12, no. 5, 1997, pp. 904 - 911.
- [22] J.-S. Yim, W.-J. Lee, S.-K. Sul, H.-S. Yang and J.-T. Kim, "Sensorless vector control of super high-speed turbo compressor," *Proc. of PESC 2005*, pp. 950 - 953.
- [23] V. Kaura, and V. Blasko, "Operation of a phase locked loop system under distorted utility conditions," *IEEE Trans. Industrial Application*, vol. 33, no. 1, 1997, pp. 58 - 63.
- [24] R. Burgos, P. Kshirsagar and A. Lidozzi, "Design and evaluation of a PLL-based position controller for sensorless vector control of permanent-magnet synchronous machines," *Proc. of ISIE 2005*, pp. 1081 - 1086.
- [25] R. P. Burgos, P. Kshirsagar, A. Lidozzi, F. Wang and D. Boroyevich, "Mathematical model and control design for sensorless vector control of permanent magnet synchronous machines", *Proc. of COMPEL 2006*, pp. 76 – 82
- [26] B. Shi, G. Venkataramanan, N. Sharma, "Design Considerations for Reactive Elements and Control Parameters for Three Phase Boost Rectifiers", *2005 IEEE International Conference on Electric Machines and Drives*, pp. 1757 - 1764.

- [27] F. Barruel, J.L. Schanen and N. Retiere, "Volumetric optimization of passive filter for power electronics input stage in the more electrical aircraft", *IEEE Electronics Specialists Conference (PESC), Jun. 2004*, pp. 433 - 481.
- [28] S. Chandrasekaran, D. Borojevic, D. K. Lindner, "Input filter interaction in three phase AC-DC converters", *PESC 1999*, Vol. 2, pp. 987 - 992.
- [29] P. Pillay, R. Krishnan, "Modeling of permanent magnet motor drives", *IEEE Transactions on Industrial Electronics*, 1988, pp. 537 – 541.
- [30] C. Attaianesi, V. Nardi, G. Tomasso, "Modelling of permanent magnet AC machine by taking into account dynamic and static inductances", *Proceedings IEEE IAS Annual Meeting 2004*, vol.3, pp. 1709 - 1714.
- [31] S. Weisgerber, A. Proca, A. Keyhani, "Estimation of Permanent Magnet Motor Parameters", *Proceedings IEEE IAS Annual Meeting 1997*, Vol. 1, pp: 42 - 49.
- [32] N. Urasaki, T. Senjyu, K. Uezato, "An Accurate Modelling for Permanent Magnet Synchronous Motor Drive", *Proc of APEC 2000*, Vol.1, pp: 387 - 392.
- [33] A. Consoli, A. Raciti, "Analysis of Permanent Magnet Synchronous Motor", *IEEE Transactions on Industry Application*, Vol. 27 No. 2, 1991, pp: 350 - 354.
- [34] H. Akagi, Y. Kanazawa, A. Nabae, "Instantaneous reactive power compensators comprising switching devices without energy storage components", *IEEE Transactions on Industry Applications*, 1984, pp: 625 - 630.
- [35] D. M. Divan and T. H. Barton, "Considerations on the application of improved power factor converter structures," *IEEE Trans. Ind. Applicat.*, vol. 19, 1983, pp. 1076–1084.
- [36] K. Matsuse, H. Kubota, and L. Huang, "Performance of PWM-controlled thyristor rectifier operating at unity fundamental power factor in PWM current source GTO inverter system for induction motor drives," *IEEE Trans. Ind. Applicat.*, vol. 30, 1994, pp. 699–706.
- [37] J. W. Kolar, H. Ertl and F. C. Zach, "Design and experimental investigation of a three-phase high power density high efficiency unity power factor PWM (VIENNA) rectifier employing a novel power semiconductor module", *Proc. of APEC 1996*, pp. 514-523.
- [38] J. Minibock, F. Stogerer and J. W. Kolar, "Comparative theoretical and experimental evaluation of bridge leg topologies of a three-phase three-level unity power factor rectifier", *Proc. of PESC 2001*, pp. 1641-1646.
- [39] H. Sugimoto, S. Morimoto and Y. Yano, "A high performance control method of a voltage-type PWM converter," *Proc. of PESC 1988*, pp. 360 - 368.

- [40] M. H. Bierhoff, F. W. Fuchs, "Semiconductor losses in voltage source and current source IGBT converters based on analytical derivation", *Proc. of PESC 2004*, pp. 2836 - 2842.
- [41] F. Cmanellm, "Losses in PWM inverters using IGBTs", *IEE Proc of Electr. Power Appl.*, 1994, pp. 235 – 239.
- [42] K. Tan, T. T. Yao and S. Islam. "Effect of loss modeling on optimum operation of wind turbine energy conversion system," *Proc. of IPEC 2005*, pp. 1 - 6.
- [43] T. Senjyu, S. Tamaki, N. Urasaki and K. Uezato, "Wind velocity and rotor position sensorless maximum power point tracking control for wind generation system," *Proc. of PESC 2004*, pp. 2023-2028.
- [44] A. Tommaso, R. Miceli, G. Galluzzo. "Efficiency control for permanent magnet synchronous generators," *Proc. of ICIT 2006*, pp. 2079-2084.